Synthesis and Function of Ion-Selective Single-Molecule Fluorescent Imaging Molecules and Materials

by

Alena A. Denisenko

Presented to the Faculty of the Graduate School of

The University of Texas at Arlington in Partial Fulfillment

of the Requirements

for the Degree of

DOCTOR OF PHILOSOPHY

THE UNIVERSITY OF TEXAS AT ARLINGTON

May 2022

Copyright © by Alena Aleksandrovna Denisenko 2022

All Rights Reserved

Acknowledgments

It is with great pleasure that I thank my supervisor, Dr. Frank W. Foss Jr., for his excellent mentorship and support throughout the years. In addition to sharing his knowledge with me, he encouraged me to pursue my scientific interests by leading by example and inspiring me to continue working hard and pushing myself to overcome my limits. Dr. Foss' research group has been significant to me, and I feel humbled to have been a part of it.

Also, I would like to thank all the members of my Dissertation Committee: Dr. Carl Lovely, Dr. He Dong, and Dr. Kwangho Nam, for their guidance and suggestions. In addition, I would like to thank Dr. Benjamin Jones and his excellent group, with whom I learned to think outside the box and enjoyed working. My deepest thanks go out to my colleagues in the Organic Division and other research labs for their support, suggestions, valuable discussions, and friendship. I would like to thank Dr. Pawan Thapa, Shan Hazoor, Anurag Noonikara Poyil, Olatunji Ojo, Enrique Barragan, Maya Boyd, Chini Avisankar, Nicholas Byrnes, Karen Navarro, Reagan Miller, Thanh Vuong, Patrick Ho, and Ryan Madigan. My sincerest thanks to all of you who supported me during my time of need.

I am grateful to my mentor and supporter, Dr. Alejandro Bugarin, for believing in me and introducing me to the fascinating world of science. I am incredibly thankful to Dr. Seiichiro Tanizaki, with whom I had the pleasure of working and assisting him in teaching a course where I gained valuable skills in teaching and learning. I would also like to express my gratitude to the outstanding staff at UT Arlington for their help making this possible. My sincere gratitude goes out to the Administrative Assistants, Mrs. Jill Howard and Mrs. Debbie Cooke, and the Coordinator of the Graduate Program, Mrs. Stephanie Henry. Additionally, I would like to thank Dr. Brian Edwards and Dr. Roy McDougal for their training and assistance. Furthermore, I would like to thank our Undergraduate Lab Coordinators, Dr. William Cleaver and Dr. Cynthia Griffith, for their support and advice regarding teaching duties, as well as the Stockroom Supervisors, Mrs. Beth Klimek, for providing me with all of the supplies that I needed throughout the entire semester.

Moreover, I am incredibly grateful to my husband, Daniel Trinidad, who is incredibly supportive of me and always loves me; to my children, Saveliy Trinidad and Amelia Trinidad, whom I love and who teach me to value time and care for others; to my parents, Silvia Trinidad and Tito Trinidad for raising and guiding my children and giving me the opportunity to go to school; to my role models, my mother Zoya Denisenko and father Aleksandr Denisenko who have always been there for me and helped me grow into what I am today. I would also like to thank my sister Galina Maki for giving me the opportunity to come to the United States and pursue my career. To my dear friend John Michael, whom I consider my brother, thank you for believing in me.

Abstract

Synthesis and Function of Ion-Selective Single-Molecule Fluorescent Imaging Molecules and Materials

Alena Denisenko, Ph.D.

The University of Texas at Arlington, 2022

Supervising professor: Frank W. Foss, Jr.

Neutrinos are fermion subatomic particles that interact only by weak subatomic forces—making them almost impossible to detect. However, they can be produced in specific radioactive decay reactions, such as beta decay.

We hypothesize the detection of double beta decay through the tagging of the Ba^{2+} daughter ion from ^{136}Xe (^{136}Xe —$^{136}Ba^{2+} + 2v + 2\beta$). The proposal is to develop single-molecule fluorescence imaging (SFMI) technology to investigate gaseous chemical constituents in high-pressure gases (ca. 30-150 psi) at gas-solid interfaces. To achieve proper SMFI, heterogenous self-assembled monolayers (SAMs) containing fluorophores that operate under dry conditions and are turned on when a covalently attached binding domain captures Ba^{2+} pursued. Many technological advances in molecular sensors are required to achieve this goal.

The background context and the contributions to the field are outlined in **chapter 1**. The key ideas behind the design of different crown ether chelating agents with diverse fluorophores to demonstrate a fluorescent response to Ba^{2+} cation is argued. SMFI is being applied in the search for neutrinoless double-beta decay ($0v\beta\beta$) through the development of novel barium sensing molecules that will be employed as the first dry-phase chemosensor to detect Ba^{2+} ions using the new method, which is still in progress.

Chapter 2 discusses the synthesis of the first-generation barium chemosensor tags. Anthracene substituted aza-18-crown-6-ether has been shown to function in the dry phase with almost no intrinsic background from the unchelated state. Through fluorescence microscopy with single barium ions in the

solution, the sensors perceive barium ions in dry films, opening the door to the detection of single ions in high-pressure xenon gas.

By applying naphthalimide to (di)aza-crown-ether chemosensors in **chapter 3**, we developed simple, robust, and effective Ba^{2+} selective chemosensors that performed well in ^{136}Xe gas under high pressure while achieving SFMI in polyacrylamide matrix. NMR spectroscopy and fluorescence experiments support the concept of photoinduced electron transfer for turn-on sensing. Using an oil-free microscopy technique, we succeeded in imaging Ba^{2+} ions within the large volumes of ^{136}Xe for the first time, which is an essential step toward finding the hypothetical process known as $0\nu\beta\beta$.

In **chapter 4**, we explore the synthesis of the Hg^{2+} sensor. Mercury selective aminonapthalimide-aza-crown-ether sensor has an ion charge transfer mechanism, able to fluoresce selectively in a variety of solvents as well as cells and solvent-free matrices. Their significant selectivity for Hg^{2+} ions offers the potential for use as a functional chemosensor for trace mercury in various solvent-free matrices.

Finally, in **chapter 5,** we discuss the preliminary approaches and data concerning the development of SAMs. The fine-tuning of functional chemosensors with SAMs at transparent dielectric surfaces may be accomplished by fluorescent monomer synthesis, APTES growth, the addition of spacer/functional molecule, and quality analysis of the monolayer formation by using different analytical techniques such as atomic force microscopy (AFM) and total internal reflection fluorescence (TIRF) microscopy.

In summary, we have generated fluorescent dyes for dry phase sensing of Ba^{2+} in a gaseous Xe and examined the function of the monolayer formation for Ba-tagging using single-molecule fluorescent imaging tags (SMFI). Our current research focuses on the formation and identification of SAMs using analytical techniques, such as AFM and TIRF microscopy.

Table of Content

List of illustrations and tables

Chapter 1. Introduction and previous work

1.1. Introduction to neutrinos

Neutrinos, which are being searched for in particle and experimental physics, pose an open question in the universe. Having the neutrino as a first-order particle was proposed by Wolfgang Pauli in 1930, one of the greatest Austrian theoretical physicists and a pioneer of quantum mechanics. He is famous to chemists for formulating Pauli's Exclusion Principle. According to Pauli's hypothesis, beta decay conserves energy, momentum, and angular momentum. In gas or liquid, detecting neutrinoless double beta decay (0vββ) is the most sensitive and promising method to determine whether the neutrino is a Majorana particle, a particle capable of being both its antiparticle and its progeny.

In different international collaborations, hypotheses are examined for the first detection of 0vββ decay, including the use of nuclei known to undergo 0vββ decay: ^{76}Ge, ^{136}Xe, ^{130}Te, ^{100}Mo, among others.[1] The experimental challenge in all of these studies is identifying one or a handful of decay events for a given mass of a particular isotope, which is complicated by several factors, such as the theoretically long half-life of 0vββ decay (over 1.8 x 1026 yr. in ^{76}Ge and over 1.0 x 1026 yr. in ^{136}Xe) and high levels of background noise.[1] Studying these phenomena in ^{136}Xe at high pressure is the focus of the NEXT collaboration. First of all, the attainable energy resolution at the Q-value of the decay (^{136}Xe is 2458 keV) should be considered when selecting between gaseous or liquid xenon.[2] Second, the projected duration of the ionization tracks in high-pressure xenon can help distinguish between events that are either signals or background noise.[2] The hypothetical detection of single ^{136}Ba ions produced by ^{136}Xe decay ("barium tagging") can be used to detect neutrinoless double-beta decay with an ultra-low background. Using this method is dependent upon the development and demonstration of a high-pressure gaseous xenon electroluminescent time projection chamber (HPXe EL-TPC) sensitive to single ions in gaseous xenon. A technology developed by Dr. Dave Nygren, the track path detector (TPC), enables direct three-dimensional tracking through an electronically read gaseous detector.[3] This method can be used to reconstruct the events of up to 20 particles colliding at the electron-positron collider. The detection of the beta particle energies is currently ongoing; however, if the Majorana particle does exist, additional energy will be detected in the ejected electron when two neutrinos collide. A method of detecting individual barium daughter ions by single-molecule fluorescence imaging (SMFI) has been proposed for tagging gas-phase ions with barium. In order to investigate neutrinoless double beta decay using fluorescence microscopy in the TPC chamber, we developed dry-phase barium chemosensor molecules for use in high-pressure xenon gas. This significantly enhances the sensitivity of searching for neutrinoless double-beta decay.

1.2. Previous studies[4]

Single-Molecule Fluorescence Imaging was one of the first proposed ideas describing an automatic in situ identification method for Ba^{2+} in high-pressure xenon gas. It was published by Austin McDonald, Ben Jones, and Dave Nygren.[4] Using liquid detection methods, they are using the various molecules known to detect Ca^{2+} in biological systems **(Figure 1).**

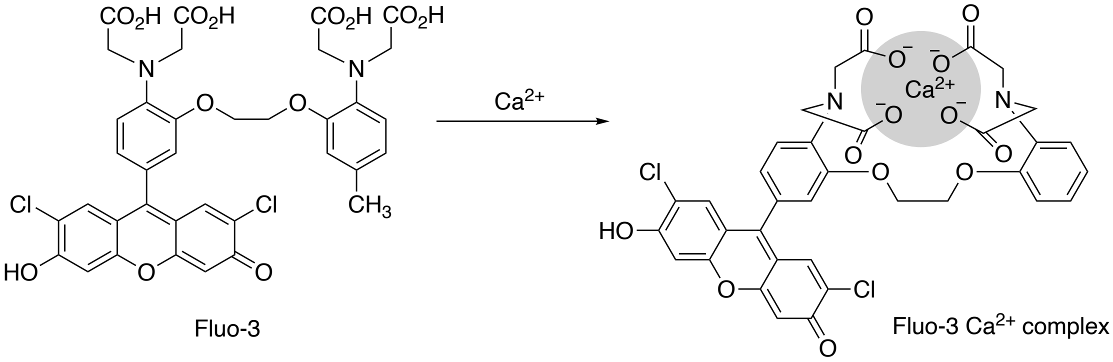

Figure 1. The structure of **Fluo-3** before and after complex formation.

In order to determine if fluorescence behavior can be maintained in a high-pressure gaseous Xe (HPGXe) detector, such as the one understudy in the NEXT collaboration, three steps were required: 1) identifying dyes that provide a strong fluorescence response to barium; 2) developing a scanning system that can be used to tag barium in large detectors; 3) optimizing the detection technique to detect single molecules.[4,31] Due to their strong detection of Ca^{2+}, **Fluo-3** and **Fluo-4** were chosen for Ba detection due to barium and calcium having similar electronic configuration states, with the difference between the two molecules having chlorine substituents replaced with fluorines. In addition, the excitation in the blue region is convenient for laser and microscope development, since both molecules have strong excitation in the blue region. The optical system was constructed using the laser with 488 nm wavelength as an excitation light source coupled into a numerical aperture multimode fiber using a 10X microscope objective and plastic cuvette to

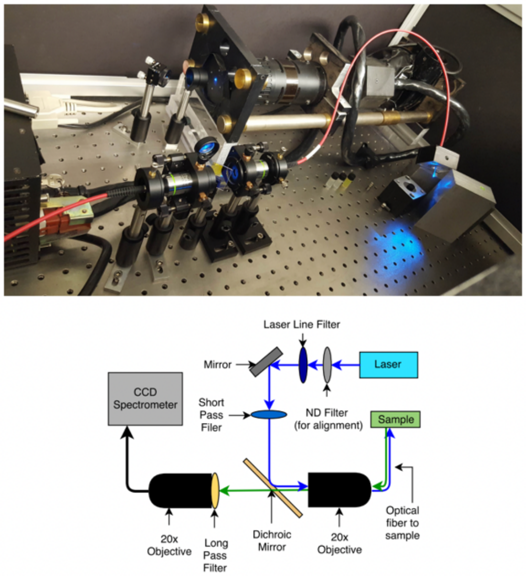

Figure 1.1. Photograph (top) and diagram (bottom) of the optical system.[4]

(Copyright Clearance Center, Inc. granted the permission for the use of the image.)

place the fluorescent mixture approximately 1 m away from the fiber within the custom-made cuvette holder (**Figure 1.1**)[4]. The laser line filters were used to block the long-wavelength background light. Due to its similarity to **Fluo-4** and the fact that it can be examined independently of chelation, fluoresceine was used to configure the system. Using **Fluo-3** and **Fluo-4** at 100 μM concentrations in buffer, studies on Ba began.

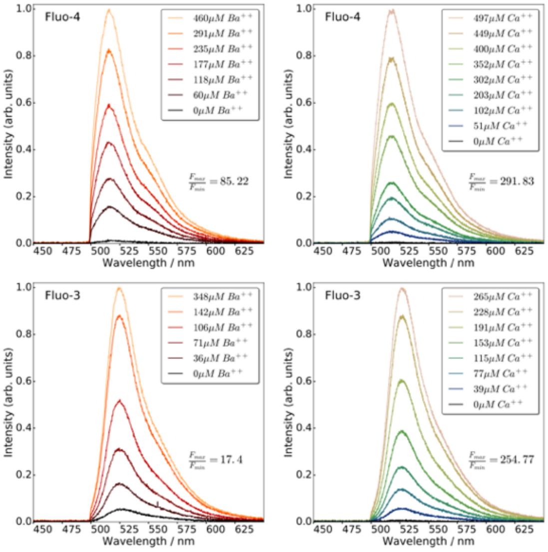

Figure 1.2. Ca^{2+} (left) and Ba^{2+} (right) induced fluorescence in **Fluo-4** (top) and **Fluo-3** (bottom) dye solutions.[4] (Copyright Clearance Center, Inc. granted the permission for the use of the image.)

BAPTA was used to suppress the significant fluorescent background caused by the addition of 5 nM calcium ion chelators. A clear demonstration of barium's ability to induce fluorescence by the addition of barium perchlorate solution in **Figure 1.2** shows that **Fluo-3** and **Fluo-4** are suitable dyes for barium sensing, as well as the capability of the remote optical system to detect barium ions. The dyes, developed for calcium dication detection, have a high affinity for barium dications, making them potentially useful for SMFI in xenon gas TPCs.

The previous studies identified a new method of searching for neutrinoless double-beta decay using the SMFI technique for the progress of the search for neutrinoless double-beta decay. In light of the fluorescence studies using **Fluo-3** and **Fluo-4** dyes showing signal-to-noise ratios in liquid, the next step is to look for dyes that operate in gaseous environments, using the scanning system developed by Dr. Jones' group, and finally, the development of a system called SAMs for detection of Ba^{2+} in TPC chamber.

Chapter 2.

Barium Chemosensors with Dry-Phase Fluorescence for Neutrinoless Double Beta Decay

P. Thapa, I. Arnquist, N. Byrnes, A.A. Denisenko, F.W. Foss Jr., B.J.P. Jones, A.D. McDonald, D.R. Nygren, and K. Woodruff.

(Reproduced with permission from Springer Nature, *Scientific Reports* 9, Article number 15097 (2019)).

2.1. Introduction

The search for neutrinoless double-beta decay (0νββ) is a major focal point of experimental nuclear physics worldwide. If and only if the neutrino is a Majorana fermion (a particle that is its own antiparticle), the lepton-number violating nuclear decay ${}^{N}_{Z}X \rightarrow {}^{N}_{Z-2}X + 2e$ may take place. An observation of this decay would simultaneously prove that the lepton number is not conserved in nature; demonstrate the existence of physics beyond the standard model responsible for the lightness of neutrino masses;[5-9] lend weight to lipogenesis as the mechanism for introducing matter-antimatter asymmetry into an initially symmetrical Universe.[10] The search for 0νββ has spurred the development of many sensitive detection techniques.

The primary challenges involved in the search for 0νββ derive from the fact that this process if it occurs at all, is extremely slow. Present experimental lower limits on 0νββ lifetime sit at 1.2×10^{26} years.[11] Well-motivated theoretical models involving light neutrino exchange predict that 0νββ could be observed with any lifetime beyond this limit,[12-14] given present knowledge of neutrino masses and mixing angles. Observing such a rare process above experimental background from sources such as detector material gamma rays,[15] dissolved radioisotopes,[16,17] neutron captures,[18] and others is a formidable experimental challenge, requiring deep underground detectors, exquisite radio-purity,[19-21] and extremely selective signal identification and background rejection methods.

The target for the next generation of experiments is to deploy ton- to multi-ton-scale detectors with background rates of less than 0.1 counts per ton per year in the experimental region of interest (ROI). At the time of writing, the best-demonstrated background rate from any technology has been demonstrated by germanium diodes and is around four in these units.[22,23]

One isotope that has drawn particular attention as a suitable candidate for building very large, low background 0νββ experiments is ^{136}Xe, which could decay via 0νββ to ^{136}Ba + 2e. Technologies have been developed to search for 0νββ of ^{136}Xe in both liquid (LXe)[2] and gas (GXe)[24] phases, and dissolved in liquid scintillator (LSXe),[11] with the latter providing the present strongest limit. The lowest background rate from a running 0νββ search in ^{136}Xe is from the EXO-200 experiment using LXe and is ~144 counts per ton per year in the ROI.[2] The NEXT program is presently constructing a 100 kg high-pressure GXe (HPGXe) detector called NEXT-100 that projects a background index of between 5 and 10 counts per ton per year in the ROI.[15] Despite impressive technological advances from all techniques, an effectively background-free 0νββ technology for the ton-scale and beyond remains undemonstrated.

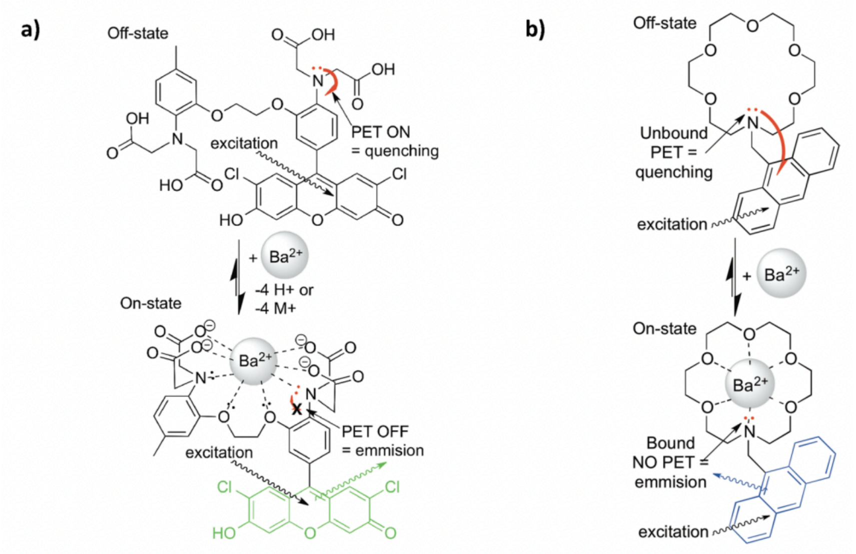

Figure 2. Cartoon showing binding and turn-on fluorescence in dyes (**a**) **FLUO-3**, used in[23,29] and (**b**) **18c6-an**, developed for this work.

As recognized 17 years ago,[25] in experiments using the isotope ^{136}Xe, efficient and selective detection of the daughter nucleus ^{136}Ba^{2+}, accompanied by electron energy measurements of precision better than ~2% FWHM to reject the two-neutrino double beta decay background, could provide an effective background free approach to search for 0νββ. Recently, single-atom or single-ion-sensitive detection methods for the detection of barium have been demonstrated, emerging from various disciplines in physics and chemistry.[26,27] As yet, no sensor capable of direct deployment within the working medium of a running detector has been produced.

A key consideration differentiating barium tagging approaches in LXe and GXe experiments is the charge state of the daughter nucleus. Barium from double beta decay is born in a highly ionized state Ba^{N+} that quickly captures electrons from neutral Xe until further capture is energetically disfavored, stopping at Ba^{2+}. In LXe, recombination with locally thermalized electrons causes further neutralization, leading to an ensemble of ionic and atomic species[28] including Ba and Ba^{+}. The lack of recombination in GXe, on the other hand, implies that Ba^{2+} will be the predominant outcome.[16] Optimal technologies are likely to be distinct for detection in these two cases.

Barium tagging approaches for LXe[29] have previously been focused on atomic fluorescence transitions of the outer electron in Ba^{+}, or in some cases, neutral Ba.[30] Ba^{2+}, on the other hand, has a noble-like electron configuration without low-lying fluorescence transitions. To detect Ba^{2+} using fluorescence techniques it is necessary to add such transitions artificially. One such method was proposed in[31] and further developed in[4], using single molecule fluorescence imaging (SMFI). SMFI and super-resolution techniques, resulting in the 2014 Nobel prize in chemistry, are widely used in biology for sensing Ca^{2+} ions at the single ion level.[32-37] In SMFI detection of cations, a suitable fluorophore-containing molecule is employed that is nearly non-fluorescent in isolation but becomes highly fluorescent upon chelation of a target ion (**Figure 2**). The fluorescence enabled upon binding can be observed by probing with an excitation laser and collecting the fluorescence light using single-photon-sensitive EM-CCD cameras. The range of applicability of SMFI dyes is wide, including in solution and inside living cells. This work focuses on the adaptation of SMFI for sensing of dications in dry gaseous environments at the solid-gas interface.

2.2. Development of SMFI dyes for dry-phase barium ion sensing

A cross-disciplinary effort has been underway since 2015 to develop barium tagging techniques for high-pressure xenon gas detectors using single-molecule fluorescent imaging. In exploratory work, we demonstrated that commercially available calcium chemosensors **FLUO-3** and **FLUO-4** are sensitive probes for Ba^{2+}, thus making them potentially promising barium tagging agents.[4] Using total internal reflection fluorescence microscopy[38] (TIRFM) with **FLUO-3**, the first single barium dication fluorescence detection was then demonstrated.[26] Individual ions were spatially resolved with 2 nm super-resolution and identified with 13 σ statistical significance over background via their sharp photo-bleaching transitions.

FLUO-3 and **FLUO-4** are formed from a 1,2-bis(*o*-aminophenoxy)ethane-*N*, *N*, *N'*, *N'*-tetraacetic acid (BAPTA)-like receptor that is covalently bound to a fluorescein-like fluorophore. On-off fluorescence response in the **FLUO** family arises from quenching of the fluorescein group, presumably by photo-induced electron transfer from the electron-rich BAPTA species (likely involving the electrons on the adjacent nitrogen atom, see **Figure 2**, left). When unbound to an ion, electrons may move freely into the fluorescein group to quench excited states and inhibit fluorescence. In the presence of Ba^{2+}, the electronics of the BAPTA-like receptor are altered, effectively by Lewis acid-base complexation with the nitrogen's lone pair electrons. This inhibits the donation of electrons into the excited fluorescein group, and prevents the fluorescence quenching, switching on a fluorescent response. These changes in fluorescent quenching states can be probed by laser excitation at an energy just above the fluorescence transition.

The majority of contemporary SMFI work has been performed in solution, often with molecules in pockets of liquid suspended in a polymer matrix. For example, our previous work[26] used **FLUO-3** suspended in polyvinyl alcohol to detect ions from barium perchlorate solution. On the other hand, the xenon gas within 0νββ experiments must be free of impurities such as water at the part-per-trillion level, which is achieved through continuous circulation and purification with hot and cold getters.[39] Any water-based sensor is therefore inappropriate for this application, and a dry-phase barium chemosensor is required. Our studies of the **FLUO** family implied they will be unsuitable for barium detection in the dry phase, for two reasons: (1) binding of BAPTA to Ba^{2+} requires deprotonation of four carboxylic acid groups and reorganization of the various points of binding, not expected to occur effectively in a dry state (**Figure 2**). (2) While fluorescein is a bright fluorophore in solution, the fluorescence is suppressed when dried.[40]

Similarly, most ion-sensing work in SMFI focuses on calcium detection, due to its relevance as a signaling agent in biological systems. Some prior work on chemosensors for barium ions has been reported,[41-43] but barium sensing remains a relatively unexplored sub-field.

We have thus initiated an interdisciplinary program to develop and test barium-sensitive molecules for use in the dry phase, to enable barium tagging in high-pressure xenon gas. The requirements for a barium chemosensor suitable for ion tagging in 0vββ include (1) relatively long-wavelength excitation and emission, suitable for transmission through microscope optics (in practice both excitation and emission longer than 350 nm); (2) bright fluorescence of the “on” (barium-bound) state in the dry phase; (3) a strongly suppressed “off ” (barium-unbound) state in the dry phase; (4) A sufficient Stoke’s shift to allow dichroic separation of excitation and emission light; (5) binding that is strong enough to reliably capture ions but weak enough that residual ions can be washed from the sensor with a competing stronger receptor before installation (likely anything in the range of dissociation constants $K_d \sim 10$ μM to few mM range is suitable); (6) ability to chelate ions at the gas-solid interface; (7) stability under a dry noble gas environment. In this work, we address points 1 through 5. Points 6 and 7 depend sensitively on the form of the final coating, envisaged here as a self-assembled and covalently tethered monolayer on a thin trans-parent surface, to be developed and addressed in future work.

In order to identify daughter ions at a sensing region of an 0vββ experiment, they must first be transported from the position of the decay to the sensor. There are various lines of technological development being pursued to address this question. The NEXT collaboration[44] is undertaking R&D on RF carpet structures[45] to achieve electric-field driven transport in high-pressure xenon gas detectors. A proposed scheme for barium tagging in liquid xenon also involves RF methods,[46] in this case, to extract from gas ullage into an evacuated region. This could be coupled with the mechanical actuation of a cold finger to extract frozen ions from a liquid into the gas.[47] For a realistic application, the efficiency of the barium tagging process incorporating both transport and detection must be high. A dense monolayer of molecular probes may plausibly exhibit an ion tagging efficiency near one. Establishing this number will require detailed ion-by-ion characterization in the dry phase, a test we plan to undertake at the University of Texas at Arlington as a future step in this program.

Considering the need for molecular structures that function in dry systems, aza-crown ethers appear to be an ideal candidate for photo-induced electron transfer (PET)[48] modulated turn-on SMFI techniques. They have been successfully used for the capture of various earth and earth alkali metals in both protic and aprotic solutions and their nitrogen can be placed in a fashion to modulate the excited states of various fluorophores (including organic dyes, nanoparticles, and hybrid fluorophores).[49-52] As binding domains for alkali earth metals, aza-crown ethers demonstrate slightly higher K_d values as compared to their all-oxygen crown ether precursors.[53] Their binding, however, is expected to achieve similar selectivity based on size considerations and the pre-organized (conformationally restrained) ring systems. **Figure 2** demonstrates the chemical bonding model supported by crystal structures and NMR experiments, depicting binding by cooperative Lewis base donation of lone pair electrons of the crown ether oxygens and nitrogen to cations and other Lewis acidic guest molecules. Aza-crown ethers may be covalently linked to fluorophore molecules through their nitrogen atom, forming tertiary amines or secondary amides, allowing for divergent synthesis of various classes of fluorescent sensors. Both amine and amide functional groups act as "switches" for modulation of light and dark states in tethered fluorophores[54]-although, these two moieties display different PET donation abilities to acceptor fluorophores and innate stability. Stemming from the structural arguments above, the aprotic and preorganized binding domain of aza-18-crown-6 ether was envisioned for optimal chelation of Ba^{2+}. The aza-15-crown-5 ether has a relatively smaller size and, in some cases, has been shown to chelate Ba^{2+} in a termolecular, sandwich-like complex with a 2:1 ratio of crown-ethers to Ba^{2+}.[43,55] Aza-21-crown-7 ether, with its larger ring size is thought to result in weaker/longer bonds to metal ions, which cannot overcome the entropy and flexibility seen in larger ring systems.[56,57]

When considering fluorophores for sensitive function, especially in dry and solid states, it is common to select more rigid aromatic or heteroaromatic fluorophores, which are relatively photostable and undergo less structural reorganization and non-radiative deactivation pathways after excitation.[58] We chose to investigate pure arenes (all carbon and hydrogen aromatic fluorophores) in this initial investigation of functional SMFI molecules because of their robust nature, ease of synthetic tailoring, and relatively weak intermolecular interactions with barium ions. This paper presents the first family of molecules designed specifically for this purpose, experimentally investigating aza-crown ether binding site of various sizes bound through the crown-ether amine to a methyl aromatic fluorophore, creating benzylic nitrogen "switch" to regulate rigid aromatic fluorophores, pyrene, and anthracene.

In this paper, we present both wet and dry-phase barium-induced fluorescence in eight molecules constructed from four nitrogen-containing binding sites: 1-aza-15-crown-5 (15c5), 1-aza-18-crown-6 (18c6), 1-aza-21-crown-7 (21c7), and a diethanolamine linear fragment of the aza-crown ethers (lin); and two fluorophores: pyrene (py), anthracene (an). The molecules developed for this work are shown in **Figure 2.1**.

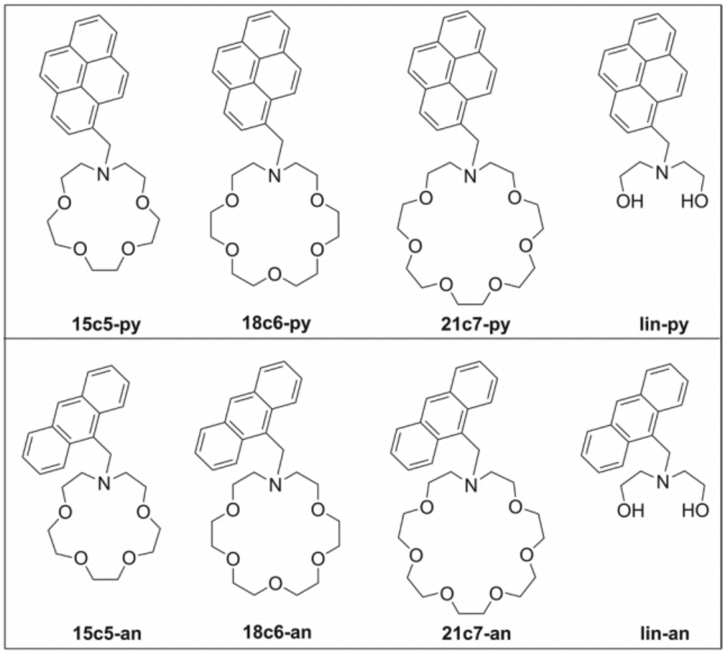

Figure 2.1. Molecules developed for dry barium sensing in this work.

The synthesis of the fluorophores were carried out in a divergent method. **18c6-an's** synthesis is shown in **Figure 2.2** as an example. (See the Supplementary Information for detailed experimental methods for all molecules studied in this report, including chemical characterization and spectra for all intermediates and final products.) Our synthesis began with the preparation of various protected diethanolamines, settling on *N*-benzyl diethanolamine (I)[63] to be cyclized with the activated ditosylate (OTs, II-b).[64] Cyclization of I and II-b was achieved most efficiently under a reported method that used phase transfer conditions[64] to yield the *N*-benzyl-aza-crown ether, which was deprotected by standard hydrogenolysis to provide 1-aza-18-crown-6 ether (III-b) in good yield. 9-bromomethylanthracene (IV-b)[65] was prepared in excellent yields by radical bromination and underwent an SN_2 displacement by (III-b) to provide **18c6-an** in reliable yields.

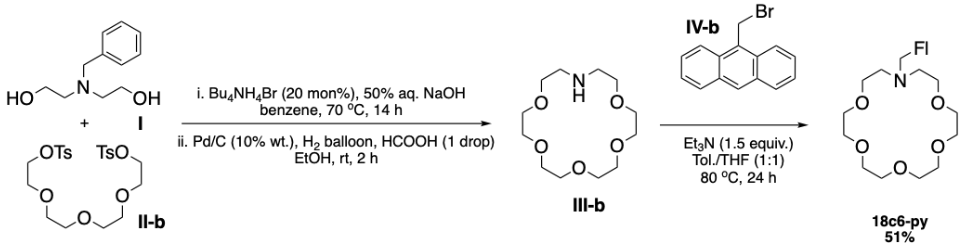

Figure 2.2. Example synthesis of 18c6-an.

2.3. Characterization of barium sensors in solution

The fluorescence intensity of unbound and barium-bound fluorophores were first studied in solution ("wet studies"). In order to achieve solubility of the pyrene and anthracene derivatives, a solvent mixture of 10:1 TRIS buffer and acetonitrile mixture was used. Protonation of the nitrogen "switch" was observed to lead to a non-quiet off state in neutral, un-buffered solution, and so the buffer was prepared to pH 10.1 to enhance the on-off ratio. Some residual activity in the off state was still observed even at this higher pH. Data that will be shown in Sec. 2.4 are suggestive that the residual off-state fluorescence is largely induced by solvent effects which are not present in the dry phase.

The intensity of fluorescence was measured as a function of wavelength between 300 and 550 nm. For each fluorophore a **2D** emission/excitation spectrum was recorded to establish the most efficient excitation wave-length λ_{max}, with an example for 18c6 shown in Appendix B **Figure 2.3.1** Experimentally we found that λ_{max}, ~342– 344 nm for the pyrene derivatives and λ_{max}, ~366–368 nm for the anthracene derivatives. To avoid quenching and excimer formation effects observed at higher concentrations, relatively weak solutions of 2 μM were used. These concentrations are lower than the preliminary results reported in[40]. The various species were first compared at a fixed barium concentration of 37.5 mM to establish relative sensitivity. These data are shown as solid lines in **Figure 2.3**, where the curves are normalized to the intensity of the "off " state at the longest wavelength emission peak (as indicated on the y-axes).

The linear systems are not expected to capture barium in solution but were included as control systems for wet and dry fluorescence. As expected, we observed no significant increase in fluorescence from these species on addition of barium ions. The strongest fluorescence response was found for the 18c6 species, which is consistent with expectations based on size-matching of the ion and the receptor site.[59]

A smaller but still significant response is observed in some other molecules, including **21c7-an** and **15c5-py**. We also found that the absence of an observable fluorescent barium response in 2 μM **15c5-an** could be alleviated by working at higher concentrations of 90 μM or above, as shown as a dashed curve in **Figure 2.3** and in[40]. However, at these concentrations, efficient saturation could not be achieved without substantial excimer formation in some samples[60] in dry data (see Sec. 2.4), and so we continue most studies at the lower concentration point of 2 μM.

The brightest barium response at 2 μM fluorophore concentration was observed in **18c6-an**, and as such, this molecule is selected as the basis for more detailed studies. A Job's plot study demonstrated that **18c6-an** binds with Ba^{2+} in the ratio 1:1, shown in **Figure 2.11.** ^1H NMR experiments of both **18c6-py** and **18c6-an** with or without barium perchlorate in 1:1 ratio in CD_3CN suggest the involvement of nitrogen and oxygen lone pairs in interaction with barium cations as indicated by the downfield shift of all proton signals in the aza-crown ether ring and the benzylic protons located between the nitrogen and anthracene. More subtle effects are observed in the aromatic region, showing a likely small field effect on the anthracene ring upon binding. Similar binding experiments with acyclic lin-an show minimal downfield shifts, indicative of less effective barium-fluorophore binding with those receptors. Two illustrative examples are shown in **Figure 2.9**.

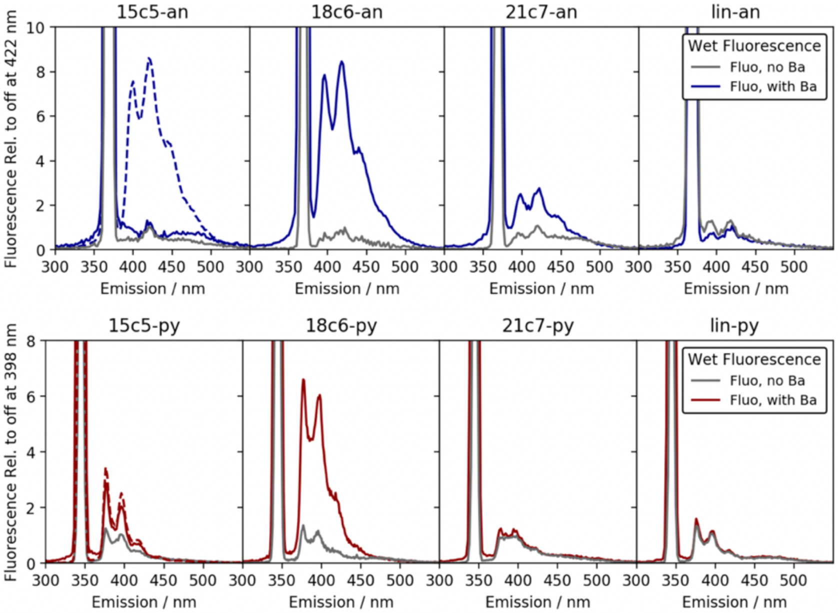

Figure 2.3. Fluorescence response of each species in solution at a concentration of 2 μM and barium at 37.5 mM. In each panel, the grey line shows the emission contribution from scattering and fluorescence in the buffer alone. The colored lines show the response with barium added. The dashed line shows a higher concentration study for comparison, with the 15c5 fluorophores at 90 μM.

Titration studies of barium into the anthracene derivatives are shown in **Figure 2.4**. For the pyrene derivatives, similar studies were undertaken but found to be less reliable, possibly because of relatively slow solvation rates paired with increased rates of oxidative degradation of pyrene in our solvent system leading to larger fluctuations in a batch-to-batch manner. The error bars in **Figure 2.4** reflect the observed variability between repeated runs at the same concentration point. The overlaid fit functions reflect the functional form associated with a 2-body association/dissociation reaction, with the error bands showing 68% frequentist intervals at each barium concentration, accounting for correlated variations in the value of K_d and the saturation fluorescence. The extracted K_d values from the fits of **Figure 2.4**, right are: **15c5-an** K_d = 0.988±0.008 mM; **18c6-an** K_d = 16 ± 4 mM; **21c7-an** K_d = 0.68 ± 0.01 mM. The uncertainties reported there are statistical only, but some variance between repeated titrations suggests the uncertainty on each K_d should be larger than this due to systematic effects. We attribute an additional 20% systematic uncertainty to each measured K_d value on this basis, and so report **15c5-an** K_d =0.98 ± 0.20 mM; **18c6-an** K_d = 16 ± 5.2 mM; **21c7-an** K_d = 0.68 ± 0.13 mM. The general values are reasonable when compared to measured binding constants for all-oxygen crown ethers interacting with barium cations in water.[61]

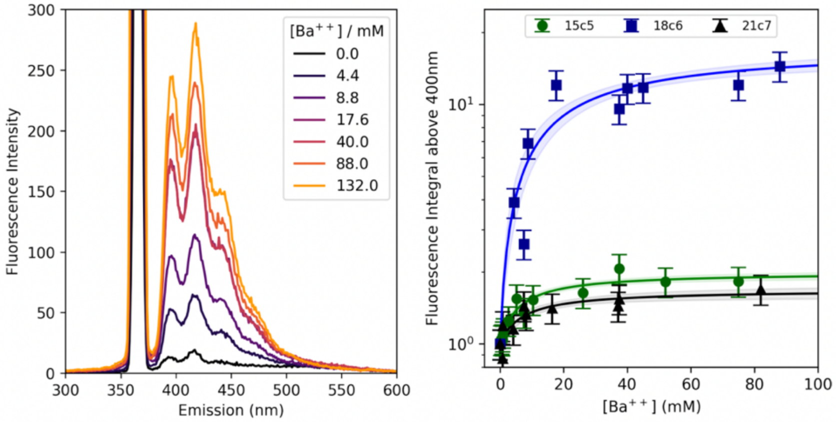

Figure 2.4. Left: Titration study showing an increase in fluorescence intensity with added barium to **18c6-an**. Right: Titration curves for anthracene derivatives with fits for K_d overlaid.

The fluorescence in the wet phase is strongly influenced by the solvent. The addition of a Triton-X above its critical micelle concentration in our solvent system was studied, to produce a protective non-aqueous environment around the molecule suspended in a microemulsion, potentially more representative of the environment expected in the dry phase. For both **15c5-py** (90 μM) and **18c6-py** (2 μM) solutions, the micelle substantially improved the fluorescent response of the system, as shown in **Figure 2.5**, left. This offers the promise that the dry response may be expected to be innately (or tailored to be) stronger than the wet response for these molecules. For anthracene derivatives, no substantial change was observed with the addition of the micelle, which suggests that protection of the fluorophore from quenching rather than protection of the receptor from disturbance may be the dominant effect leading to improved performance for pyrene fluorophores.

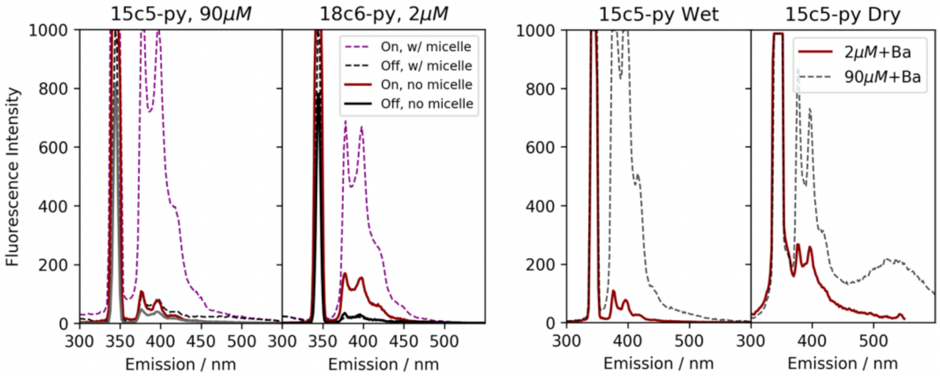

Figure 2.5. Left: Effect of micelles on **15c5-py** and **18c6-py** species, showing the significant solvent effect on fluorescence in the wet state. Right: effect of increasing **15c5-py** concentration. A direct increase in primary fluorescence is observed in solution, whereas an excimer peak emerges in dry samples.

2.4. Characterization of barium sensors in the dry phase via spectroscopy

Dry fluorescence studies of pre-chelated solutions were performed by drying 8–10 drops of each wet sample on a glass plate. The samples were dried by heating the glass on a hot plate at a temperature 120 °C. Two-dimensional emission/excitation scans were again used to establish λ_{max}, with no significant shifts observed relative to wet studies. The fluorescence intensity measured at λ_{max} is reported at wavelengths between 300 and 550 nm for samples without and with 37.5 mM added barium in **Figure 2.6**. Broadly we observe the same trends as in the wet studies, with 18c6 demonstrating the strongest response.

In the dry phase, an additional complication is present, which is that the glass and dried buffer are found to introduce some level of scattering and fluorescent response, shown in grey in **Figure 2.6**. The effect is much larger for the pyrene species, which are excited at 344 nm, than for the anthracene derivatives, excited at 368 nm. Fluorescence from the dried fluorophore with no barium is found to be negligibly different from the glass/buffer control system in all cases, suggesting that the isolated molecules are extremely quiet in the dry phase when unchelated. This lends support to the hypothesis that the off-state fluorescence is a largely solvent-induced effect, caused by interaction between the nitrogen group and residual protons in the solvent.

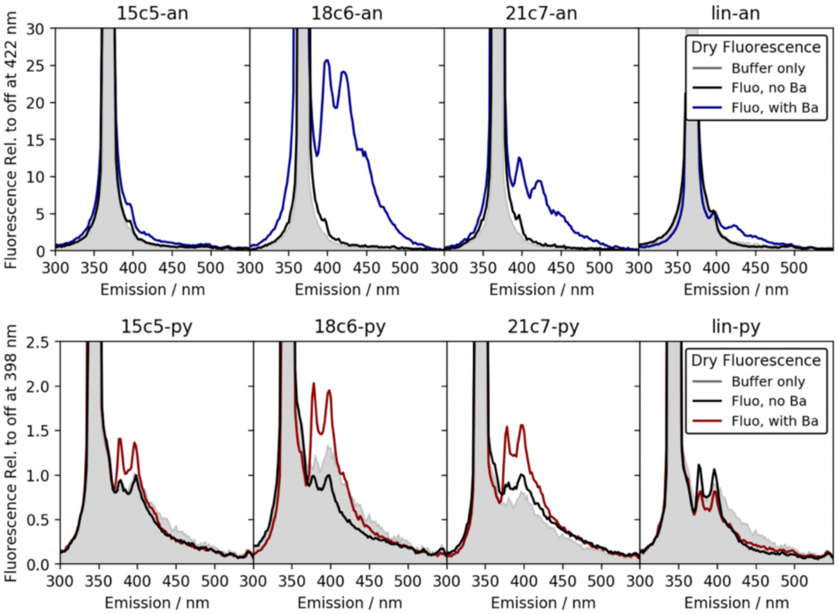

Figure 2.6. Fluorescence response of dried films of fluorescent barium sensing molecules in buffer. In each panel the grey line shows the emission contribution from scattering and fluorescence in the buffer alone. The black line shows the emission contribution from un-chelated fluorophore in buffer, and the colored lines show the response with barium added.

All anthracene derivatives show a fluorescent response to barium cations in the dry phase, with **18c6-an** again being the strongest, followed by **21c7-an**. The linear system here also shows some response, likely due to the co-precipitation of barium when rapidly solidified on the scanning surface. The pyrene derivatives show some response, with **18c6-py** being the strongest, but the response is more difficult to observe over the buffer/scattering background.

As in the wet studies, both 15c5 responses to barium are weak. Following a similar strategy to the wet samples, we also tested a higher concentration sample of **15c5-py** in the dry phase, shown in **Figure 2.5**, right. In this case, a large increase in fluorescence is observed in the dry phase, but at much longer wavelengths than the expected pyrene monomer emission. This emission at 525 nm derives from the pyrene excimer,[60] and thus represents a collective effect of fluorescence between multiple pyrene groups. This emission is the likely origin of the intense dry fluorescence reported in,[40] given the optical configuration used there. Because the excimer likely requires barium binding to two fluorophore molecules simultaneously, it is not of direct interest for the goal of single-molecule imaging at a self-assembled monolayer consisting of these chemosensors.

2.5. Characterization of barium sensors in the dry phase via microscopy

The most promising compound identified in this work is **18c6-an**. It binds strongly to barium in solution, maintains fluorescence in the dry phase, and has spectroscopic properties amenable to microscopy, with both excitation and emission at fairly long wavelengths, and a large enough Stoke's shift to allow dichroic separation of excitation and emission. Samples of dried on- and off-state **18c6-an** were examined under a fluorescence microscope, to establish that bulk fluorescence is detectable microscopically.

Using total internal reflection microscopy (TIRFM),[38] the fluorescent response of 18c6-an was measured both with and without exposure to Ba^{2+}, alongside blank coverslips tested as a control to monitor the level back-scattered light and camera noise.

The slides were prepared by sonicating first for 20 minutes in a mixture of one-part Liquinox Cleaning Solution and ten parts deionized water, and then again in only deionized water for ten minutes. The slides were then left to soak in 6 M nitric acid for four hours in order to remove any remaining metal impurities on or near the surface of the slides. The slides were then thoroughly washed with Ultra-trace water and rinsed in a buffer solution in order to neutralize any remaining acid before a final water rinse.

In order to assess the removal of residual Ba contamination from the glass slides, two tests were performed. In one test, two sets of three cleaned and three uncleaned slides were rinsed with 2 mL of 18 MOhm deionized water, acidified with 80 mL 8 M Optima Grade nitric acid to make solutions of 2% HNO_3 and analyzed via inductively coupled plasma mass spectrometry (ICP-MS). Determinations of 2.06 ± 0.77 and 18.8 ± 5.8 pg Ba were made among the three cleaned and uncleaned slides, respectively, for a reduction factor of 9.1.

In a second test, in individual vials, cleaned and uncleaned slides were sonicated in 20 mL of 5% (v/v) HNO_3 in a 40 °C bath for 99 minutes and allowed to soak overnight. Determinations of 90.1 ± 0.8 and 746 ± 2 pg Ba were made from the leachates of the cleaned and uncleaned slides, respectively, for a reduction factor of 8.3. Detection limits of 1 fg Ba were calculated (3 × standard deviation of the process blanks, n = 3).

After allowing cleaned slides to dry, each was heated to 100 °C and 37.5 μL of barium enriched and barium free **18c6-an** were deposited on the glass drop-wise until dry. This forms a fluorescent spot of area around 9 mm^2.

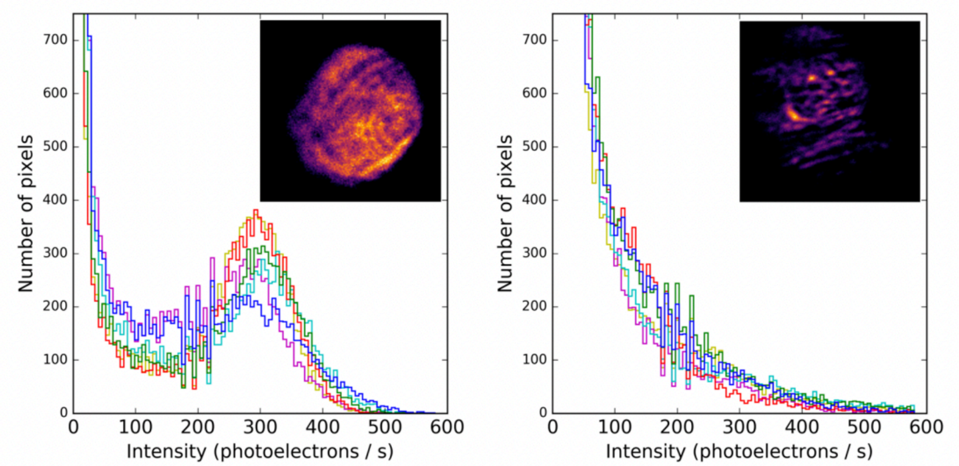

Figure 2.7. Example of barium-chelated (left) and unchelated (right) fluorescence microscope images. The histograms show the pixel intensity populations, with a clear excess visible in the "on" slide. The multiple colored histograms are various locations within the fluorescent spot, chosen at random. The insets show two example microscope images at specific locations.

The coated slides are then imaged in a system that resembles that used to image single molecules in[26]. The optics of the system were switched to a set appropriate for anthracene fluorescence, incorporating a 450 nm short pass emission filter, 400 nm immersed, high numerical aperture, 100X objective lens. The light coming from the objective lens is then bent through the different refractive indices of the glass, oil, glass, and air in its path, allowing the excitation of only the molecules at the surface interface. The fluorescent response for each sample from this excitation was then recorded using a Hamamatsu EM-CCD camera, at one second of exposure. This was repeated for six positions on each slide, with three slides of each type (fluorophore with no barium, fluorophore with barium, blank control slide). Example pixel intensity histograms and images for one on-state and one off-state sample are shown in **Figure 2.7**. The fluorescent response for the on the state of **18c6-an** is visibly higher overall than that for the off state in this example.

In order to quantify the effect in aggregate, the total intensity within the region of interest above one hundred photoelectrons was summed for each point on each field of view on each slide. The resulting fluorescence intensity measurement per slide is shown in **Figure 2.8**. The off-state slides do not show significant activity above the blank slide baseline, but a clear increase in fluorescence in the barium-chelated samples is observed. Some time-dependent degradation of the off-state was observed when exposed to air for multi-hour periods, likely due to aerobic oxidation of the SMFI species' switchable nitrogen[62]. To mitigate any biasing effect the data were taken with alternating on and off slides one after the other. Both the clear distinction between on- and off-state fluorescence and the gradual increase with time are visible in **Figure 2.7**. These data demonstrate that **18c6-an** has appropriate spectroscopic properties for dry barium chemo sensing via fluorescence microscopy.

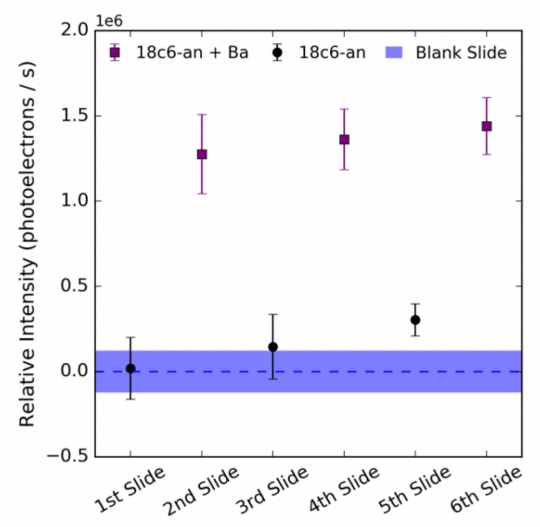

Figure 2.8. Measured response of dry barium-chelated vs. unchelated microscope slides excited at 365 nm under fluorescence microscope. Each error bar represents the 1σ spread if intensities within a single slide, and each point represents an independently prepared slide. A clear enhancement of the "on" state relative to the "off " state is visible.

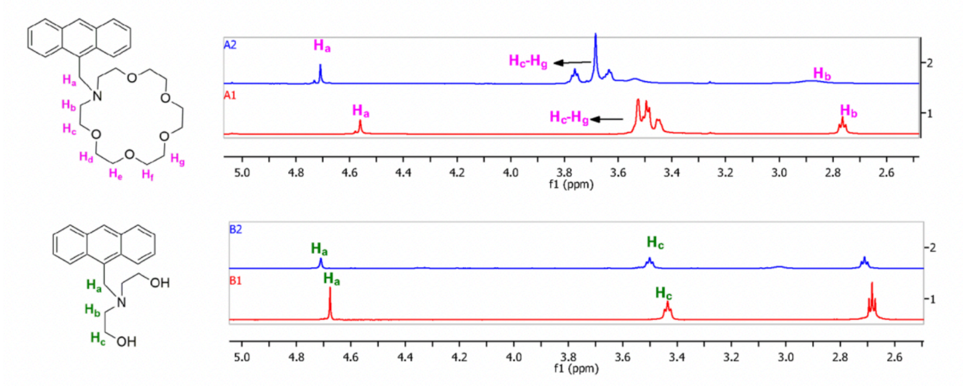

Figure 2.9. NMR experiment showing barium binding in **18c6-an** and lin-an. Bottom (red) traces show fluorophore without barium, and top (blue) traces show fluorophore with barium in 1:1 ratio. Lone pairs are coordinated to barium, leading to decrease in electron shielding around the proton labelled as H*a* in the 18c6 receptor. The similar proton shows much smaller shift in the lin receptor, which does not have a strong tendency to bind barium.

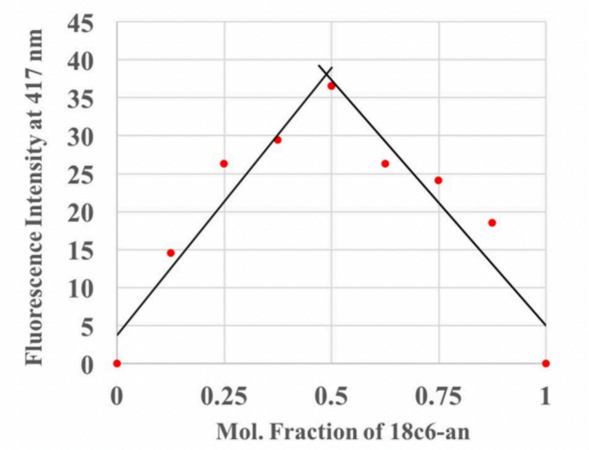

Figure 2.10. Job's plot of **18c6-an** and Ba^{2+} with total concentration of 40 μM, which demonstrates a 1:1 binding stoichiometry.

2.6. Conclusion

We have studied a family of molecules designed for dry-phase barium chemosensing, based on azo-crown ether species bonded to small rigid dye molecules via a nitrogen switch. Barium responsiveness shows a clear trend with 18c6 giving the strongest response, with intermediate responses observed in 15c5 and 21c7 receptors, and no in-solution response from the linear molecules, which are ineffective for binding barium. Titration studies were undertaken, establishing K_d values for all anthracene-based species.

Dry phase fluorescence was studied spectroscopically, with 18c6 derivatives again showing the strongest response in pre-chelated and dried samples. For all the anthracene derivatives, the off-state of the sensor molecule becomes negligible in the dry phase, with the only background deriving from residual scattering and low level fluorescence in the glass and buffer. This is suggestive that any off-state fluorescence in the wet studies is attributable to solvent effects, likely protonation of or hydrogen-bonding to the nitrogen group preventing it from inhibiting fluorescence. Based on these studies, **18c6-an** was identified as the most promising candidate for further work.

The fluorescence enhancement from barium chelation was tested under an inverted fluorescence microscope, in conditions similar to those used previously for single-molecule imaging of barium ions by **FLUO-3**. We observe a significant increase in fluorescence for the barium-bound vs unbound samples, showing that this family of dyes has appropriate spectroscopic characteristics for imaging of barium ions in the dry phase.

Single-molecule response has not been demonstrated in this work since the aggregation and crystal structure of the dried dye prohibits observation of distinct and separated fluorescent molecules. The next stage of this R&D program will address this by self-assembling a monolayer containing **18c6-an** onto a glass surface, presenting a well-organized and dispersed fluorescent sensing layer. Based on the spectroscopic properties of **18c6-an** established in this work, and its strong on-off response in the dry phase exceeding that of **FLUO-3** in solution,[4] we expect to be able to resolve individual barium-bound molecules within the dry layer following barium binding, once the monolayer has been assembled.

The path to single-molecule imaging using this class of fluorophores will build upon our past work in[26], using total internal reflection fluorescence microscopy to identify near-surface ions, first within polymer matrices and then in surface-tethered monolayers. The UV excitation of these new molecular probes presents some new challenges in terms of eliminating substrate fluorescence, which can be overcome either with the use of low-fluorescence materials or by extending the structures we have demonstrated to analogs with visible excitation and emission. These topics will be the subject of future publications.

Demonstration of a class of molecules with a dry fluorescent barium response, observable via TIRF microscopy, is a significant advance in the development of barium tagging in high-pressure xenon gas. Since the single-molecule fluorescence imaging approach is applicable directly at atmospheric or elevated pressures, these new species of barium chemosensors open a viable path to *in-situ* barium ion detection within a high-pressure xenon gas detector. Demonstrating performance at the single-molecule level in noble gases is the next important step. With this new family of chemosensors for dry SMFI in hand and single ion sensitivity to barium already reported in the wet phase,[26] a near-term demonstration of single barium ion detection in dry xenon gas appears within reach.

Chapter 3

Demonstration of Selective Single-Barium Ion Detection with Dry Diazacrown Ether Naphthalimide Turn-on Chemosensors

Pawan Thapa, Nicholas K. Byrnes, Alena A. Denisenko, James X. Mao, Austin D. McDonald, Charleston A. Newhouse, Thanh T. Vuong, Katherin Woodruff, Kwangho Nam, David R. Nygren, Benjamin J.P. Jones, and Frank W. Foss, Jr.

(Part of this work has been published in *ACS Sens.* 2021, 6, 192-202).

3.1. Introduction

Single-ion sensing techniques at gas−solid interfaces have the potential to enhance our structural understanding of dynamic supramolecular events on conventional solid detectors. We turned our attention to the development of functional materials for such a process when tackling one of the great open questions of particle physics,[10] whether or not the neutrino is its own antiparticle. The detection of barium daughter ions generated by double beta decay in liquid or gaseous xenon has been termed "barium tagging"[25] and is becoming a vibrant area of R&D in particle and nuclear physics.[69,70] The detection of individual Ba^{2+} ions would greatly improve detection sensitivities over background processes due to radioactivity because only the double beta decay of the ^{136}Xe isotope is expected to produce Ba^{2+} ions within a radiopure particle detector. This would enhance searches for the hypothetical radioactive process of $0\nu\beta\beta$ with a signal that is orthogonal to the radiation-based events currently measured. A robust observation would demonstrate that the neutrino is a Majorana particle—its own antiparticle—altering our understanding of neutrinos and the early history of the Universe. One possible implementation of barium tagging employs single-molecule fluorescent imaging (SMFI) with chemosensors that exhibit turn-on fluorescence in response to barium chelation.[6,71] The limited arsenal of barium sensors does not possess the proper binding and/or fluorescent characteristics necessary for SMFI at dry gas−solid interfaces. While the structural requirements for barium tagging are explored, one may envision the application of such an approach to the broader development of sensing materials at gas−solid interfaces for environmental and industrial applications.

Fluorescent chemosensors are sensitive analytical tools for rapid chemical and biochemical measurement.[72-74] Properly incorporated within SMFI experiments, they reveal individual molecular events and fundamentals, whose significance is unavailable through bulk analysis. We investigated 4-amino1,8-naphthalimide fluorophores because they exhibit many favorable properties but have not been demonstrated for selective barium sensing.[75,76] Synthetically tractable 4-amino1,8-naphthalimides allow construction of both photoinduced electron transfer (PET) and intramolecular charge transfer (ICT) fluorescent sensors.[77] Relatively large Stoke's shifts and high photostability features are beneficial for high signal-to-noise ratios.[78] Likewise, crown ethers afford enhanced efficiency in binding to metal ions and can act as switches for PET- and ICT-based sensors without the need for proton transfer or metal ion exchange that renders other molecules useless in solventless environments.[79] As such, 4-amino-1,8-naphthalimide fluorophores with crown ether-based binding domains have been used as colorimetric and fluorescent sensors for the detection of ions and small molecules that are of great significance to the environment, human health, and industrial processes.[80-83] Several 4-amino-1,8-naphthalimide chemosensors have been developed for detection of cations, anions, and small polar molecules.[84-87] However, chemosensors with selective response to Ba^{2+} remain underdeveloped.[74,88]

Selective barium sensing has been demonstrated by a relatively small number of fluorescent chemosensors.[42,74,88-96] This is not surprising because barium sensing is not widely studied for clinical or environmental reasons; although acute barium exposure can be deadly, diagnoses are rare and often confirmed by inductively coupled plasma mass spectrometry analysis of the patient's plasma and urine.[97,98] Nakahara and co-workers pioneered a monoazacryptand receptor with a PET switch to pyrene fluorescence that operates in aqueous micellar systems and would require relatively high-energy excitation that would make SMFI challenging in our system.[37,41,99] Crown ether systems have invoked termolecular complexes with two crown moieties sandwiched around one Ba^{2+}, which would also be limited in dry-phase sensing, where bimolecular interactions may be preferred.[43,88] A bioinspired G-quadruplex chemosensor provided rapid detection of Ba^{2+}, also in solution.[100,101] Recently, a fluorescent chemosensor based on the phenoxazine system with an ICT turn-on mechanism was reported for Ba^{2+}, where charge transfer was achieved by metal binding specifically to a single amide functional group.[102] These receptors are instructive but unsuitable for long-term dry phase SMFI device design, presumably as part of a functional monolayer or thin coating deposited on a translucent optical device.

Within the context of R&D toward a barium-tagging phase of the NEXT program's search for 0νββ decay,[15,39,103] we previously demonstrated single-ion sensitivity to Ba^{2+} using commercial chemosensors in an aqueous suspension.[70] Achieving single-ion sensitivity mandated the use of the competitive binding agent BAPTA and used fluorophores incompatible with dry operation. To address the challenge of solventless sensing of barium, we demonstrated a class of dry phase active fluorescent chemosensors using monoazacrown receptors.[99] Single-molecule sensitivity of this system[99] was elusive because of UV excitation of impurities in the substrates and a lack of photobleaching transitions to use for single-molecule identification. Similar molecules were then recently shown to be suitable for ratio metric or "bicolor" Ba^{2+}-sensitive fluorescence,[104] a promising new direction under consideration for barium tagging.

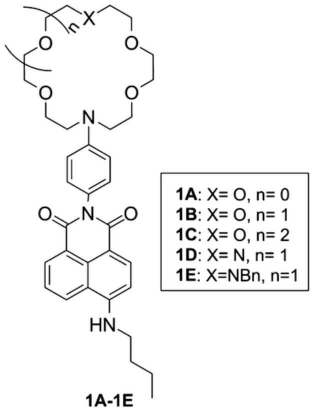

1A-1E

Figure 3. Naphthalimide derivatives used in this study.

In this paper, we report a study on the synthesis, characterization, analysis, and computational modeling of a new family of monoazacrown ether and diazacrown ether naphthalimide fluorescent sensors (**Figure 3**) with enhanced selectivity and sensitivity to Ba^{2+}. These visible fluorescent probes are amenable to SMFI microscopy in dry environments and consequently allowed us to resolve individual Ba^{2+} ions without a competitive binding agent. This improves upon our initial sensor dyes,[99] with visible excitation proving to be a critical ingredient in overcoming fluorescent backgrounds of glass and quartz substrates at the level required for singlemolecule sensitivity. We also report on computational models that offer reliable predictability of target ion- and binding sitedependent fluorescent response within this family, a capability that will accelerate explorations of structure−function relationships in future dry-phase SMFI probes.

3.2. Experimental section

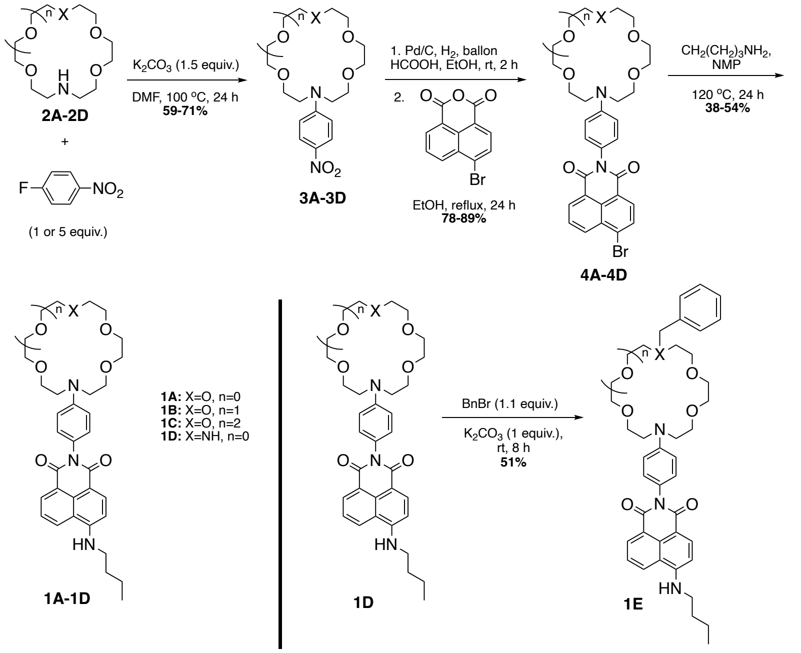

Scheme 3. Synthesis of 4-Amino-1,8-naphthalimide Sensors.

3.2.1. Synthesis

The synthesis of naphthalimide derivatives **1A−1E** is shown in **Scheme 3.** Monoazacrown ethers **2A−2C** were assembled as previously described.[64,99] Diaza-18-crown-6 ethers were prepared by the modification of methods from a previous report.[105] Complete details and full chemical characterization can be found in section Appendix B2.

3.2.2. Sample Preparation for Solution-Phase Studies

Stock solutions of probe molecules were prepared at 1 × 10^{-3} M concentration in an acetonitrile solvent. Stock solutions of metal perchlorates were made at 1 × 10^{-2} M concentration in a 9:1 acetonitrile/water mixture. UV−vis studies were performed with and without Ba^{2+} in acetonitrile, dichloromethane, acetone, and ethanol solvents with probe **1B** (10 × 10^{-6} M) and barium perchlorate (50 × 10^{-6} M). Fluorescence titration and metal ion selectivity studies were performed by maintaining a final concentration of the probe molecule at 1 × 10^{-6} M concentration. Metal ion selectivity studies were conducted by maintaining metal perchlorate concentrations at 5 × 10^{-6} M. Competitive fluorescence experiments were performed using 2× 10^{-6} M probe **1D** with 5 × 10^{-6} M metal perchlorate solution in an acetonitrile solvent. Job's plot experiments were performed by maintaining a total concentration of the probe and barium perchlorate solution at 20 × 10^{-6} M. Samples were incubated for 2 min in the dark before measuring fluorescence intensity. ^{1}H NMR titration experiments were conducted with the concentration of the probe at 1 × 10^{-2} M and metal perchlorate (barium, potassium, and mercury) at 1 × 10^{-2} and 5 × 10^{-2} M in an acetonitrile-d_3 solvent at room temperature.

3.2.3. Slide Preparation for Dry-Phase Fluorescence

Dry samples of probe **1D** on glass slides for dry-phase fluorescence studies were prepared as follows: an acetonitrile solution of barium-selective probe **1D** was mixed into cyanoacrylate in 1:1 ratio to desired concentration (10 × 10^{-12} to 10 × 10^{-6} M). A total of 30 μL of this solution was applied to a glass microscope slide and then dried in an oven for 5 min at 373 K to set it into a thick solid layer. Fluorescence response from three slides was measured with excitation at 430 nm before and after washing with 50 μL of 1 × 10^{-3} M metal perchlorate in acetonitrile or only acetonitrile and then drying. Each slide was then rescanned three times, and the fluorescence response was averaged to yield a mean response.

3.2.4. Microscopy Details

Probe **1D** was suspended at a concentration of 10^{-11} M within the cyanoacrylate matrix and analyzed via fluorescence microscopy. Excitation is delivered with a supercontinuum laser with the output selected using an acousto-optical tunable filter. For the studies performed here, several output lines were superposed between 420 and 437.5 nm, to maximize output power and cover the excitation band of 1D. Laser light was cleaned by passing through a beam expander and cutting off the outer, nonuniform edge with an iris, generating a circular and approximately Gaussian beam profile. The beam was then redirected through a 500 nm short-pass filter to reduce incident background light, reflected off a 505 nm dichroic mirror, and focused through a 100X air-coupled microscope objective (NA = 0.95) for a final power output of 125 mW to excite the **1D** matrix in the epifluorescent mode. The objective collected resultant Stoke's shifted fluorescent emissions, which were then passed back through the dichroic mirror and a 500 nm long-pass filter, again for background reduction, and collected via a Hamamatsu EMCCD camera, which acquired one image every half second into 300-image sequences. Microscopy images were processed using an algorithm that first filters the image in Fourier space to remove slowly sloping backgrounds and then sums the sequence over the full imaging time. After filtering, single-molecule candidates can be identified after subtracting the background profile, which is found by blurring the summed image via a Gaussian filter. Single-molecule candidates are identified as points with intensities in the excess of 3σ above the background. Once the candidates are identified, their locations on the raw images are analyzed as a function of time for the duration of the sequence to produce fluorescent trajectories. These trajectories are scanned for an instantaneous drop or "single-step" profile, which is the hallmark characteristic of a single molecule undergoing a discrete photobleaching process.

3.2.5. Computation Details

Molecular structures were optimized using the M06-2X[106] functional with the SDD[107-110] effective core potential basis set for heavy metal atoms (barium and mercury) and def2- SVP[111,112] basis set for other atoms, followed by frequency analysis to confirm the nature of their energy minima (no imaginary frequency). Calculations with time-dependent density functional theory (TDDFT)[113] were carried out to reveal the orbitals involved in the observed fluorescence events. SMD[114] or PCM[115] solvation models were used to incorporate solvent effects with acetonitrile as the solvent. All calculations were performed using the Gaussian 09 program.[116]

3.3. Results and discussion

3.3.1. Synthesis

Scheme 3 represents the synthesis of probes **1A−1E**. In brief, nucleophilic aromatic substitution of 4-fluoronitrobenzene by mono/diaza crown ethers, prepared by modification of our previous work,[99] gave the desired 4-nitroaniline derivatives **3A−3D**. Reducing 4-fluoronitrobenzene to one equivalent was critical in the case of diaza-18-crown-6 ether **2D**. Nitro reduction by Pd-catalyzed hydrogenolysis followed by condensation with commercially available 4-bromonaphthalic anhydride resulted in the desired bromonaphthalimide products **4A−4D**. Initial attempts for the final nucleophilic aromatic substitution reaction of bromonaphthalimide with n-butylamine in 2-methoxyethanol led to poor yields of the desired aminonaphthalimides. However, switching the solvent to N-methyl-2-pyrrolidone, a basic solvent, enabled the bromide substitution to afford the desired aminonaphthalimides **1A−1D**. Compound **1E** was prepared by nucleophilic substitution by dropwise addition of benzyl bromide into a solution containing **1D** and potassium carbonate. Overall, this synthetic approach led to the efficient preparation of the desired naphthalimide fluorescent probes **1A−1E**.

3.3.2. UV−Vis Studies

UV−vis spectra of all synthesized 1,8-naphthalimide-based fluorescent probes (**1A−1E**) were recorded in an acetonitrile solvent at room temperature. Major absorbances were centered between 200−300 and 380−480 nm consistent with 4-amino-1,8-naphthalimide chromophores.[76] Solutions doped with Ba^{2+} provided no or negligible shifts on UV−vis absorbances in all probes (**Figure 3.5.1**). These effects were also encountered in acetone and ethanol (**Figure 3.5.2**). In dichloromethane, however, a slight red shift was observed possibly because of change in solvent polarity as a result of addition of barium ions in the acetonitrile solvent. $Ba(ClO_4)_2$ addition led to a concentration-dependent increase in fluorescence centered near 530 nm in probes **1B**, **1D**, and **1E**, when excited at λ_{max} obtained from the UV−vis spectrum, suggesting turn-on fluorescence by changes to PET.[82] Similarly, fluorescence analysis as a function of absorption wavelength from 430 to 460 nm showed no significant change in the emission intensity profile (**Figure 3.5.3**).

3.3.3. Fluorescence Response and Metal Ion Selectivity

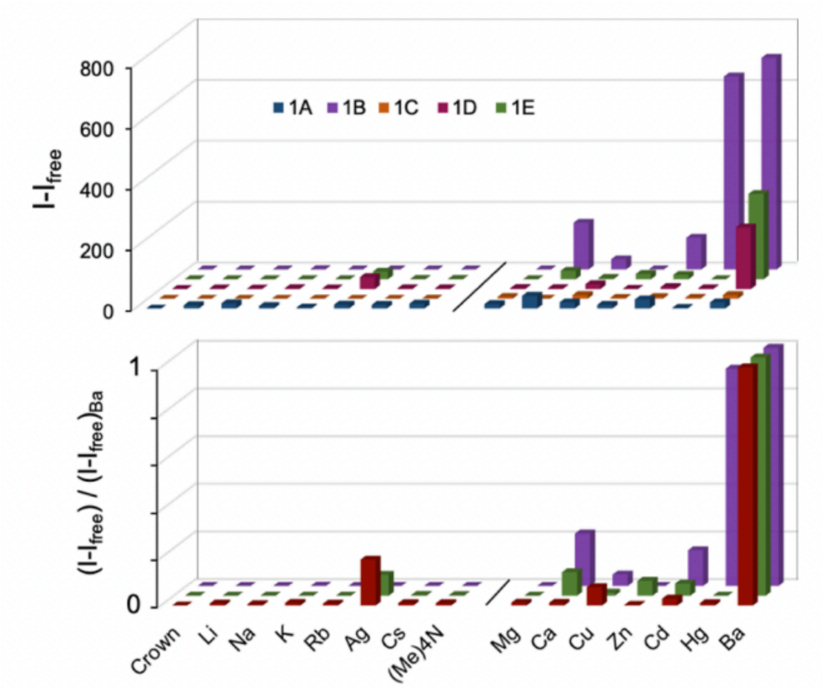

Figure 3.1. Top: ion perchlorate (5×10^{-6} M) response to **1A−1E** (1×10^{-6} M) in MeCN solution. Bottom: fluorescence response of **1B**, **1D**, and **1E** with different cation solutions normalized to fluorescence intensity for barium perchlorate.

Fluorescent response to cationic analytes was determined for each of the synthesized probes (1.0 μM in acetonitrile). Stock solutions of perchlorate salts were prepared in a 9:1 mixture of MeCN/H_2O to achieve complete dissolution. The final concentration of the perchlorate solution was maintained at 5 μM to achieve 1:5 concentration ratio of the probe to the ion analyte. The selectivity studies are summarized in **Figure 3.1**, top panel with emission at 530 nm. **Figure 3.5.10** demonstrates I/I_0 analysis of the same data. Molecular probes **1A** and **1C** were not effective optical sensors for almost all tested ions. A small twofold response was found in the case of calcium with probe **1A**. In contrast, **1B** showed excellent sensitivity toward Ba^{2+} and Hg^{2+} in addition to a lesser response to Ca^{2+}. In the presence of Ba^{2+} and Hg^{2+} solutions, ca. 30-fold increases in fluorescence intensities were observed. Ca^{2+} and Cd^{2+} ions also showed eightfold and fivefold increases, respectively, for probe **1B**.

Two novel 4-amino-1,8-naphthalimide derivatives containing diazacrown ether-binding domains **1D** and **1E** were found to have excellent selectivity to Ba^{2+}. **1D** and **1E** showed solution-phase emission enhancements of 11-fold and 22-fold, respectively, in the presence of Ba^{2+}. Among the different ions (Mg^{2+}, Ca^{2+}, Cu^{2+}, Zn^{2+}, Cd^{2+}, Hg^{2+}, Ba^{2+}, Li^+, Na^+, K^+, Rb^+, Ag^+, Cs^+, and $(CH_3)_4N^+$) studied, only Ba^{2+} showed significant increased fluorescence for probes **1D** and **1E**. Other ions showed little to no (<2×) fluorescence intensity. Normalized fluorescence responses highlight selectivity by ignoring differences in absolute brightness and show **1D** and **1E** with highest selectivity for Ba^{2+} (**Figure 3.1**, bottom panel).

Barium sensitivity remained in all but one competitive fluorescence experiment (**Figure 3.2**). The barium selectivity of probe **1D** is observed in all cases, except for open-shell Cu^{2+}. Cu^{2+} addition showed a blue-shifted absorption spectrum reminiscent of the aminoless 4-H-naphthalimide chromophores (**Figure 3.5.11**). This phenomenon is potentially due to Cu^{2+}'s strong binding to the 4-amino-residue, truncating the cross-conjugation of the sensor chromophore of **1D**. However, Cu^{2+} and other open-shell transition metals often interact with PET fluorophores to quench fluorescence by an electron/energy transfer mechanism.[117,118] This effect was observed in another "turn-off" Cu^{2+} 4-amino-1,8-naphthalimide sensor.[119] We compared the fluorescence of Cu^{2+} and Ba^{2+} addition to the sensor **1D** and to a binding domain-free 4-amino-1,8-naphthalimide analog (**Fluo**, **Figure 3.5.12**). Cu^{2+} effects were identical with and without the crown ether moiety. DFT computational studies have limitations for such open-shell systems,[120] but our studies were consistent with these Cu^{2+} experimental results, showing an open-shell nonfluorescent **1D** molecule and interactions with the 4-amino residue in our model fluorophore (Fluo, **Figure 3.5.13**). Despite the interesting copper inactivation, these data are evidence of increased sensor selectivity of two novel turn-on optical sensors **1D** and **1E** to Ba^{2+}.

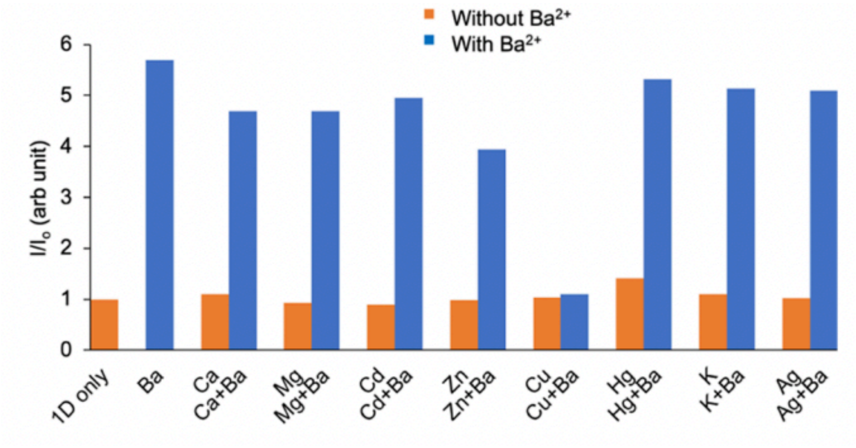

Figure 3.2. Fluorescence response of **1D** (2×10^{-6} M) to Ba^{2+} (5×10^{-6} M) in the presence of other metal ions (ions, 5×10^{-6} M) in acetonitrile. Slit width 2.5/5.0.

3.3.4. Fluorescence Titration and Binding Studies

Fluorescence titration curves presented in **Figures 3.3A, 3.5.4A**, and **3.5.5A** show that the emission reaches maxima near one equivalent of Ba^{2+} addition for probes **1E, 1B**, and **1D**, respectively. Titration studies performed with probes **1B, 1D**, and **1E** with an increasing concentration of barium perchlorate in acetonitrile gave dissociation constant reveal effective binding between each probe and Ba^{2+}. Solution-phase limits of detection (LOD) were calculated using linear fitting curves of fluorescence titration data and the formula LOD = 3σ/k, where σ is the standard deviation of the blank sample without barium and k is the slope between intensity versus barium concentration,[121] resulting in 0.0288×10^{-6}, 0.074×10^{-6}, and 0.006×10^{-6} M detection limits for probes **1E, 1B**, and **1D**, respectively. **Figures 3.3B**, **3.5.4B**, and **3.5.5B** show good linear correlation for probes 1**E** ($R^2 = 99.5$), 1B ($R^2 = 98.5$), and 1D ($R^2 = 99.1$). Overall results show that the probes **1B, 1D**, and **1E** can detect Ba^{2+} in solution at nanomolar concentrations and therefore can be highly practical fluorescent sensors for selective detection of Ba^{2+}. The stoichiometry of binding for molecular probes **1B** and **1E** with barium was calculated by Job's method. The results, presented in **Figures 3.5.4C** and **3.3C**, show the inflection point of two linear fitting curves at 0.46 and 0.50 mol fraction for complex **1B**−Ba^{2+} and **1E**−Ba^{2+}, respectively. This indicates a 1:1 binding stoichiometry between probes **1B** and **1E** with Ba^{2+}. Additionally, complex **1B**−Ba^{2+} was observable in a high-resolution mass spectrometric analysis of the solution of **1B** and barium perchlorate (**Figure 3.5.4D**).

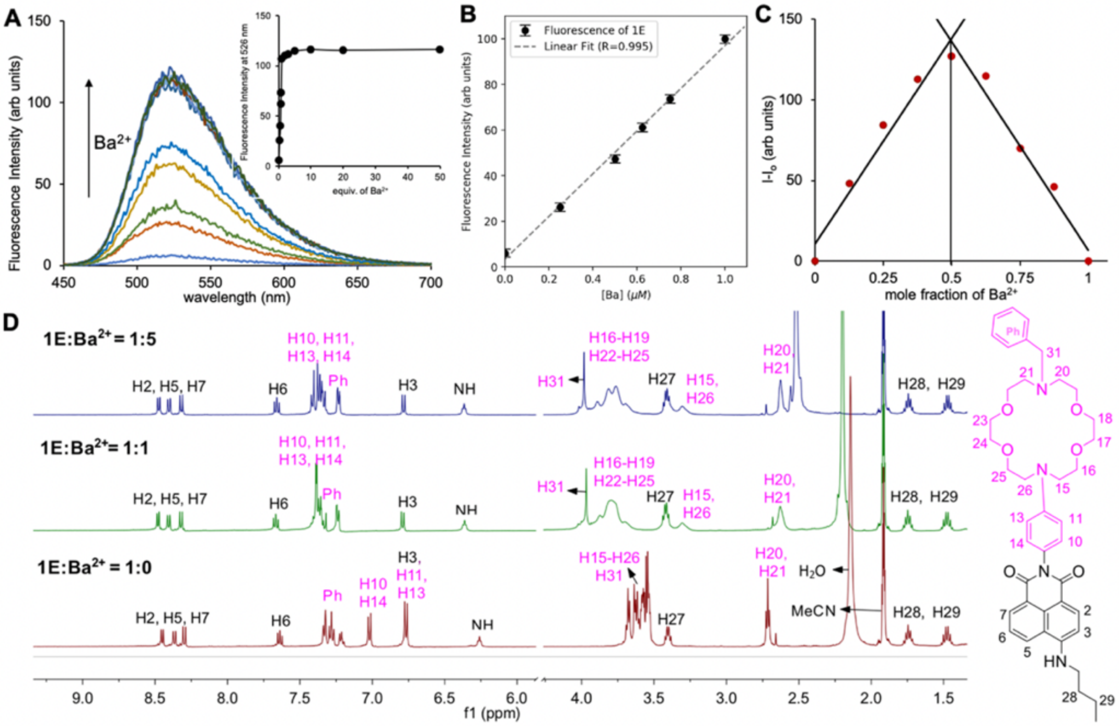

Figure 3.3. (**A**) Fluorescence titration spectra of **1E** (1×10^{-6} M) upon addition of Ba^{2+} (0 to 50×10^{-6} M) in acetonitrile (λ_{ex} = 430 nm). (**B**) Linearity of fluorescence intensity at 526 nm for **1E** (1×10^{-6} M) in acetonitrile as a function of the concentration of Ba^{2+}. (**C**) Job's plot figure for **1E**−Ba^{2+} at constant total concentration 20×10^{-6} M of **1E** and barium in acetonitrile. (**D**) ^1H NMR titration spectra of probe **1E** with the addition of 0.0 (red trace), 1.0 (green trace), and 5.0 (blue trace) equiv. of Ba^{2+} in acetonitrile-d_3. The inset shows the plot of fluorescence change as a function of Ba^{2+} concentration. Slit width 2.5/5.0 presence of other metal ions (ions, 5×10^{-6} M) in acetonitrile. Slit width 2.5/5.0.

3.3.5. ^1H NMR Studies

Complexation between Ba^{2+} and fluorescent probes **1B, 1D**, and **1E** was further demonstrated by ^1H NMR experiments performed with 1:1 and 1:5 M ratios of the probe and $Ba(ClO_4)_2$ in acetonitrile-d3. Ba^{2+} addition resulted in downfield shifts of N-phenyl-aza crown ether protons, while the chemical shift values of protons in the naphthalimide fluorophore group have minimal or no change (**Figure 3.3D**).

Noticeably, an upfield shift in α-protons of the anilino nitrogen in azacrown ether was also observed (H15 and H26 in **Figure 3.3D**) in all molecular probes (for **1B** and **1D**, see **Figure 3.5.6**), suggesting that the nitrogen atom of N-phenyl-aza crown ether was not directly involved in ion binding. Similarly, the effect of Ba^{2+} on the N-benzyl group in probe **1E** was observed, as seen with downfield shifts of both aromatic and benzylic protons (**Figure 3.3D**). Additionally, in fluorescent probes **1D** and **1E**, all α-protons of two nitrogen atoms in the diazacrown ether structure showed an upfield shift, indicating no interaction between both the nitrogen atom of diazacrown and Ba^{2+}. The results obtained from ^1H NMR experiments with probes clearly show the binding of Ba^{2+} on the receptor crown ether units with no significant binding on naphthalimide fluorophore units. Comparative ^1H NMR studies were carried out with Ba^{2+}, Hg^{2+}, and K^+ in the case of probe **1B**, which showed distinct features in the NMR spectra. With Hg^{2+} addition, all monoazacrown methylene protons were deshielded, indicating binding of the nitrogen atom of Nphenyl-aza crown ether with Hg^{2+} (**Figure 3.5.8**). With K^+, however, no observable change was found in the chemical shift values of the protons of both naphthalimide and azacrown ether moieties (**Figure 3.5.9**).

3.3.6. Computational Studies

Computational models were studied using TDDFT to predict the fluorescence behavior of sensors in response to ions as calculated within an acetonitrile solvent model (**Figure 3.4A−D**). As a test suite, we considered molecules **1B** and **1E**, both unchelated and chelated with Ba^{2+}, K^+, and Hg^{2+}. The results support the proposed PET-mediated off-state within unchelated mono- and diazacrown ether naphthalimides, which is turned on by chelation-enhanced fluorescence (CHEF) upon ion binding. In the unbound 1B species (**Figure 3.4A**), excitation of the naphthalimide fluorophore is governed by a HOMO−1 to LUMO transition based on orbital analysis. The electrons in the interstitial $HOMO_{free}$ orbital of the receptor (highlighted) are localized around the N-aryl unit and energetically well positioned to quench the excited state before fluorescence transition can occur from the LUMO to HOMO−1, by a traditional PET mechanism. Upon barium chelation, however, the $HOMO_{free}$ level is drastically stabilized by mixing with Ba^{2+} and becomes the new HOMO−1 (**Figure 3.4B**), allowing the fluorophore-centered HOMO and LUMO levels of the barium-bound species to participate in fluorescence without PET quenching.

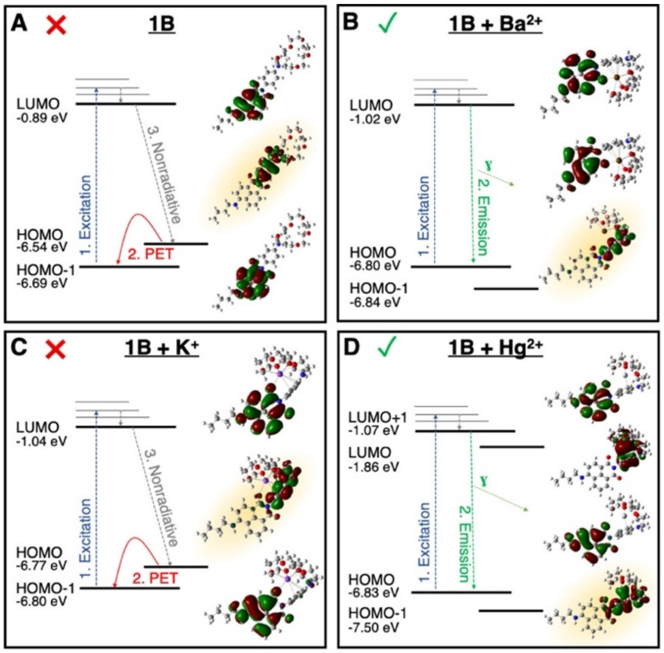

Figure 3.4. Simulated orbitals of **1B**. The mechanism of PET and CHEF is illustrated by the change in energy of the nitrogen-dominated orbital, highlighted, upon binding various cations.

As **1B** responds to Hg^{2+} but not to K^{+}, we examined the arrangement of frontier molecular orbitals when complexed to these cations. Chelation is effective and lowers the critical PET-enabling $\text{HOMO}_{\text{free}}$ orbital through binding to both ions. However, in the case of K^{+}, PET quenching is still possible (**Figure 3.4 C**), predicting a non-fluorescence response to K^{+} consistent with the experiment. Hg^{2+} chelation results in notable lowering of the HOMO, LUMO, and LUMO+1 energy states relative to the free chemosensor (**Figure 3.4D**); the LUMO and LUMO+1 states show substantial lowering in energy including a reordering of states, not unusual among heavy-atom binding.[122] Excitation of the fluorophore-centered electrons (HOMO to LUMO+1) is not quenched by PET. Thus, CHEF occurs with Hg^{2+} addition to **1B**, similar to the barium chelation, albeit with a different rearrangement of orbital energies.

Analysis of the selective diazacrown ether chemosensor **1E** showed similarity to **1B** when free and bound to Ba^{2+} and K^{+}, especially with respect to the critical relative location of the $\text{HOMO}_{\text{free}}$ orbital (highlighted in **Figure 3.5**). However, Hg^{2+} binding resulted in a weaker effect on the $\text{HOMO}_{\text{free}}$ orbital, and the fluorescence of Hg^{2+}-bound species is still quenched by internal PET from the HOMO to HOMO−1. Overall, the theoretical studies support experimental results for the enhanced selectivity of **1E** to Ba^{2+}.

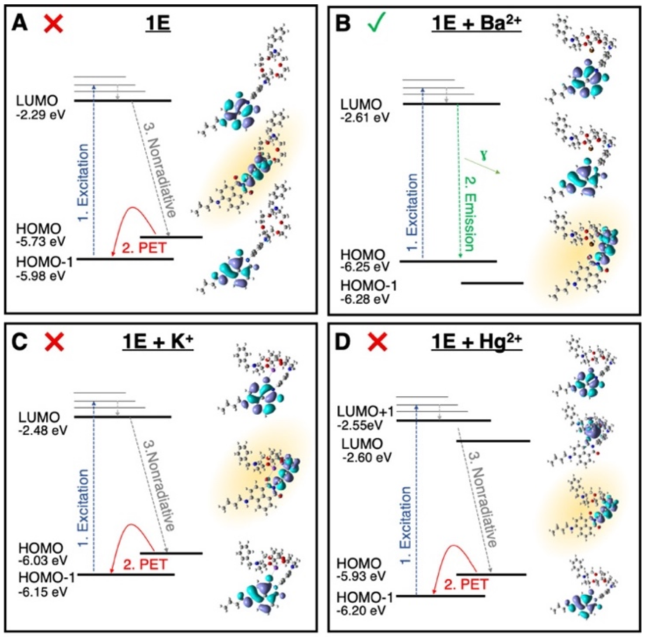

Figure 3.5. Simulated orbitals of **1E**. Enhanced Ba^{2+} selectivity is illustrated by comparing changes in energy of the nitrogen-dominated orbital, highlighted.

In conclusion, the theoretical models correctly predict the observed switch-on fluorescence patterns across all ions and species tested. These are summarized in **Table 1**.

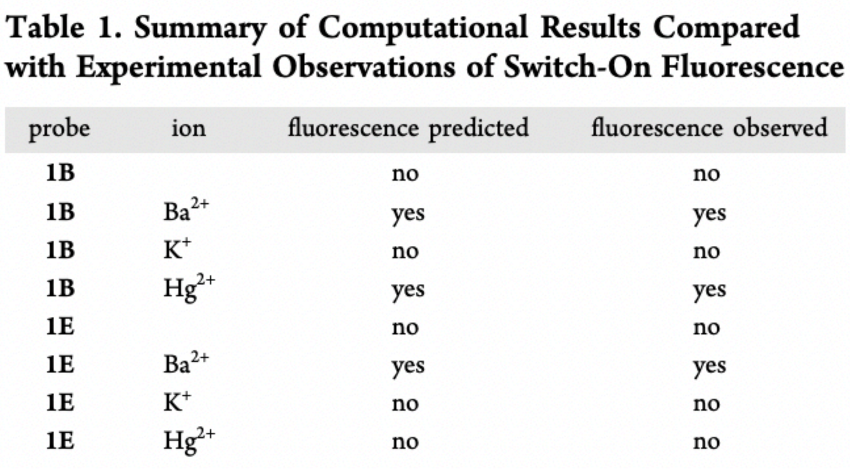

Table 1. Summary of Computational Results Compared with Experimental Observations of Switch-On Fluorescence

probe	ion	fluorescence predicted	fluorescence observed
1B		no	no
1B	Ba^{2+}	yes	yes
1B	K^{+}	no	no
1B	Hg^{2+}	yes	yes
1E		no	no
1E	Ba^{2+}	yes	yes
1E	K^{+}	no	no
1E	Hg^{2+}	no	no

3.3.7. Dry SMFI of Ba^{2+}

To demonstrate single-ion sensing in a dry environment, compound **1D** was suspended in a cyanoacrylate polymer. Polyvinyl acetate and polystyrene matrices were initially investigated with interesting yet relatively poor solvatochromic effects on bulk fluorescence. Barium-induced fluorescence was first verified by spectrophotometry in a bulk matrix. A strong fluorescent response was observed across all three tested locations on three slides, although significant variability was observed because of the imperfect uniformity of layer deposition. **Figure 3.6A** shows the background-subtracted response of slides with no added Ba^{2+} and after Ba^{2+} wash. Fluorescence is normalized to activity on the rising edge of the excitation peak before background subtraction. Mean and standard deviation are shown as dashed and filled regions, in addition to individual response curves. Also, the shown overlaid is a control measurement using a pure solvent wash, resulting in slightly reduced fluorescence, likely because of removal of some ionic contamination or fluorescent emitters from the surface. Furthermore, the selectivity toward barium is maintained in the dry phase because this fluorescent response was not observed in the case of potassium and mercury (**Figure 3.5.7**). These data demonstrate that fluorescent response to Ba^{2+} is maintained in the dry phase, as observed in our past work with molecules of this family,[99] however, now with selectivity for barium ions and the potential for enhanced SMFI. The imaging modality for SMFI in this paper is air-coupled epifluorescent microscopy. This too is distinct from our prior work[70] on SMFI imaging of Ba^{2+} in solution, which used total internal reflection fluorescence (TIRF). TIRF offers combined benefits of a reduced background by exciting only at the glass−sample interface and oil couplings that allow for high numerical aperture imaging. The oil required for through-objective TIRF, however, is likely problematic within the high purity xenon environment of our target application. Because the oil-free imaging modality used here introduces additional practical challenges, realization of single-Ba^{2+} imaging in this way encapsulates an important practical step toward application in time projection chambers.

A set of slides was prepared for single-ion level imaging of barium, with compound **1D** suspended at 10 pM concentration in the cyanoacrylate matrix. Slides were washed with a 1 nM Ba^{2+} solution. A stark increase in the net fluorescence intensity of the sample was observed upon the addition of Ba^{2+}. Three slides were tested, with image sequences taken across three locations both before and after the barium solution was introduced. The increase in intensity was quantified via a raw pixel histogram for each slide, as shown in **Figure 3.6B**. A robust increase in bright pixels was observed in all cases, indicative of turn-on fluorescence.

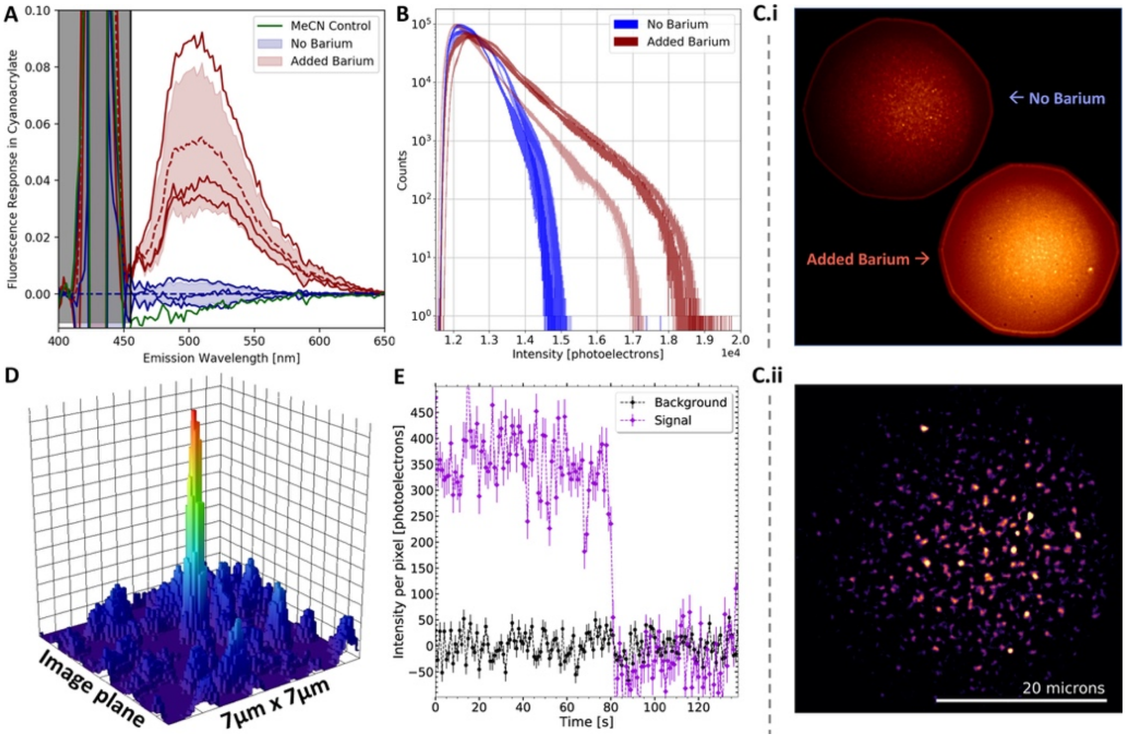

Figure 3.6. Solid-matrix measurements of barium-sensing fluorophore **1D**. (A) Bulk spectrophotometry in a dried cyanoacrylate matrix; (B) raw pixel histogram of three **1D**-coated slides imaged at the single-molecule level; (C) single-molecule level microscopy images of the **1D** layer with and without Ba^{2+} (i) and with Ba^{2+} after background removal (ii); (D) specific single reconstructed barium-chelated **1D** molecule; and (E) bariumchelated **1D** molecule fluorescence time trajectory showing a single-step photobleaching characteristic of SMFI detection.

The detected fluorescence in these images originates from molecules at various distances from the focal plane, with near focus points appearing very bright and out-of-plane candidates appearing dimmer. Both before and after addition of Ba^{2+}, an array of spots of various degrees of brightness can be observed, undergoing discrete photobleaching transitions over time, with the number dramatically enhanced in the barium-added images. An example of a before/after comparison is shown in **Figure 3.6C**(i), where in both cases, bright points corresponding to distinct barium−**1D** complexes can be visually identified.

Using a sample with 10 pM barium perchlorate solution applied to the 10 pM sensor matrix, the interpretation of these bright emitters as single molecules was confirmed. **Figure 3.6C**(ii) shows an example image processed and filtered according to the algorithm described in the Microscopy Details section, which is used as an input to time series analysis. The well-localized candidate spots in this image, an example of which is shown isolated in **Figure 3.6D**, are observed to exhibit discrete photobleaching transitions, as shown in **Figure 3.6E**. This behavior, also observed visually for the bright spots in the denser samples, as well in previous work in the solution phase,[70] confirms the single-molecule interpretation of these fluorescent emitters.

3.3.8. Toward Gas-Phase Ion Sensing

An aspect that remains undemonstrated here is the capture of Ba^{2+} within an environment of high-pressure xenon gas. Our past theoretical work[123] demonstrated that solvation-like effects with xenon are expected, with the shell configuration depending on gas temperature and pressure. The xenon shell typically contains 7−10 xenon atoms for Ba^{2+} at 10−15 bar. Capture by a molecular layer must free Ba^{2+} from this shell of accompanying spectator atoms, typically held at a binding energy of 3−4 eV. The Ba^{2+} binding energy of the molecules developed in this work is calculated to be around 0.2 eV in MeCN. However, calculations of the binding affinity in the gas phase, removing polarization effects of the solvent, show a much-enhanced binding energy of −10.5 eV. This is sufficient to extract the target Ba^{2+} from its weakly attached xenon neighbors, so efficient capture of Ba^{2+} from high-pressure xenon gas is expected. Notably, the xenon solvation shell may also offer useful protection until proximity adequate for capture occurs.

A pertinent question for the design of a molecular sensing layer at the gas−solid interface is the optimal surface density of probe molecules. An ultra-dense fluorophore layer is likely to suffer from collective quenching effects, whereas an overly sparse one may not efficiently capture arriving ions. To this end, we undertook computations of the range of ion capture. Complexation can be considered to be inevitable when the ion−molecule proximity is such that the binding energy is more than a few times the thermal energy ($kT \sim 0.02$ eV at STP). To evaluate the effective capture range, the most stable geometry of the complex **1B**−Ba^{2+} was evaluated as a function of ion-to-surface distance in the gas phase (**Figure 3.7**). Upon allowing Ba^{2+} to move closer to the azacrown ether surface, a bent geometry was obtained where the ion is bound to naphthalimide oxygen along with four ethereal oxygen atoms of the azacrown ether substructure (**structure 4**). This bent geometry of the complex is consistent with the NMR titration study in solution, in which the nitrogen atom of the azacrown ether did not appear to directly bind with the electron withdrawing Ba^{2+} ion. Beyond a range of 32 Å from the anchor point, our simulations fail to converge. The binding energy at this distance is still large, at 1.75 eV. Extrapolating the trend observed in the potential energy surface, it appears that the effective binding range of the molecule is somewhere between 32 and 40 Å. This suggests a range of densities for future monolayer construction, in order to realize efficient binding and reduce intermolecular distortions to fluorescent events. Exploration of the power of sensitive, semi dense monolayers for ion capture at the solid−gas interface is the next immediate step in this ongoing program.

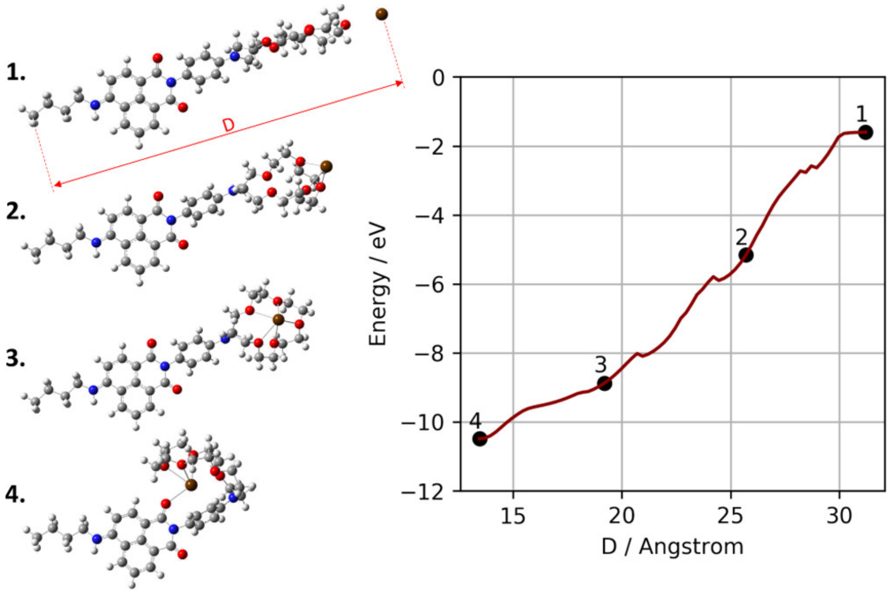

Figure 3.7. Simulation of ionic capture (left) and the potential energy surface in the gas phase as a function of ion-to-surface distance (right).

3.4. Conclusion

We have designed, synthesized, and studied barium-selective fluorescent sensors capable of ion sensing in dry environments, specifically selective Ba^{2+} imaging via SMFI. We found that a new, convenient, and visible-spectrum 4-amino-1,8-naphthalimide derivative with a diaza-18-crown-6 binding domain dramatically improved the selectivity of the sensors to Ba^{2+} without significantly compromising sensitivity. Solution-phase fluorescence and NMR experiments supported a PET mechanism enabling turn-on fluorescence sensing in the presence of metal ions. Experiments showed strong binding of Ba^{2+} to the sensor with 1:1 stoichiometry and a nanomolar LOD. Experimentally validated theoretical calculations illuminated the mechanism of fluorescence sensing, in addition to providing insights into the expected behavior at gas−solid interfaces. SMFI microscopy in the air-coupled epifluorescent mode was employed to sense single Ba^{2+} ions with these fluorophores. Cyanoacrylate was found to be an effective support medium for the aforementioned fluorophores, and because of the sensor's strong selectivity for barium, no competitive binding agent was required to achieve singlemolecule sensitivity with these molecules. Single-Ba^{2+} candidates were resolved spatially and identified through single-step photobleaching transitions, with enhanced prevalence in barium-washed samples. Realization of single-Ba^{2+} sensitivity under these conditions represents an important step toward practical application of this technique within time projection chambers. Such a technique could enable new precision and robustness in searches for 0vββ in xenon gas.

3.5. UV-Vis spectral data of probe 1A-1E in the absence and presence of barium ions

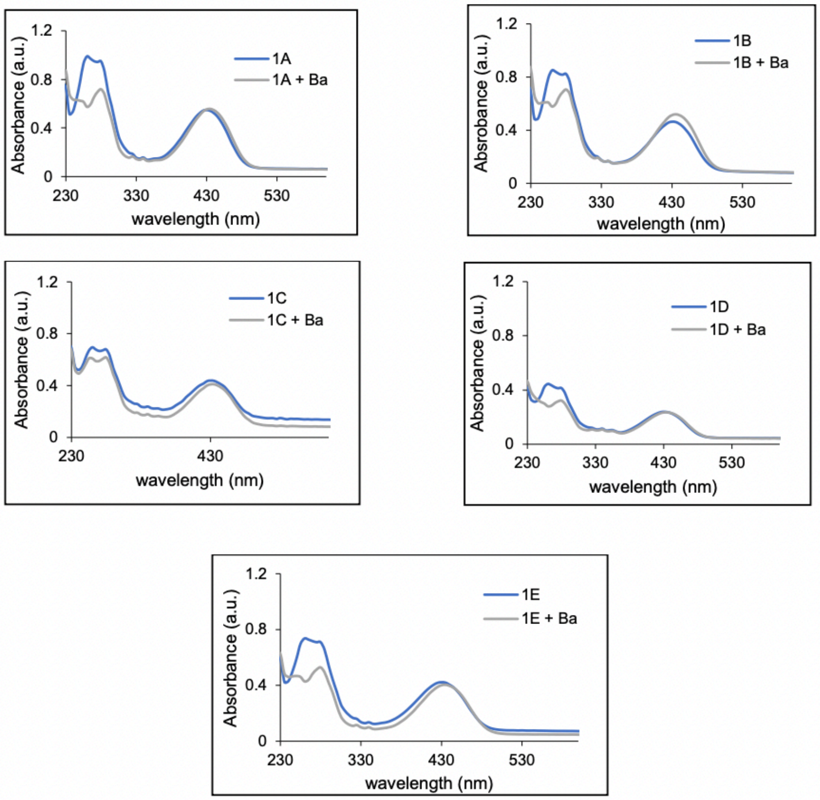

Figure 3.5.1. UV-Vis absorption curves for molecular probes **1A-1E** (10×10^{-6} M) in absence of Barium (blue trace) and in presence of Barium perchlorate (50×10^{-6} M) (gray trace) in acetonitrile.

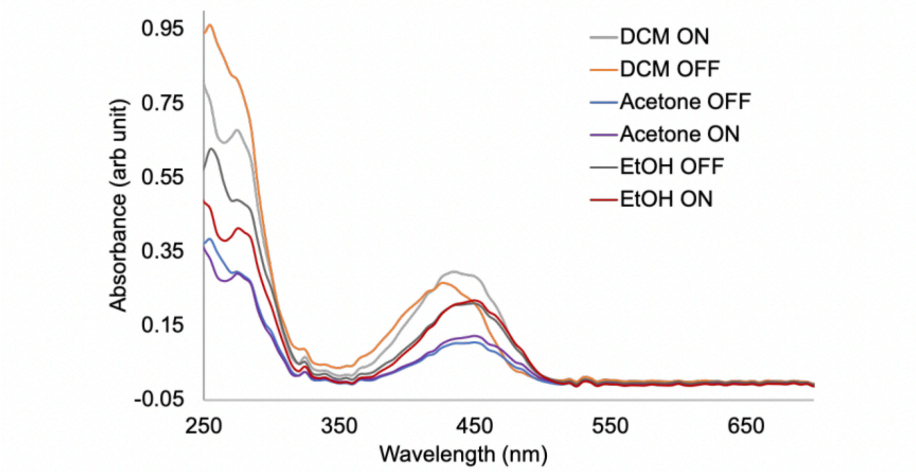

Figure 3.5.2. UV-Vis absorption curves for molecular probes **1B** (10×10^{-6} M) in the absence (OFF sample) and in the presence (ON sample) of barium ions (50×10^{-6} M) (gray trace).

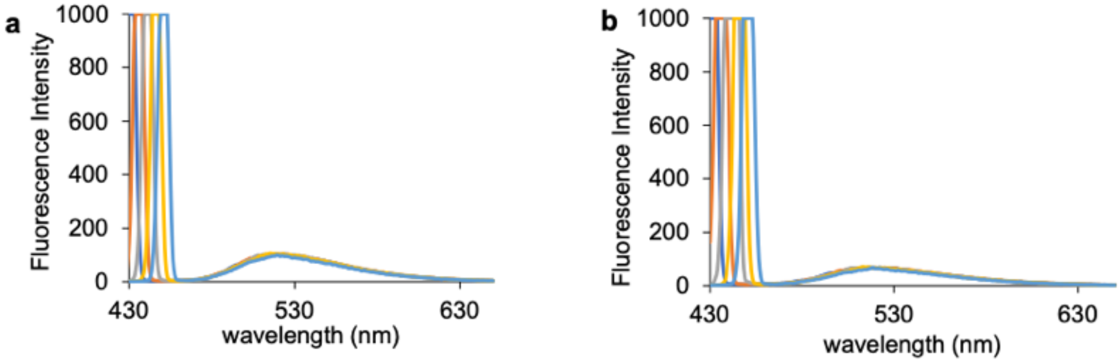

Figure 3.5.3. Fluorescence intensity change for probe **1D** (a) and **1E** (b) as a function of excitation wavelength from 430-460 nm.

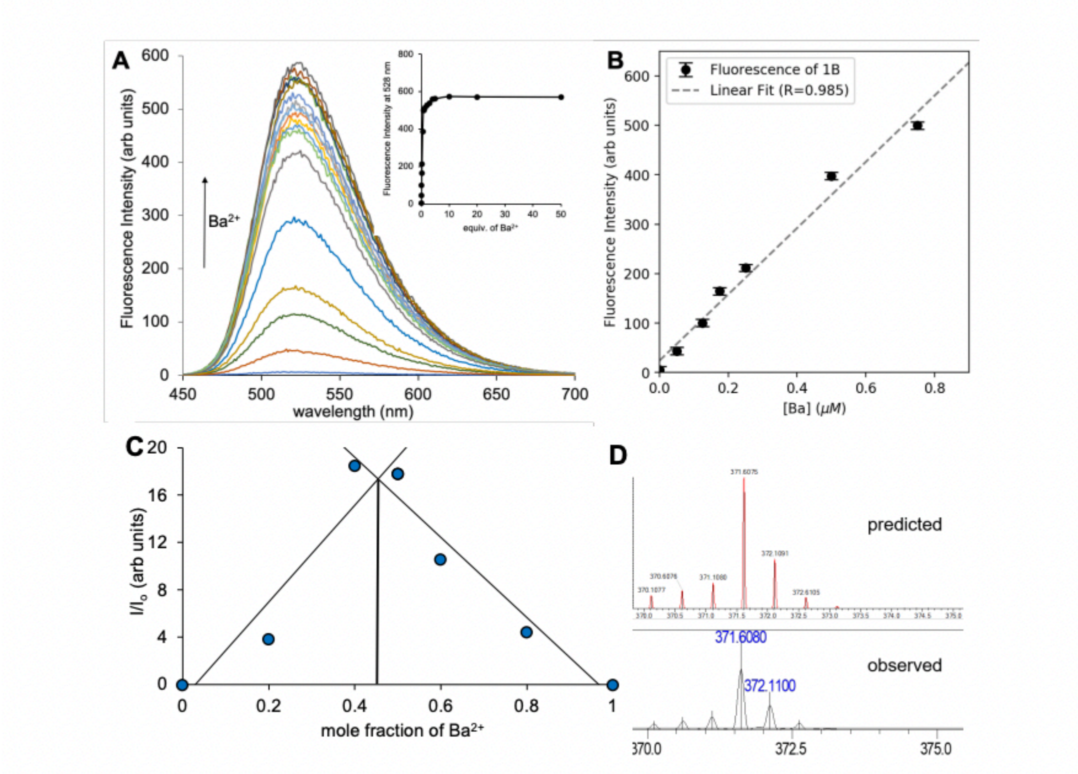

Figure 3.5.4. A: Fluorescence titration spectra of **1B** (1 × 10^{-6} M) upon addition of Ba^{2+} (0–50 × 10^{-6} M) in acetonitrile (λ_{ex} = 430 nm). **B**: Linearity of fluorescence intensity at 528 nm for **1B** (1 × 10^{-6} M) in acetonitrile as a function of the concentration of Ba^{2+}. C: Job's plot figure for **1B** showing the difference between fluorescence intensity before (I_o) and after (I) addition of Ba^{2+} at constant total concentration 20 × 10^{-6} M of **1B** and barium perchlorate in acetonitrile. **D**: Partial HRMS data observed for complex **1B**-Ba^{2+}

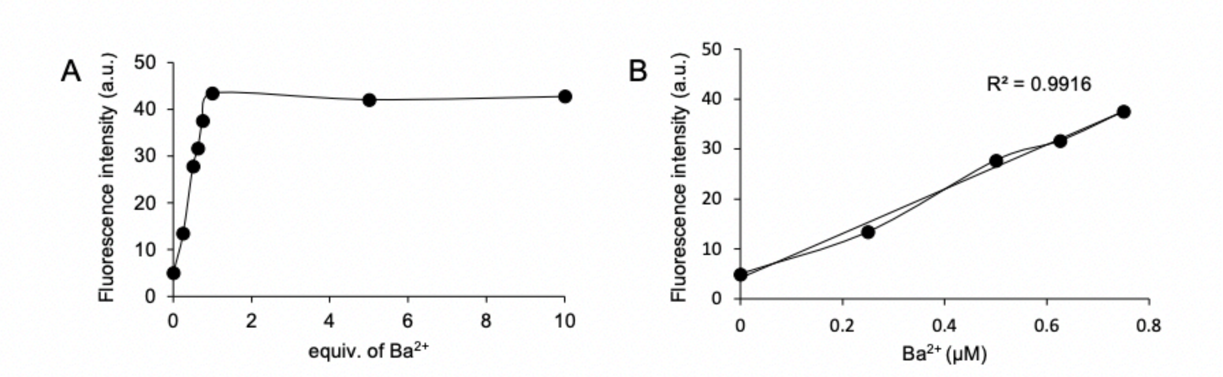

Figure 3.5.5. A: Fluorescence intensity change of probe **1D** (1 μM) as a function of barium perchlorate (0–10 × 10^{-6} M) in acetonitrile. **B**: Linear fitting of fluorescence titration data for probe **1D** (1 μM) as a function of barium concentration in acetonitrile.

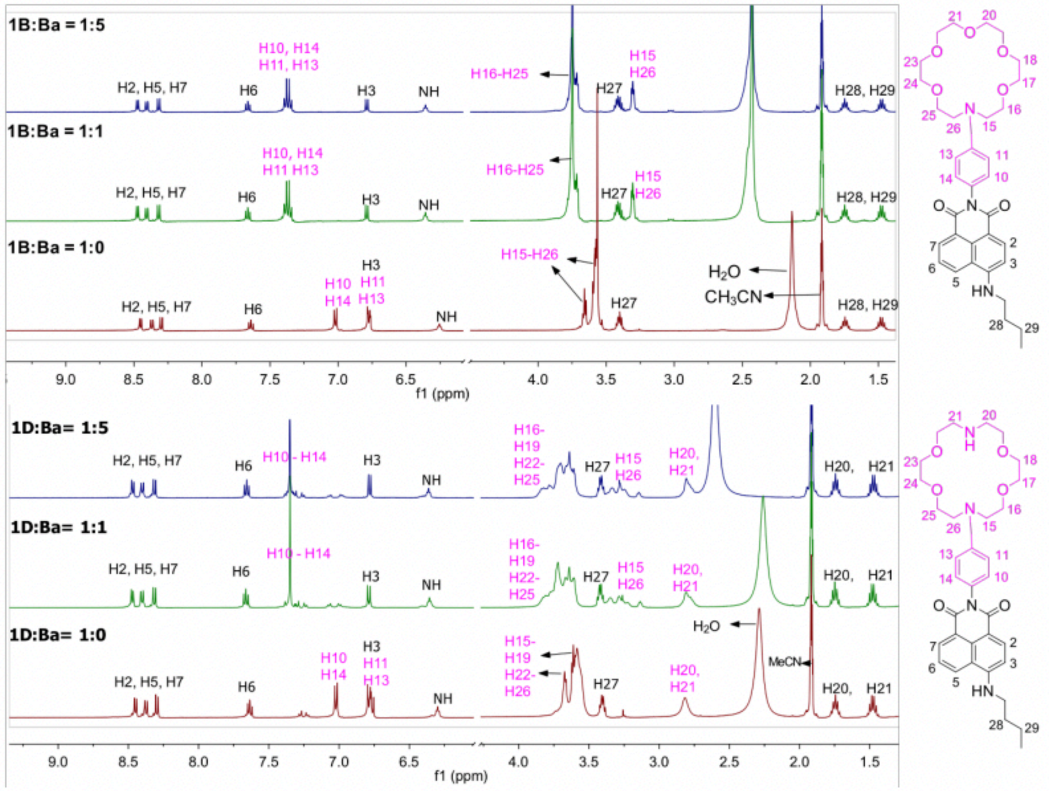

Figure 3.5.6. ^{1}H NMR titration spectra of probe **1B** (top) and **1D** (bottom) with the addition of 0.0 (red trace), 5.0 (green trace) equiv. of Ba^{2+} in acetonitrile-d$_3$. Proton numbering is inconsistent with IUPAC nomenclature.

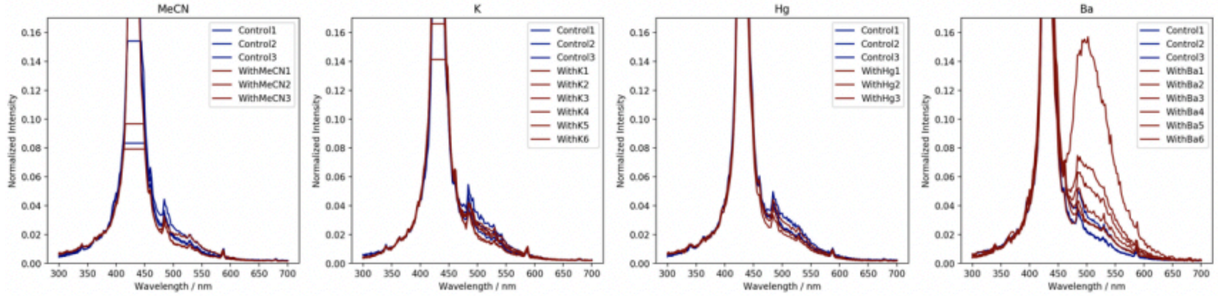

Figure 3.5.7. Bulk dry-phase fluorescent response of probe **1D** in cyanoacrylate polymer matrix with acetonitrile only, potassium perchlorate, mercury perchlorate, and barium perchlorate (excitation wavelength = 430 nm, slit width = 2.5/2.5 nm).

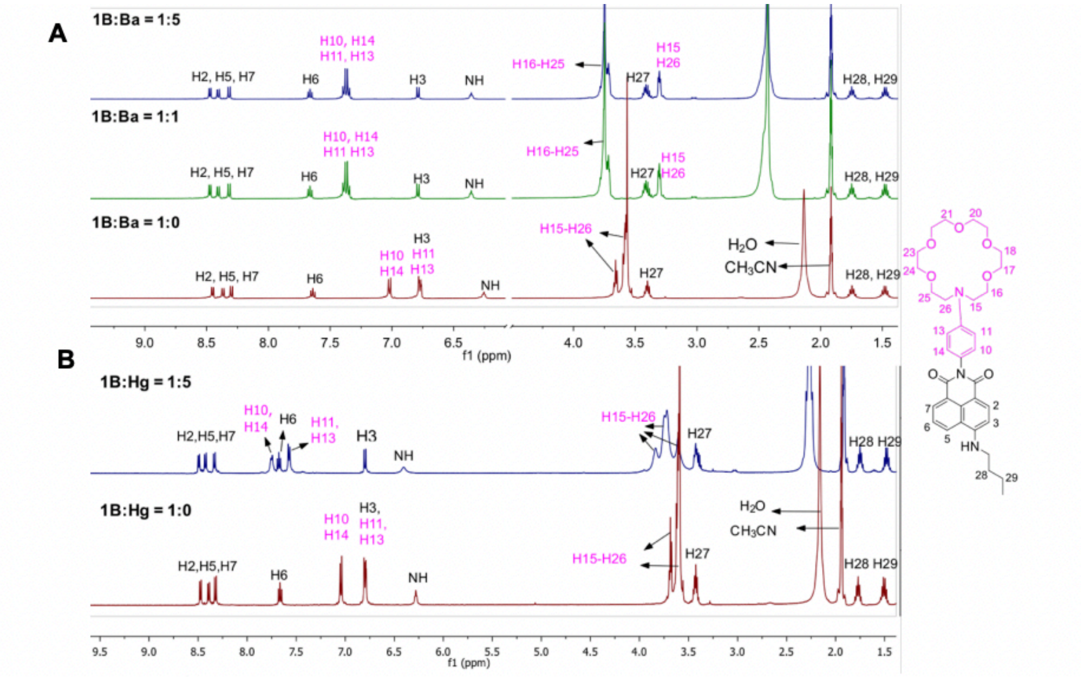

Figure 3.5.8. ^{1}H NMR titration spectra of probe **1B** with the addition of 0.0 (red trace), 5.0 (green trace) equiv. of Ba^{2+} (**A**) and Hg^{2+} (**B**) in acetonitrile-d_3. Proton numbering is inconsistent with IUPAC nomenclature.

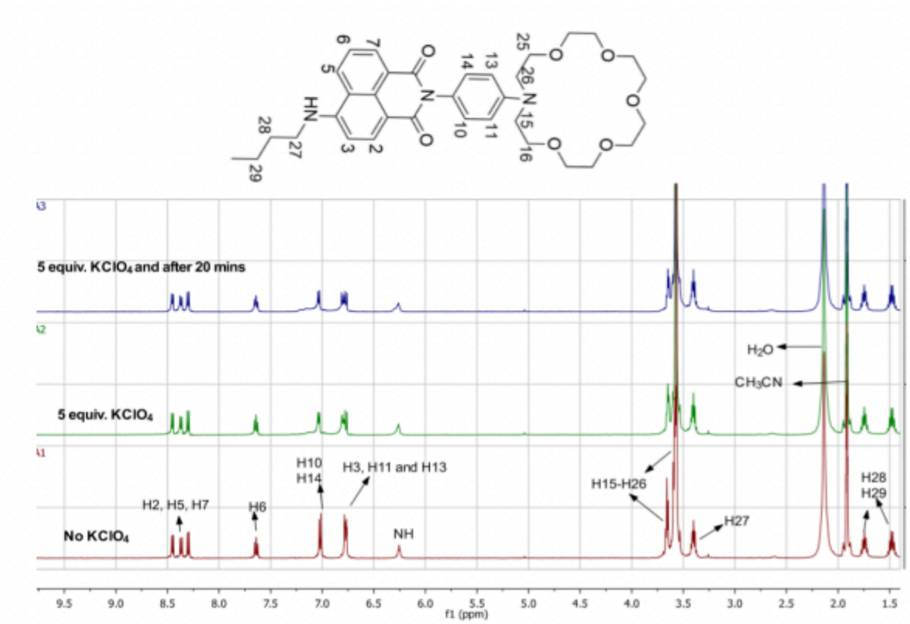

Figure 3.5.9. ^{1}H NMR titration spectra of probe **1B** (top spectrum) with the addition of 0.0 (red trace), 5.0 (green trace), and 5.0 (blue trace) equiv. of $KClO_4$ in acetonitrile-d3. Proton numbering is inconsistent with IUPAC nomenclature.

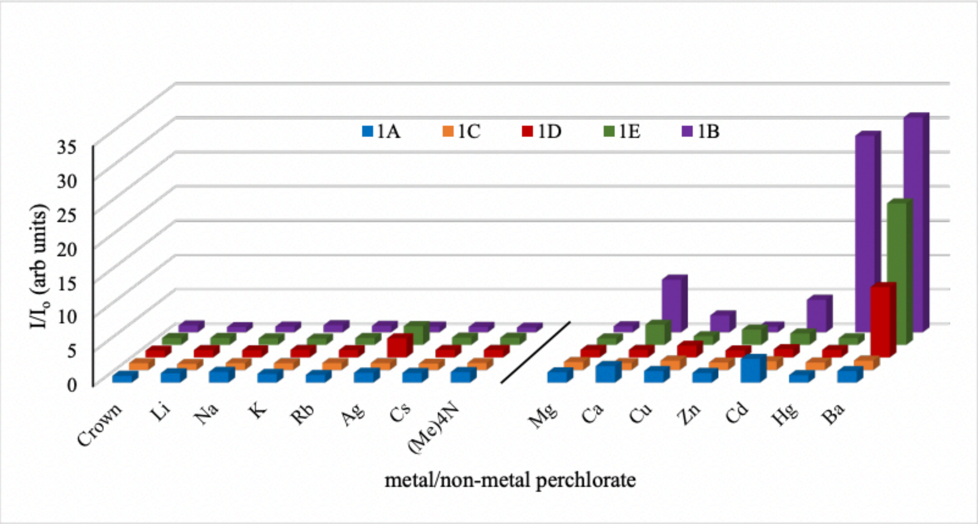

Figure 3.5.10. Ion perchlorate (5×10^{-6} M) response to probes (**1A-1E**) (1×10^{-6} M) in acetonitrile solution.

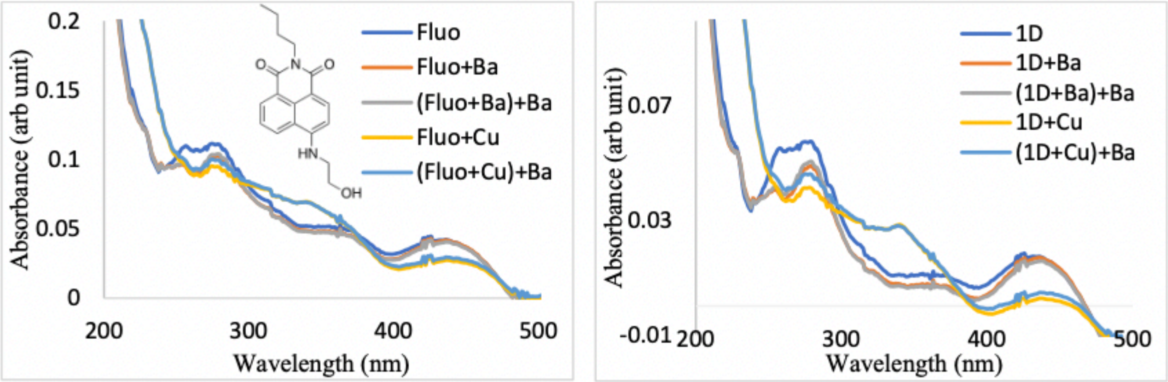

Figure 3.5.11. UV-Vis absorbance of **Fluo** (left) and **1D** (right), each 2×10^{-6} M in acetonitrile with Cu^{2+} and Ba^{2+} (5×10^{-6} M).

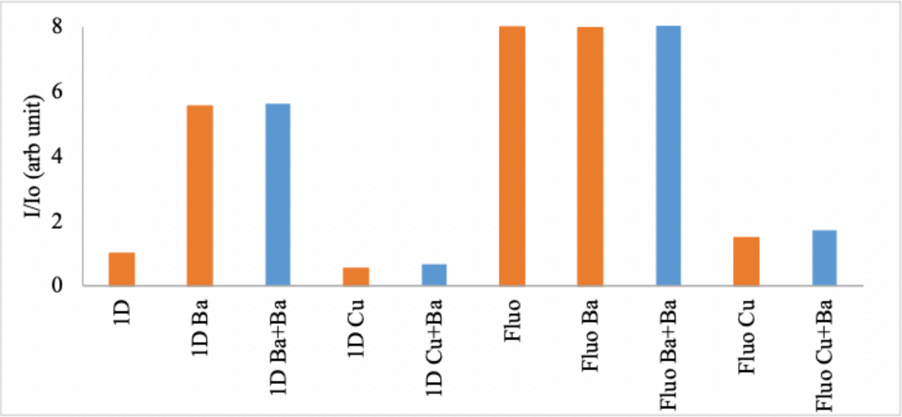

Figure 3.5.12. Fluorescence response comparison of **1D** and **Fluo**, which lacks a crown ether binding domain, (2×10^{-6} M) in the presence of Cu and Ba perchlorate (5×10^{-6} M) in acetonitrile. Slit width 2.5/2.5.

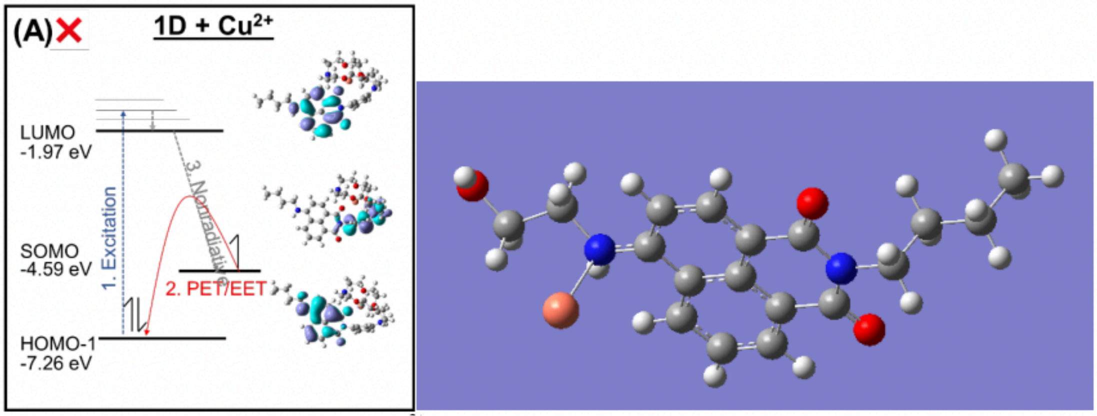

Figure 3.5.13. Simulated (**A**) Orbitals of Cu^{2+} (orange) with **1D** predicting non-fluorescent binding upon interaction with the crown ether domain, and (**B**) geometry of **Fluo** demonstrating interactions with the 4-amino moiety (blue).

Chapter 4.

Design of a Hg^{2+} selective Aminonaphthalimide-aza-crown-ether sensor capable of select fluorescence in cells and within solvent-free matrices.

4.1. Introduction

The measurement of heavy metals in humans, the environment, and industrial processes are critical to the health and sustainability of earth and human systems. Introduced into the atmosphere from natural and anthropomorphic activities, heavy metals persist[124-128] and their bioaccumulation enhances risks to human and environmental health. In particular, mercury has essentially no safe exposure limit, causing significant risks to human health.[129-131] As recognized by the World Health Organization (WHO) as one of the most toxic metals, mercury causes cancers and neurological and genetic disorders. With wide distribution in air, water, and soil, mercury affects the health of most organisms. Mercury's caustic nature is also detrimental to industrial processes like petroleum refining. Its corrosive presence, when undetected, has led to avoidable economic, environmental, and safety hazards. Therefore, a substantial effort has been made to detect CH_3Hg^+ and Hg^{2+} ions in water and cells.[132]

Other heavy metals, such as zinc, are essential metals needed for proper metabolic reactions like gene regulation, apoptosis, etc. However, abnormal levels of zinc in the human body can cause complications related to diabetes, epilepsy, Alzheimer's disease, etc.[133] Therefore, despite their different level of toxicity and environmental and biological impact, mercury and zinc metal/metal ions have been significantly studied using different analytical approaches, which clearly demonstrates the importance of examining the level of these metals and their ions in the environment and organism.

Current analytical techniques for detecting Hg and other heavy metal ions rely on sophisticated instrumentation techniques, including inductively coupled plasma mass spectrometry (ICP-MS), atomic emission spectroscopy (ICP-AES), and atomic absorption spectroscopy. While these methods represent the standard gold insensitivity, they require costly equipment, training, and sample preparation. Fluorescent techniques are comparatively rapid, sensitive, and cost-effective; coupled with advances in optics, fluorescence measurements can be made at low detection levels by routine instrumentation. Though currently requiring more advanced microscopy, fluorescence measurements can image even individual ions through single-molecule fluorescence techniques. Significant efforts, therefore, exist toward mercury fluorescent sensors, and with the advent of turn-on chemosensors that bind individual ions, the potential for enhanced sensitivity and selectivity is growing.[134-145] We have investigated the ability of fluorophores to function at gas/solid interfaces, and use advanced microscopy techniques for sensing and to inform our understanding of structure-function design at such interfaces.[146]

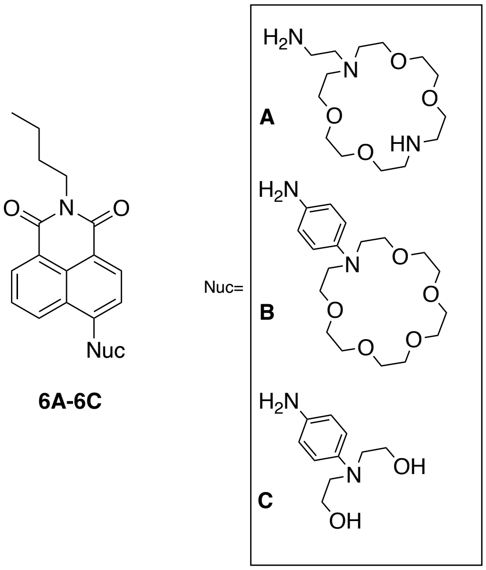

6A-6C

Figure 4. Molecule probes used in this study.

Here we report the design of a Hg^{2+} selective aminonaphthalimide-aza-crown-ether sensor capable of select fluorescence in cells and within solvent-free matrices, which has significant selectivity for Hg^{2+} ions and, therefore, potential as a functional chemosensor for trace mercury in various applications (**Figure 4**). These selective turn-on chemosensors identify Hg^{2+} by an intersystem charge transfer (ICT) mechanism. We recently demonstrated that this class of molecules has promise for their function tailored chemical interfaces between gas and solid optical devices. These sensors are also demonstrated to detect Hg^{2+} in whole cells with limited toxicity.

4.2. Experimental section

4.2.1. Materials

Commercially available chemicals were used without further purification unless specified. Spectrophotometric or HPLC-grade acetonitrile was used. Toluene and hexanes were freshly dried and distilled prior to use. Ultrapure water from a Water Pro BT water station was used for ultrarace analysis.

4.2.2. Equipment

Fluorescence spectra were recorded using a Cary Eclipse Fluorescence Spectrophotometer from Agilent Technologies (Product Number G8800A) at room temperature (25 °C). Instrumental set up: PMT detector voltage-High, Excitation filter-Auto, Emission filter-Open, Excitation slit width-2.5 nm, Emission slit width-5.0 nm, scan control-medium, spectral range 420 nm to 700 nm. All measurements were taken using Buck Scientific type 18 quartz micro cuvettes with 10 mM path length. Stock solutions of probe molecules were prepared at 1×10^{-3} M concentration in acetonitrile. solutions of metal perchlorate salts (Ag^+, Ba^{2+}, Ca^{2+}, Cu^{2+}, Cd^{2+}, Cs^{2+}, Hg^{2+}, K^+, Li^{2+}, $N(CH_3)^+$, Mg^{2+}, Na^+, Pb^{2+}, Rb^{2+}, Sr^{2+}, Zn^{2+}) were prepared at 1×10^{-2} M concentration in 9:1 acetonitrile/water mixture. All fluorescent studies were done by dilution of the probe molecule to 2×10^{-5} M (20 µM). Metal ion selectivity studies were done by diluting metal perchlorate solutions to 1×10^{-4} M (100 µM) concentration.

^1H NMR spectra were recorded on 300 MHz or 500 MHz spectrometers and referenced to the residual solvent signals (7.26 ppm in $CDCl_3$ or 3.33 ppm in CD_3OD). ^{13}C {^1H} NMR spectra were recorded on 75 MHz or 125 MHz spectrometers referenced to the residual solvent signal (77.0 ppm in $CDCl_3$ or 45.0 ppm in CD_3OD). NMR data are reported as follows: chemical shift (δ, ppm), integration (H), multiplicity (s-singlet, d-doublet, t-triplet, q-quartet, m-multiplet, br-broad), coupling constant (*J,* Hz).

High-resolution mass spectrometry (HRMS) data were recorded using a Shimadzu TOF spectrometer in the Shimadzu Center for Advanced Analytical Chemistry at UT Arlington. Fourier transform-infrared (FT-IR) spectra were recorded using a Bruker Alpha-P FT-IR spectrophotometer by attenuated total reflectance on a diamond sample plate.

Thin-layer chromatography was performed on silica gel-coated aluminum plates (EMD Merck F254, 250 µm thickness). Flash chromatography was performed over Silicycle Siliaflash P60 silica gel (mesh 230–

400) or standard grade activated Alumina (mesh 50–300). Melting points were recorded in capillary tubes on a Mel-Temp II apparatus and were uncorrected.

4.3. Results and Discussion

4.3.1. Synthesis

Molecular probes (**Figure 4**) used in this study were synthesized following known protocols, including our own reports on the synthesis of related 1,8-naphthalimide chemosensors.[146] Commercially available 4-bromonapththalic anhydride and butylamine were condensed under reflux conditions. Then nucleophilic aromatic substitution (S_NAr) of the aryl bromide (**5**) with independently constructed amine derivatives led to the completion of synthesis of potential sensors **6B** and **6C**. A similar pathway attained sensor **6A**, however, following S_NAr by ethanolamine, the hydroxyl group was substituted by phosphorus tribromide (PBr_3) in dry toluene, then the alkyl bromide **5B** was substituted with diaza-18-crown-6 ether resulting in the formation of **6A** in a fair yield. The overall scheme represents efficient reaction protocols (**Scheme 4**).

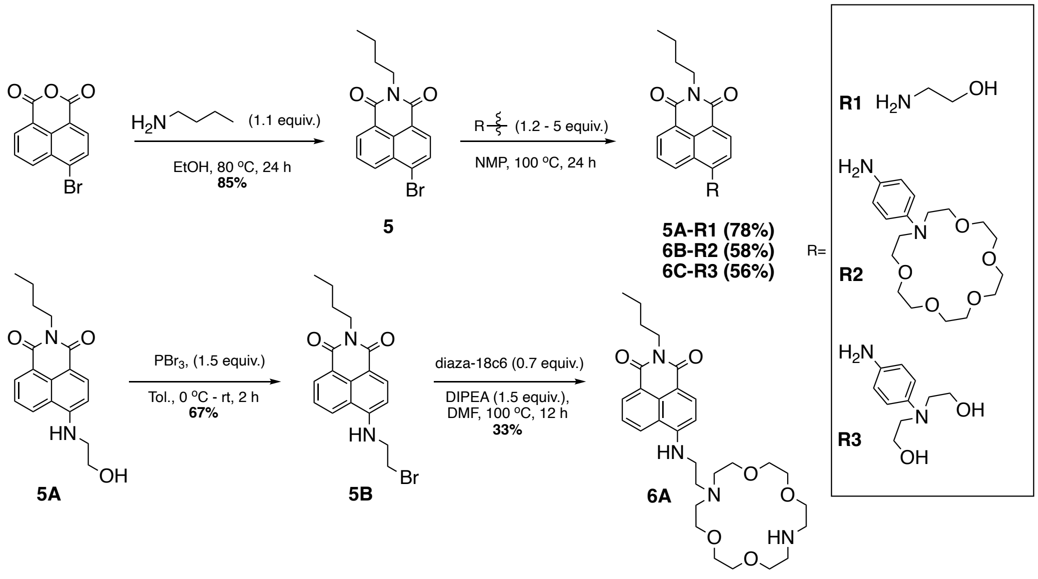

Scheme 4. Synthetic scheme for the preparation of molecular probes **6A-6C**.

4.3.2. UV-Vis absorption studies

All fluorescent probes were measured in acetonitrile solution to determine their photophysical properties. The absorption spectra of all probes shown in **Figure 4.1** (left) appear to have broad peaks around 200-300 nm, and 350-500 nm, which are consistent with the 1,8-naphthalimide chromophore.[146] Probe **6B** and **6C** showed a red-shifted λ_{max} around 450 nm compared to probe **6A** (λ_{max} ~430 nm) due to an extended chromophore effect, presumably from the aniline substituent. It is shown that the first absorption band belongs to the first excited singlet state S1 ($\mathbf{n \rightarrow \pi^{*}}$), followed by the second band S2 ($\mathbf{n \rightarrow \pi^{*}}$). The optical response of sensor 6B, when exposed to different metal cations, was studied with UV/Vis and fluorescence spectroscopy. The addition of mercury and zinc perchlorate solution led to a shift of the absorption maximum from 450 nm to 430 nm, followed by a visible color change from red to yellow in the case of probe **6B. In contrast,** the addition of equivalent amounts of most other metal ions resulted in no change in absorption maxima or corresponding observations of color change (**Figure 4.1,** right). That suggests that it follows the intramolecular charge transfer (ICT) mechanism.

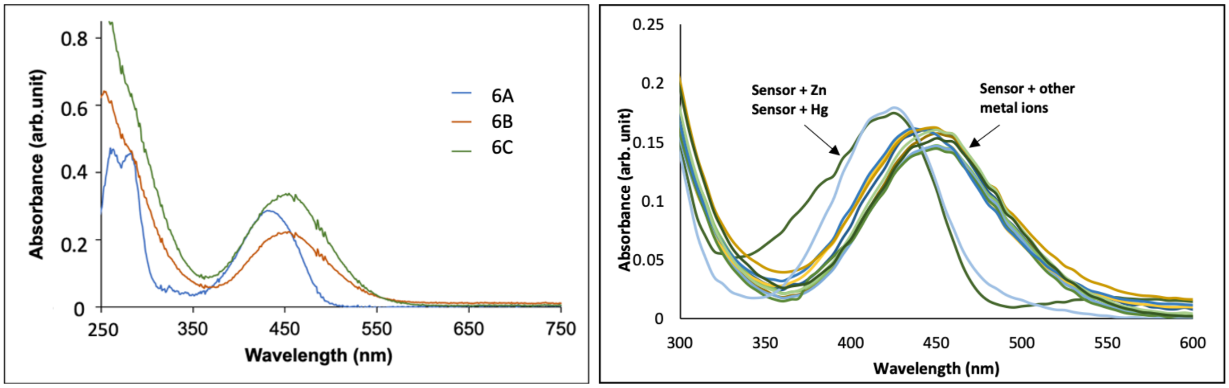

Figure 4.1. Left: UV-vis absorption spectra of probe **6A-6C** at 25 μM in acetonitrile solvent at room temperature. Right: The UV-Vis absorption spectral figure of **6B** at 20 μM concentration in acetonitrile with and without 5 equiv. of metal perchlorate solutions in 9:1 acetonitrile/HEPES buffer mixture at rt.

We investigated different solvents in order to see how they would alter the selectivity (**Figure 4.2**, left). During the measurements, the λ_{max} value shifted to 460 nm, with DCM exhibiting a change in color from red to pink, and the shift of the λ_{max} value to 510 nm due to the low polarity and low viscosity of the solvent, since non-polar solvents are not affected by the dipole effect of the fluorophore. The ethanol was used as a solvent for testing the response to metal perchlorates that had the effect of losing their vibrational fine structure due to their high polarity and increased viscosity compared to Methanol.[149] A Stoke's shift of the maximum absorption wavelength was observed as Hg^{2+} was added, moving from 460 nm to 440 nm, followed by a visible change from red to yellow, while led and other metals did not show any significantly different behavior (**Figure 4.2**, right). Adding zinc perchlorate did not change the absorption, leading to the conclusion that ethanol was the best solvent for the Hg^{2+} sensor.

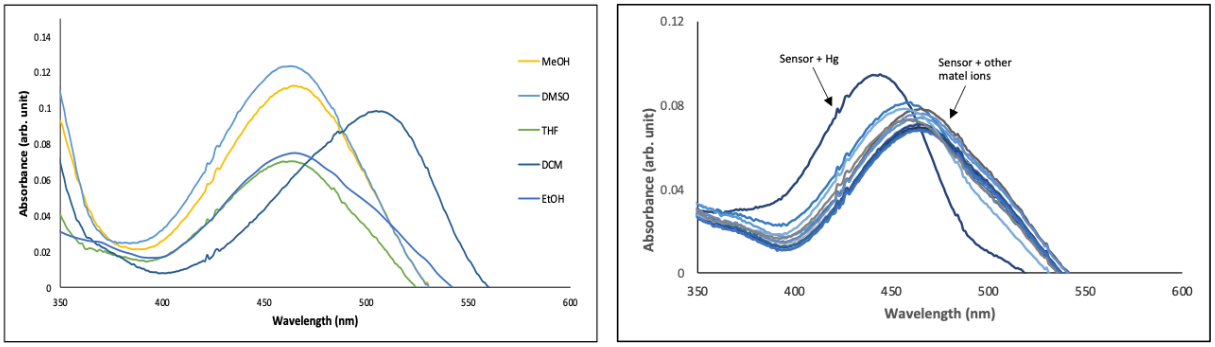

Figure 4.2. Left: UV-vis absorption spectral figure of probe **6B** at 25 μM in different solvents at room temperature. Right: The UV-Vis absorption spectral figure of probe **6B** at 20 μM concentration in ethanol in the absence of metal perchlorate and in the presence of 5 equiv. of different metal perchlorate solutions in 8:2 ethanol/water mixture at rt.

4.3.3. Fluorescence Spectroscopic Studies

Due to the absorption wavelength change that occurred in the spectra of the UV-vis absorbance spectrum after the addition of Hg^{2+} and Zn^{2+} ions, it has been determined that fluorescent absorption was measured at two excitation wavelengths, 430 nm, and 450 nm. There have been several different metal/nonmetal ions used to test the complexation ability of the receptor, such as Ag^{+}, Ba^{2+}, Ca^{2+}, Cu^{2+}, Cd^{2+}, Cs^{2+}, Hg^{2+}, K^{+}, Li^{2+}, Me^{+}, Mg^{2+}, Na^{+}, Pb^{2+}, Rb^{2+}, Sr^{2+}, Zn^{2+}. We maintained the solution of the molecule probe in acetonitrile at 20 μM concentration with the addition of 5 equivalence of metal perchlorates, while the solution of metal perchlorates was prepared at 10 mM concentration in a 9:1 acetonitrile/HEPES buffer. In all cases, the incubation in the dark for 1 minute was preceded by taking the measurements.

As shown in **Figure 4.3** (top), the blue color represents the increase in intensity at wavelength λ_{ex} 430 nm in response to different metal perchlorates. A significant increase in fluorescence is observed between the ions Hg^{2+} and Zn^{2+} for molecule **6B**. In addition to probe **6A** showing no response to any metal, there was no significant difference between the intensity of metal perchlorates and the other metals. To evaluate the sensitivity toward Hg^{2+}, the competition experiment in orange color shown at the bottom in

Figure 4.3 was performed. Using metal perchlorate, Hg^{2+} was added to the probe molecule solution after 1 minute of incubation in the dark. The concentrations of both solutions were maintained at 20 μM of the metal perchlorate equivalence and the Hg^{2+} with 5 mM of the molecule probe. The intensity of the reaction was induced when Hg^{2+} was added to the mixture. Further studies have been conducted to investigate the influence of changes in Hg^{2+} concentration.

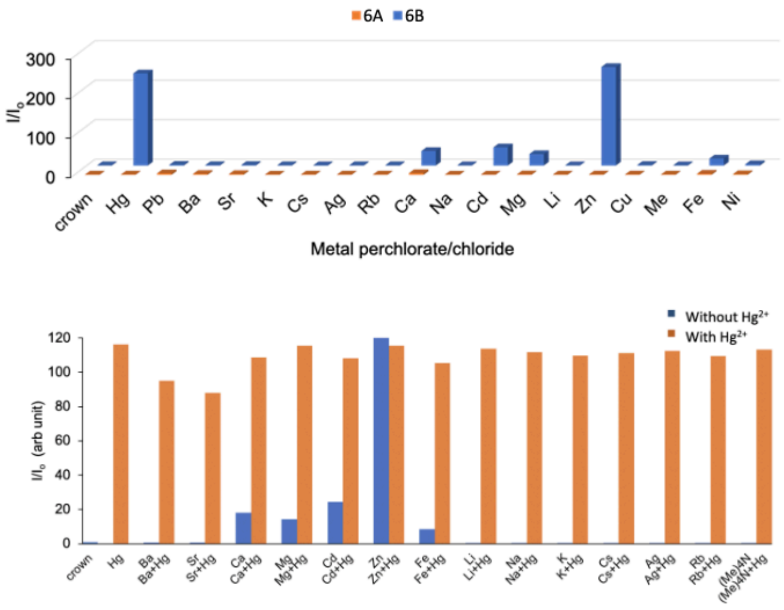

Figure 4.3. Top: Fluorescence spectra of molecule probe **6B** at 20 μM concentration in acetonitrile with different metal perchlorates in 9:1 acetonitrile/HEPES buffer stock solution in 1:5 ratio at $\lambda_{ex.}$ 430 nm. Bottom: Competitive fluorescence response of **6B** (10 μM) in the absence (blue) and in the presence (orange) of Hg^{2+} ions (50 μM) in different metal/non-metal perchlorate (50 μM) in acetonitrile with different metal perchlorates in 9:1 acetonitrile/HEPES buffer stock solution in 1:5 ratio at $\lambda_{ex.}$ 430 nm.

At all concentrations, the solution of the molecule probe is pale orange and does not emit a fluorescent signal. Hg^{2+} and Zn^{2+} at different equivalence and concentrations cause the fluorescent molecule probe color to change from pale orange to yellow. The intensity gradually increases (**Figure 4.4**) from a low intensity with the addition of metal perchlorates to the maximum intensity with the addition of three equivalences of Hg^{2+} and 5 equivalences of Zn^{2+}. As shown in Job's plot analysis (**Figure 4.5**), the ligands bound in acetonitrile with a stoichiometric 1:2 complex with Hg^{2+} perchlorate in a 9:1

acetonitrile/HEPES buffer stock solution to form the stoichiometric complex. As ethanol was changed to the solvent, a change of selectivity was observed, showing the effect of the Hg^{2+} under specific conditions (**Figure 4.6,** right). This was followed by titration studies with Hg^{2+} in ethanol, which demonstrated the increase in fluorescence intensity upon the increasing concentration of Hg (**Figure 4.6,** left).

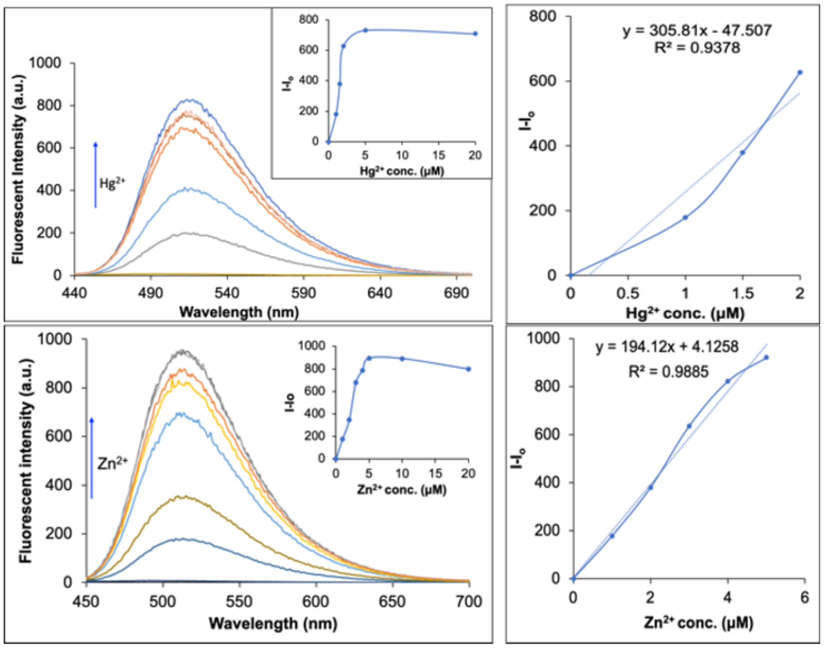

Figure 4.4. Top: Titration fluorescence spectra of **6B** at 20 μM concentration in acetonitrile with Hg^{2+} perchlorate in 9:1 acetonitrile/HEPES buffer stock solution at $\lambda_{ex.}$ 430 nm. Bottom: Titration fluorescence spectra of **6B** at 20 μM concentration in acetonitrile with Zn^{2+} perchlorate in 9:1 acetonitrile/HEPES buffer stock solution at $\lambda_{ex.}$ 430 nm.

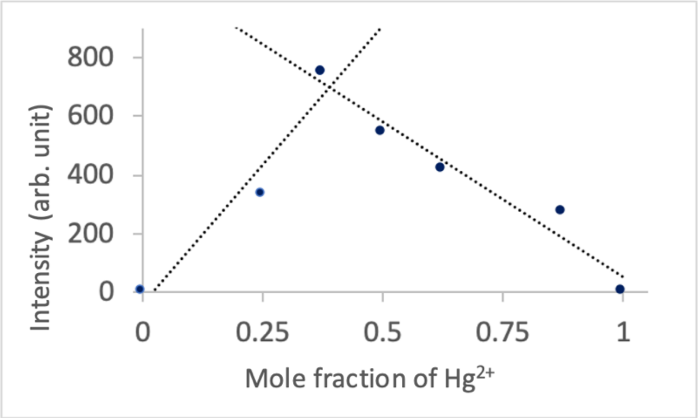

Figure 4.5. Job's plot represents the stoichiometric binding of butyl-1,8-naphtalimide monoaza-18-crown-6 (**6B)** with Hg^{2+} in acetonitrile with metal perchlorate stock solution done in 9:1 acetonitrile/HEPES buffer at $\lambda_{ex.}$ 430 nm

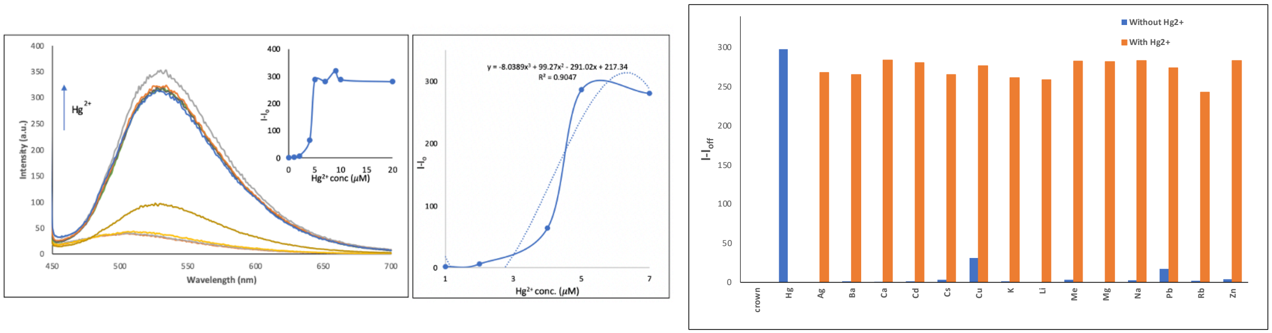

Figure 4.6. Left: Titration fluorescence spectra of **6B** at 20 μM concentration in ethanol with Hg^{2+} perchlorate in 8:2 ethanol/water stock solution at $\lambda_{exc.}$ 430 nm. Right: Competitive fluorescence response of **6B** at 10 μM in the absence (blue) and in the presence (orange) of Hg^{2+} ions at 50 μM in different metal/non-metal perchlorate at 50 μM in ethanol with different metal perchlorates in 8:2 ethanol/water stock solution in 1:5 ratio at $\lambda_{ex.}$ 430 nm.

4.3.4. ^{1}H NMR study

The effect of Hg^{2+} and Zn^{2+} on sensor **6B** was further analyzed through NMR experiments. The initial attempt to study the effect of Hg^{2+} on sensor **6B** in acetonitrile-d$_3$ solution was not successful due to the precipitation of an unknown dark brown solid as well as a significant peak broadening effect. However, the precipitation issue was resolved with the use of CD_3Cl solvent in the case of mercury salt. When mercury and zinc perchlorate salts were added in five equivalents separately to the CD_3Cl and CD_3CN solution respectively containing 14 mM of sensor **6B**, we observed a significant deshielding effect in protons of both phenyl substituent (H7-H10) and naphthalimide ring (H2-H6) concomitant to visual color change from red to yellowish-brown. Crown ether protons were found to have the mixed effect of shielding and deshielding, presumably due to the reorganization of the crown ring upon binding to Hg^{2+} or Zn^{2+} ions (**Figure 4.7**). These preliminary investigations through NMR studies strongly indicate complexation of Hg^{2+} and Zn^{2+} ions with both nitrogen of the phenyl group, thereby affecting intramolecular charge transfer from nitrogen substituents to the imide group in naphthalimide fluorophore; the effect which was further supported by UV-vis result.

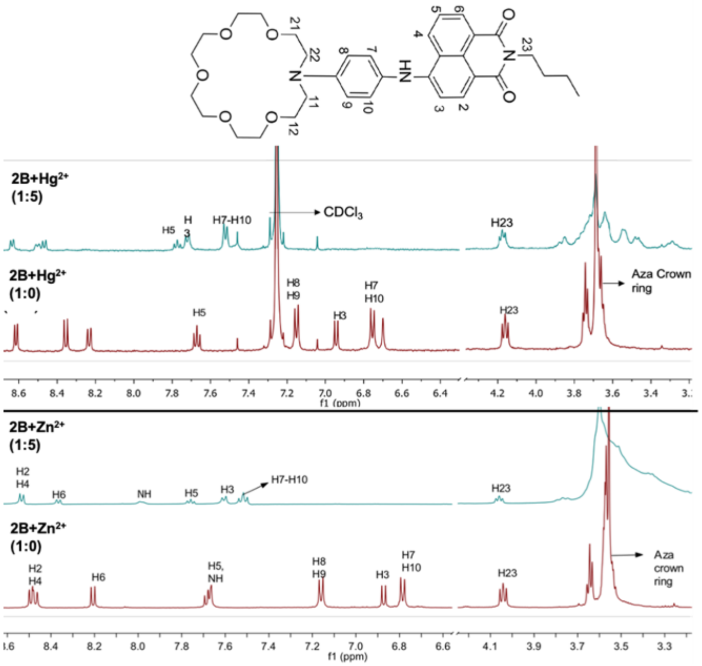

Figure 4.7. NMR spectral figure showing the effect of Zn^{2+} (figure A in CD_3CN) and Hg^{2+} (figure B in $CDCl_3$) on chemical shift values of **6B**; red traces represent NMR spectra of **6B** (14 mM) in the absence of metal ions and blue traces represent NMR spectra of **6B** in the presence of metal ions (5 equiv.); Proton numbering is inconsistent with IUPAC nomenclature

4.3.5. Computational Evaluation

For the optimization and frequency of probe **6B** without (on the left) and with (on the right) Hg^{2+}, computational studies were carried out using the Gaussian 09 program. A polarizable continuum model (PCM), and M06-2X density functional, were used to calculate the calculations in acetonitrile solution with the def2svp basis set. A Multiwfn analyzer and Gaussview were used to determine the visible orbital geometry of the molecule. Unlike the PET mechanism, which decreases the HOMO energy of the receptor molecule in our previous study,[147] we do not observe this in **Figure 4.8**. On the other hand, we can observe that there is a real difference in the conjugation, indicating an increasing HOMO-LUMO energy band, which would support the conclusion that **6B** follows the ICT mechanism. Additional studies are needed to evaluate the tertiary complex suggested from the Jobs plots.

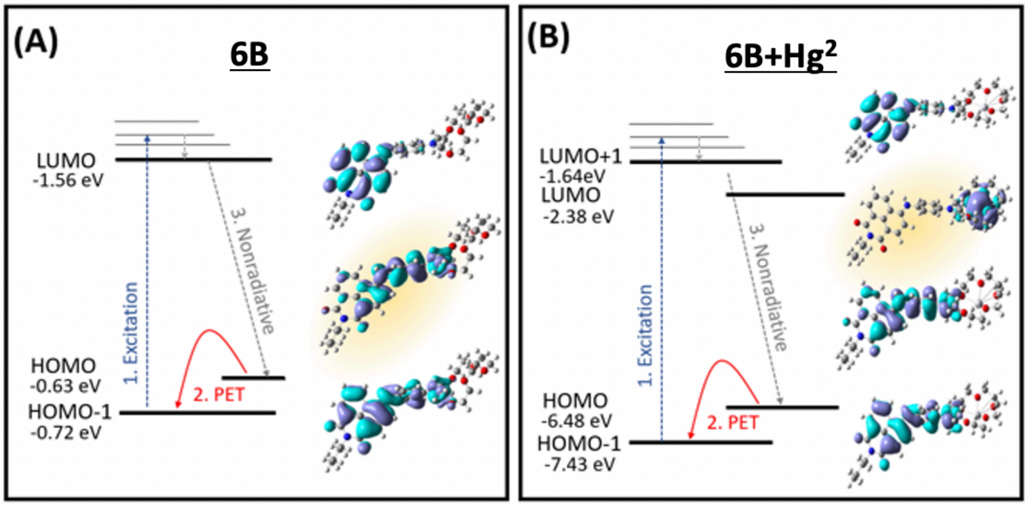

Figure 4.8. Simulated orbitals of **6B**. Enhanced Hg^{2+} selectivity is illustrated by comparing changes in energy of the nitrogen-dominated orbital, highlighted.

4.3.6. Biological Studies

The practical application of Hg^{2+} and Zn^{2+} selective probe **6B** was carried out using a fluorescence imaging study for the sensing of Hg^{2+} ions in living cancer cells. MTT assay performed to examine the toxicity level of the probe **6B** in MCF-7 breast cancer cells showed that the probe is almost non-toxic at a wide range of selected concentrations (0.195 - 100 μM) and is suitable to image cells even at high concentrations of the probe. To image the cells through sensing of Hg^{2+} ions with probe **6B**, two different concentrations of the probe (50 μM and 10 μM) in acetonitrile solution were chosen. In the absence of Hg^{2+} ions, cells treated with the only probe were non-fluorescent. Notably, the cells pretreated with 50 μM of Hg^{2+} ions followed by addition of 50 μM and 10 μM probe **6B** separately in two set of experiments gave bright green fluorescence (**Figure 4.9**). Additional representation of overlay images of fluorescence and bright field clearly demonstrates the ability of probe **6C** to cross cell barriers for sensing Hg^{2+} ions in the cytoplasmic level of the cells.

The cytotoxicity of **6B** against HeLa cells was evaluated using the MTT assay. The cells were exposed to the sample in the concentration range of 0.20 to 100 μM for 24 h. As can be seen in **Figure 4.9**, the HeLa cells exhibited good cell viability in the presence of the probe, indicating that **6B** exerts low cytotoxicity in the concentration range of 0.20–100 μM. We chose 50 μM for intracellular Hg^{2+} detection. The result demonstrates that **6B** shows green fluorescence in the cell pretreated with 50 μM of Hg^{2+}, while no fluorescence is observed in the control group (without Hg^{2+} pretreatment). This finding highlights the potential of **6B** in Hg^{2+} detection in the biological system.

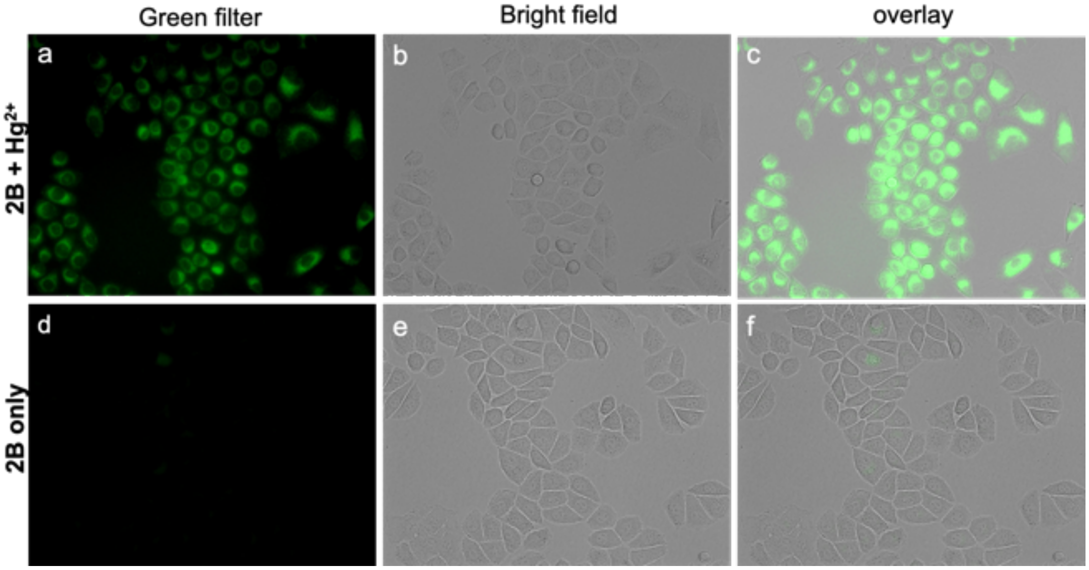

Figure 4.9. Confocal fluorescence images for the detection of probe **6B** (50 μM) in the presence (**6B**+Hg^{2+}: a, b, and c) of Hg^{2+} ions (50 μM) and in the absence (**6B only**; d, e, and f) of Hg^{2+} ions. Image a and d are fluorescence images of 6B and **6B**+Hg^{2+} when excited at 488nm. Image b and we are corresponding bright-field images of fluorescence images a and d respectively. Images c and f are overlay images of both fluorescence and bright field images of a and d respectively.

4.4. Conclusion

As a result, we have synthesized a crown ether naphtalimide fluorophore chemosensor **6B** that showed selectivity for both Hg^{2+} and Zn^{2+} ions with the advantage of the dry sensing chemosensor capability. The ultimate outcome of the research was able to adjust the sensitivity to Hg^{2+} specifically by choosing ethanol as the solvent instead of acetonitrile as the solvent originally used. Further studies need to concentrate on analyzing the LOD and K_d binding of probe **6B** as the next step in the research. The computational and fluorescence studies showed that an intramolecular charge transfer mechanism took place, however more studies with 1:2 stochiometric binding need to be investigated by the computational studies. Chemosensor showed that the probe **6B** is an almost non-toxic MTT assay performed to examine the toxicity level in MCF-7 breast cancer cells. I believe that, for future studies, the dry fluorescence response would support the significance of the sensor ability of the dry state fluorescence response.

Chapter 5. Functional Monomers for Construction of Fluorescent SAM's at Optical Surfaces

5.1. Introduction

One of the first ideas for identifying Ba^{2+} in high-pressure xenon gas was Single-Molecule Fluorescence Imaging. There were three steps to be completed: 1) identification of dyes that give a strong fluorescence response to barium; 2) development of an imaging system that can be used to tag barium in large detectors; and 3) optimizing the detection technique to detect single molecules.[4,31] As mentioned previously, we have discovered dyes that have a strong barium response and we have developed a scanning system detector that can tag barium. At this point, we are in the process of setting up the next step to optimize the detection technique in order to improve our detection ability.

We have previously demonstrated the synthesis and studies of the fluorescent dyes using SMFI microscopy to illustrate the liquid and dry fluorescence barium response in a high-pressure xenon gas environment using air-coupled epifluorescence.[146] There was high selectivity observed between 18-crown-6 and azo-derivatives with different fluorescent receptor groups that did not require deprotonation and were suitable for wet fluorescence and using cyanoacrylate as a support medium for dry fluorescence.

In order to carry out the single-molecule imaging, we envisioned the formation of self-assembled monolayers (SAMs) that contain our fluorescent barium tags in a solvent-free system.[147] A self-assembled monolayer is a molecular assembly that occurs spontaneously through the adsorption of a surfactant with a specific affinity for its headgroup to a substrate.[148] It has been shown that SAMs are used in a wide variety of applications, from protective coatings to use in electrochemical applications to biological applications like constructing interfaces between biological materials, and can be used as an application for dry fluorescence. As the first to report the presence of SAMs on hydroxyl-terminated surfaces (glasses and silicon wafers), Sagiv[151] has made significant advances toward the use of monolayers in nonlinear optical devices, as well as nonlinear optics, electrochemistry, and monolayer catalysis. As a result of SAMs development, we will have more control over the thickness and density of the barium tagging films on the surface, as the reagent adjustment is able to form on a wide range of surfaces (gold, mica, quartz, glass, quartz,).[150,152] Although all of these surfaces are capable of forming monolayers, due to the fact that we intend on using a total internal reflection fluorescence (TIRF) microscopy technique as our aim involving barium tagging, we are limited to surfaces that are both transparent and ideally dielectric materials. Glass is the substrate we used as the target for our investigation, we chose it to start these investigations. Initial studies were also performed on more planar quartz slides.

In this study,[147] we used previously synthesized **18c6-an** molecules with strong fluorescence when exposed to barium in a dry state and a fluorescent instrument that can detect fluorescence via total Internal reflection fluorescence TIRF microscopy under dry conditions under visible light and with a high sensitivity to single ions. For the TIRF microscopy technique, glass coverslips are used since they have the desired transparency. As a result of the piranha solution activating the glass coverslip surface, OH groups are now available for the connection of **18c6-an** dye by the linker (APTES) using hydrocarbon on the linker, allowing the molecules to be distributed evenly into a monolayer. **Figure 5** illustrates the studies using TIRF microscopy with **18c6-an**, clean glass, and glass with an APTES linker attached. Within the experimental error of one another, both glass coverslips activated by piranha and APTES linker had similar intensity profiles. Nevertheless, we notice a significant increase in the intensity profile of the glass when the dye is added.

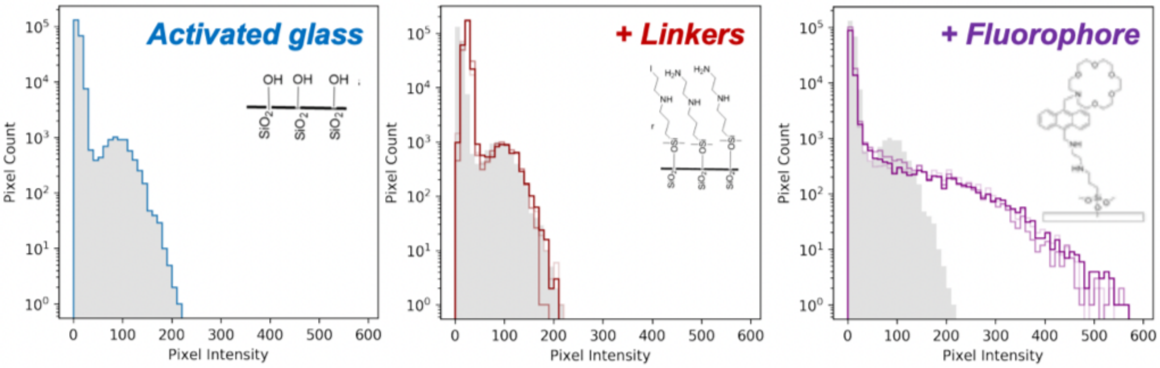

Figure 5. Progression of the number of EMCCD camera pixels capturing at specific intensities from cleaned activated glass (blue), glass with the hydrocarbon linker (red), and glass with **18c6-an** attached, and activated by ions (pink).[146] (Reproduced with the permission from arXiv:1909.04677v1.)

Since we have demonstrated that the monolayer of SAM can be formed by the glass as a substrate and **18c6-an** as a chelating dye by the TRIFT microscopy technique, our goal is to achieve qualitative analysis of the monolayer formation with the integration of different surface techniques, the use of different fluorescence dyes, as well as the use of the naphthylamide fluorophore that has been previously characterized by our group to have a greater sensitivity towards Ba^{2+} and significant “off” state.

For the purposes of single-molecule imaging, the ‘self-assembled monolayers’ SAMs have progressed to the next step in which we have synthesized 18c6-napthalamide molecules with the hydrocarbon chain to bind to the linker. For the qualitative analysis of the self-assembled monolayers, different surface analyzation techniques are employed.

5.2. Synthesis

The functional molecule **4B** was synthesized following known protocols.[146] Next, nucleophilic aromatic substitution (S_NAr) of the aryl bromide (**4B**) with 12-amino lauric acid in NMP, to result in the formation probe **7**. Different conditions were applied as CuI in DMSO for the nucleophilic aromatic substitution, but the product was only collected at 20% yield, so the NMP was decided to be used as the final choice. The last step is the preparation of the active ester using DCC as a coupling agent and NHS ester with carboxylic acid to give the final product **7A** (**Scheme 5**). The NHS ester provides a single reagent for bonding to an amino-functionalized glass substrate. In a similar manner, the **Fluo** and spacer (**9A**) were synthesized (**Scheme 5.1**)

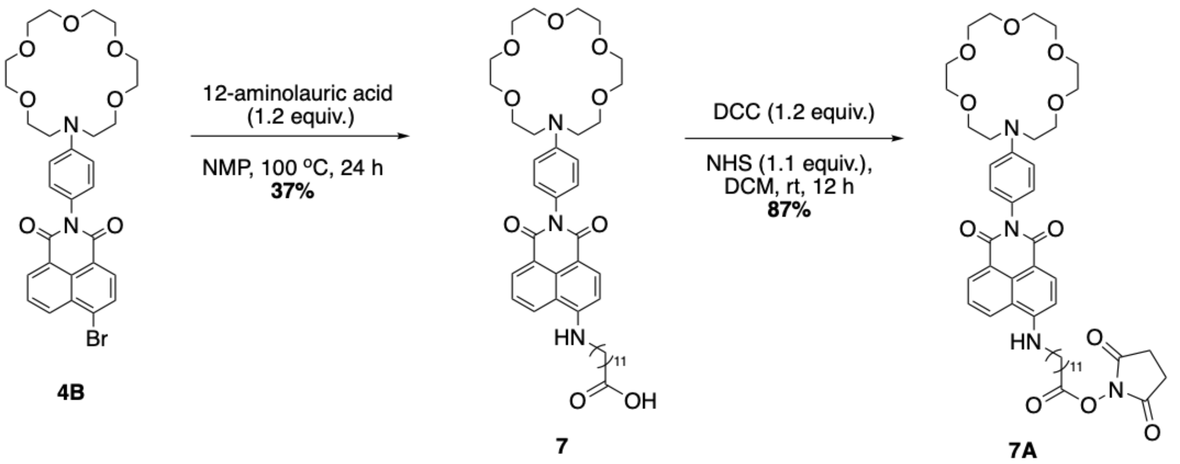

Scheme 5. Synthesis of the 18c6-Napthalimide-NHS molecule **7A**.

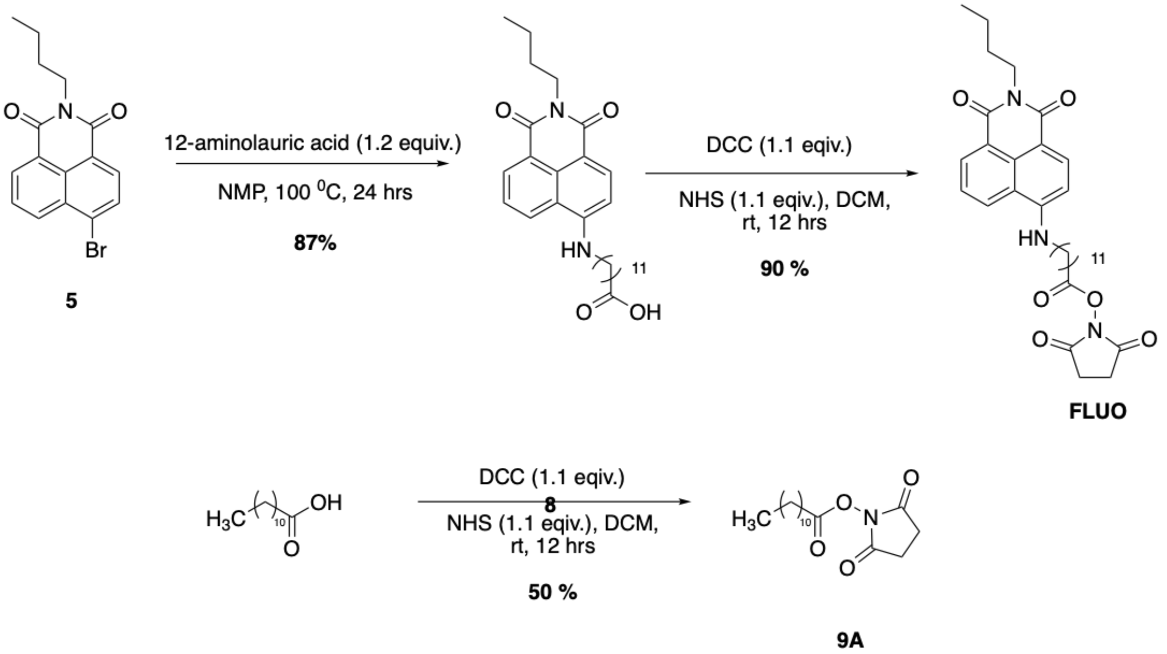

Scheme 5.1. Synthesis of the **Fluo** molecule and spacer **9A**.

5.3 Monolayer preparation

The SAMs were prepared by using a liquid deposition technique (**Figure 5.1**), the glass substrates were cleaned by sonicating in each of the following solvents: DCM, EtOH, and Acetone. Then, the glass substrates were dried in an oven at 200 °C for 10 minutes. After this process, the piranha was used to activate the glass substrates with a 3:1 H_2SO_4/H_2O_2 ratio at a temperature of 100 °C for 2 h. After slides were soaked in piranha for 2 h, slides were sonicated with ultrapure water followed by EtOH sonication and left for drying in an oven at 200 °C for 12 hours. After the slides are activated in piranha solution and dried, we proceed to the addition of APTES, soaking the substrates in a 0.01% solution of (3-aminopropyl)triethoxysilane within freshly distilled toluene for 30 minutes. Afterward, the substrates were sonicated in freshly distilled toluene, followed by sonication in EtOH, and dried under a nitrogen gas stream. To add the fluorescent molecule as well as non-fluorescent alkane spacers **9A** onto the linker, using freshly distilled toluene at different concentrations and equivalence with the difference soaking times described below, followed by the sonication in a solvent used for molecule deposition and EtOH, followed by drying under a nitrogen gas stream.

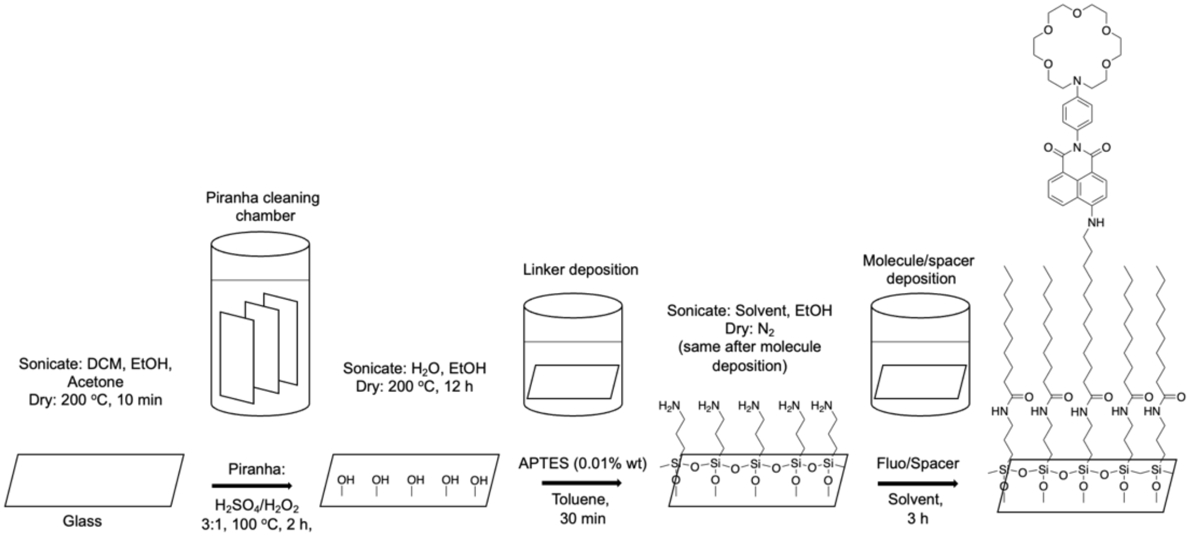

Figure 5.1. Schematic representation of the monolayer preparation.

5.4 Results and discussion

The self-assembled monolayers were investigated to analyze the formation of the strongly bound layer using various technical skills. We utilized the fluorimeter with a solid-state adapter to analyze the formation of the monolayers like in our previous studies,[99], however, due to the functional molecule **7A** having an "off" state before the addition of the metal, observing a fluorescent signal was challenged by considerable light scattering from the glass substrate. Therefore, we decided to proceed with the fluorophore molecule **Fluo** which always has an "on" state and does not require the addition of the metal as well as the fluorescent instrument that was constructed with the help of Nick Byrnes for our investigation of the effects of the timing and concentration of the **Fluo** molecule on monolayer formation. With the APTES constant at 0.01% wt., we used different concentrations (0.15, 0.3, 0.45, 0.6 and 0.9 mM) of the **Fluo** molecule in different solvents (DCM, DMF, Toluene, THF) over varied soaking times (**Figure 5.2**). Due to the solubility of the **Fluo**, toluene was used as the solvent for this study. At first, we noticed that there was no significant difference between the samples, but we observed an increase in fluorescence intensity with an increase in concentration at the longer time of soaking of the substrate (1.5 days). There is a slight drop in the intensity of the signal of the 0.9 mM solution when compared with the lower concentration solutions, and the reproducibility is also reduced. It is interesting to note that the shorter soaking time (6 h) does not demonstrate any trend in increasing intensity with an increasing-concentration.

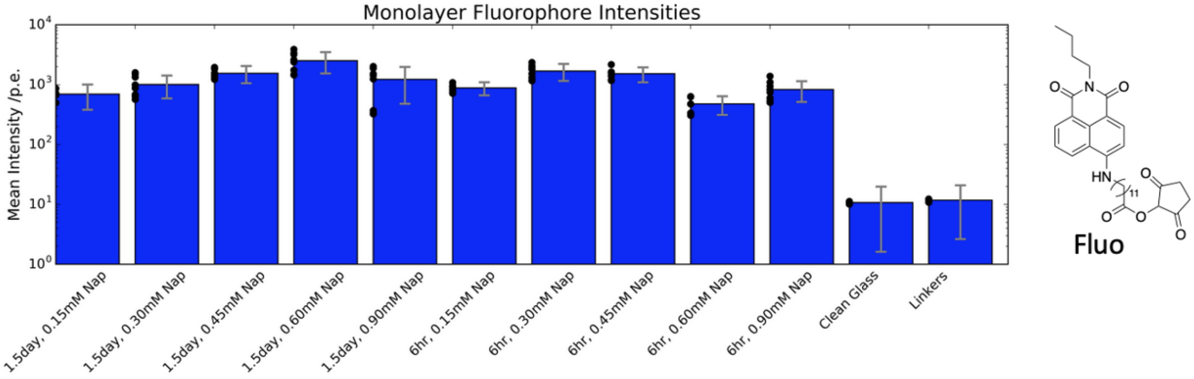

Figure 5.2. Fluorescence microscope response average of two slides (three spots on each) at different times and different concentrations.

Having found that the 0.6 mM Nap (1.5 days) exhibited the highest point of signal in the microscope, we decided to investigate the change in the signal at the lower times using the same fluorescent instrument, and we did find that there was an increase in the signal as the concentration of the solution increased. The increase in signal up to 3 h, with the 1 h and 3 h soaking times showed similar maximum values to the 1.5 days soaking times. The conclusion from our study was that the concentration has effects on the fluorescent properties of our monolayers, but the time of soaking does not show significant improvement after 3 h, so we developed the procedure to follow the 3 hours of soaking time for the further studies of our molecules. It was decided to continue the experiments for the concentration change for **Fluo** in the fluorimeter with the

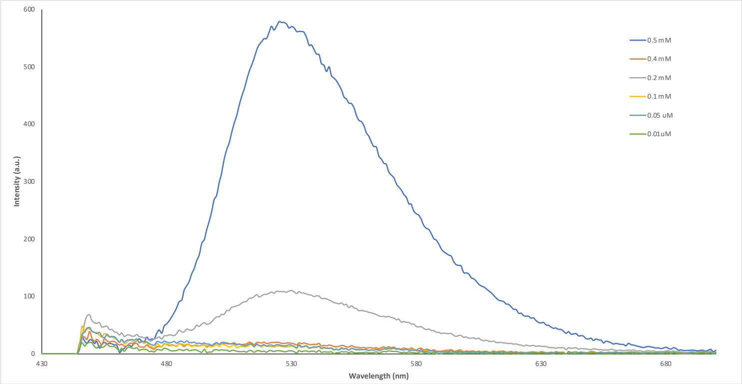

Figure 5.3. Fluorescence spectra of **Fluo** (from 0.05mM to 0.001 mM) on the glass surface with the addition of different spacer **9A** equivalence in toluene at λ_{ex} = 440 nm, at 5:10 slit/width at 3 h soaking time with two spots on two different slides averaged.

solid-state fluorescence adapter from 0.05 mM to 0.001 mM concentrations in the fluorimeter and the results were not consistent. As we can see, 0.05 mM peaks λ_{max} = 577 nm. The 0.05 mM peak shows a higher signal than 0.02 mM; however, the decrease shows the concentration of 0.02 mM showing an even larger signal than 0.04 mM, while the rest of the concentrations are "off" (**Figure 5.3**). In this experiment, it would appear that it would be possible to investigate whether the equivalence of the spacer **9A** can be increased upon adding it to the monolayer formation since we maintained the concentration of the molecule. At **Fluo** 0.1 mM we observed that the intensity at λ_{max} = 365 nm is higher than the previous results. The behavior can be seen in **Figure 5.4** (left) where we can observe that the intensity decreases when the spacer 9A equivalence is increased in order to reduce the concentration of the **Fluo** molecule. On the other hand, with 4 equivalent spacer~~s~~ **9A** introduced to the system, the intensity increased on the fluorescent instrument (**Figure 5.4**, right). This does not show the same behavior as the fluorimeter data and can be viewed as an outlier, in this case, however, we plan on reproducing this study to determine whether there is an issue with the preliminary data at this concentration. In addition, an increase in Fluo concentration can also be observed in a minor shift in λ_{max}, suggesting an interaction between molecules that will have to be further investigated.

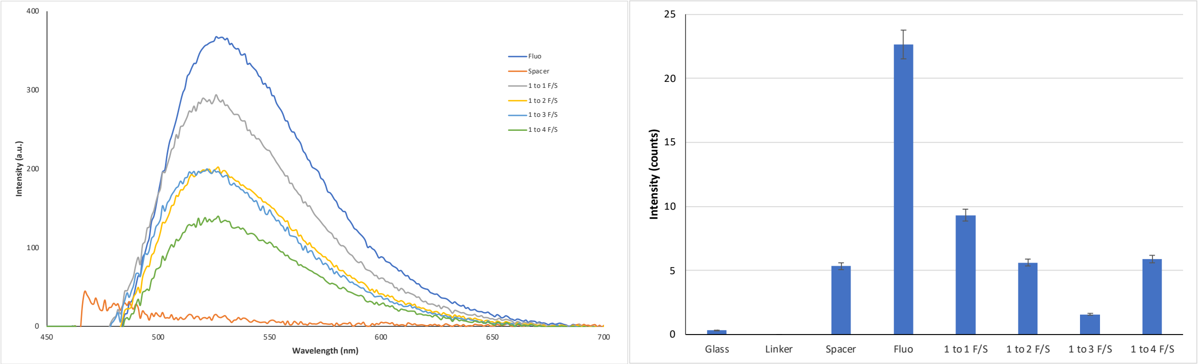

Figure 5.4. Left: Fluorescence spectra of **Fluo** (0.1 mM) on the glass surface with the addition of different spacer **9A** equivalence in toluene at λ_{ex} = 440 nm, at 5:10 slit/width at 3 h soaking time with two spots on two different slides averaged. Right: Fluorescence instrument of the same slides from the fluorescent spectra with two spots on two different slides averaged.

In the first step of the investigation of the functional molecule **7A**, we changed the concentration from 0.05 mM to 0.001 mM and kept the soaking time constant at 3 hours. It appeared from the first trial of using functional molecules that we have similar results to **Fluo**, however, because the molecule is off before the addition of the metal, we are unable to use it in our fluorimeter with the solid-state adapter for the experiment. The fluorescence intensity experiment in **Figure 5.5** using the dry fluorescence solid sample holder for glass substrate imaging showed that there was much scattering signal from the glass, making it difficult to distinguish the actual signal at the lowest concentration. Due to the TIRF microscope's inability to study the high concentrations with the mM concentrations on the microscope and fluorescent instrument giving a large error, we moved to study the lower concentration slides with the higher equivalence of the spacer **9A** under the microscope without further investigation of the monolayers on the fluorimeter. **Figure 5.6** represents the study of the single-molecule level microscopy images of the **7A** at 16.6 μM, 1.66 μM and 0.166 μM concentration respectively (left to right) with 0.8 mM of spacer 9A constant in each sample where we observe that the signal decrease with the concentration decrease of the functional molecule solution.

The self-assembled monolayers were also investigated using various characterization methods in order to analyze the formation of the strongly bound layer. We started our investigation using atomic forced microscopy (AFM). The questions we were hoping to get an answer for are the dept of the monolayer, roughness, and any visible changes in the surface that suggest that the layer is formed. **Figure 5.5 A-F** left, represents the images of the height retrace with the alignment of the rows using the method polynomial degree = 1, with fixed zero gradians and color correction using the highest height between all the samples. What we see is the piranha makes the glass a very rough surface, making it harder to form the smoothing layer. Upon addition of the APTES we can see there all height of the surface got shorter and the formation of the high mountains like formations 6-10 um in diameter by 1 μm in height. As we add additional molecules, we are able to see the decrease in roughness over all of the surface and we suggest that the monolayer is forming but not smooth due to the roughness of the starting piranha surface (**Figure 5.5**, right). In addition, we can also observe the change in the morphology of the monolayer by using a method called the water drop test. It is due to the fact that currently we are able to clearly see the difference between the piranha cleaned glass and the addition of the APTES on the surface (**Figure 5.7**) however the future investigation should include the use of a goniometer so that the angle between the surface sample change can be calculated precisely.[153]

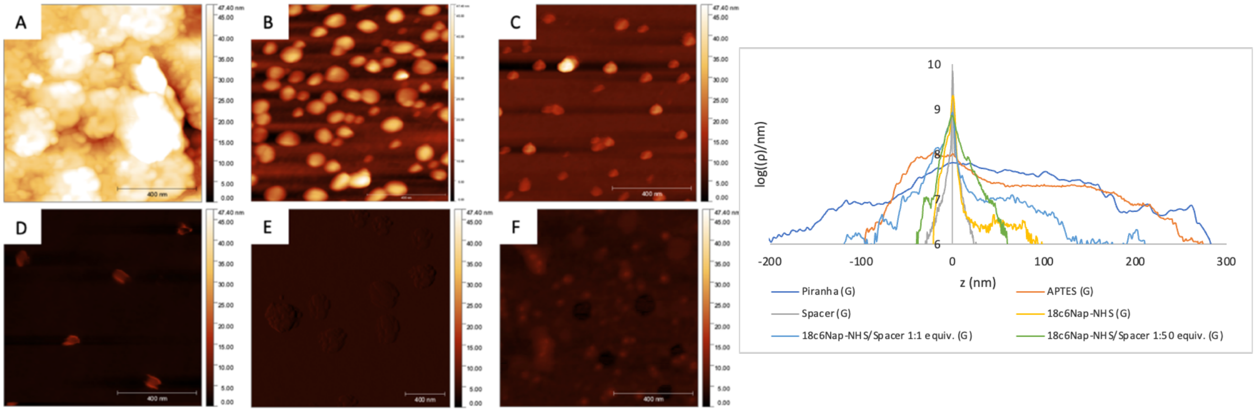

Figure 5.5. Left: AFM images of **A-**piranha cleaned glass; **B-**APTES linker attached to the piranha cleaned glass; **C-**Spacer attached on the APTES linker; **D**-**7A** attached to the APTES linker; **E**-**7A**/Spacer **9A** with 1:1 equiv. at 1μM concentration of the molecule; **F- 7A** /Spacer **9A** with 1:50 equiv. at 1 μM concentration of the molecule. Polynomial degree = 1, with fixed zero gradians and color correction using the highest height between all the samples. Right: Hight distribution from the images plotted and zeroed to the highest sample.

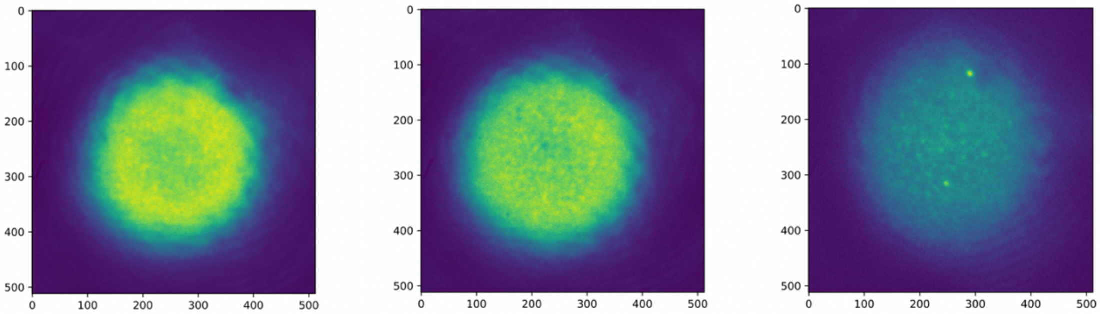

Figure 5.6. Single-molecule level microscopy images of the **7A** at 16.6 μM, 1.66 μM and 0.166 μM concentration respectively (left to right) with 0.8 mM of spacer **9A**.

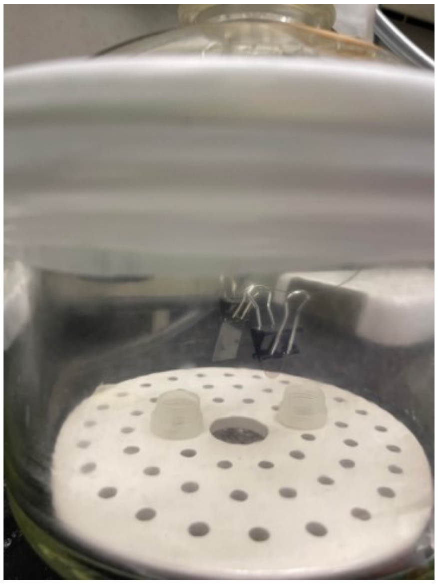

As part of future studies, we are now working on a different deposition method known as vapor deposition.[153] There is an expectation that this would result in a more uniform layer since the molecules should not be affected by the solvent diffusion rate, as well as avoiding the possibility of the particles stocking on the top of one another and forming towers. The assembly of the apparatus, taking the desiccator, and placing two plastic cups filled with 30 μL of APTES and another cup filled with 10 μL of DIPEA, was the starting point of the experiment.[154] In order to attach the piranha cleaned glass to the top of the desiccator, the clips and the metal rods were used. After placing the desiccator under vacuum for 30 minutes, followed by nitrogen purging, was followed by leaving the samples in the desiccator for curing. n the AFM data analysis, there were no signs of tower structures formed in the glass-like previously observed following the addition of APTES, and it was surprising to note there was no roughness on the piranha cleaned glass.

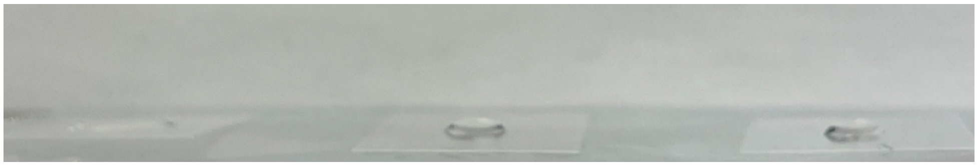

Figure 5.7. Waterdrop test using ultrapure water from a Water Pro BT water station (30 µL on each surface), from left to the right: Piranha glass, APTES linker, Functional molecule **7A**/Spacer **9A**.

5.5 Conclusion

Our recent studies have resulted in the development of quantitative methods that can be implemented in studies of SAM formations in the future. In addition to being able to use the single fluorescent imaging microscopy technique, we were also able to control the equivalence of spacers as well as decreasing the molecule concentration in order to clearly see the individual molecules on the images. In the next phase of the research, we will be extending the modification to a vapor deposition method as well as using different analytical techniques, such as substituting piranha cleaning with laser surface activation. Our studies using AFM were able to provide the surface image of the single APTES molecule formed from the vapor deposition method, which we would like to investigate in more depth (**Figure 5.8**). It is also important to carry out the water drop angle calculation test, which will serve to quantify the differences in surface changes so that the morphology of monolayers is also quantified.

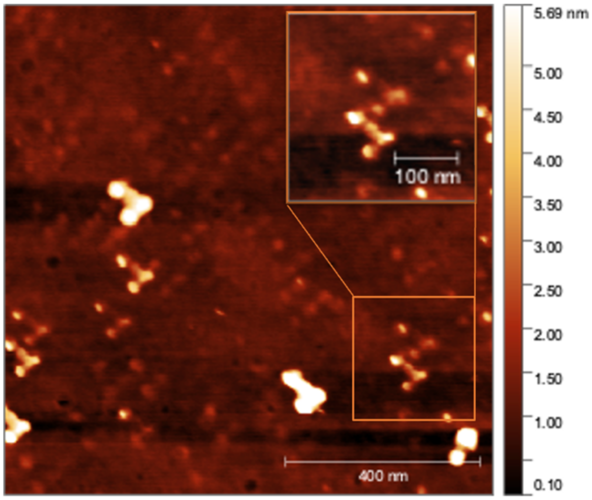

Figure 5.8. AFM images of APTES linker attached to the piranha cleaned glass via vapor deposition method. Polynomial degree = 1, with fixed zero gradians and color correction using the highest height between all the samples.

Appendix A list of abbreviations

0vββ	neutrinoless double-beta decay
AFM	atomic force microscopy
HPGXe	high-pressure gaseous Xe
HPXeEL-TPC	high-pressure gaseous xenon electroluminescent time projection chamber
Kd	dissociation constants
NMR	nuclear magnetic resonance
PET	photoinduced electron transfer
RF	radiofrequency
SMFI	single-molecule fluorescent imaging
yr.	year
%	Percent
°C	Celsius
15c5	monoaza-15-crown-5 ether
18c6	monoaza-18-crown-6 ether
21c7	monoaza-21-crown-7 ether
Å	angstrom
an	anthracene
APTES	(3-Aminopropyl)triethoxysilane
BAPTA	(1,2-bis(o-aminophenoxy)ethane-N,N,N′,N′-tetraacetic acid)
BnBr	benzyl bromide
ca.	around
def2-SVP	split valence polarization
DFT	density function theory
DMF	dimethylformamide
e	electron
EM-CCD	Electron Multiplying Charge-Coupled Device
equiv.	equivalence
EtOH	ethanol
eV	electron volt
EXO-200	Enriched Xenon Observatory
FLUO	fluorescent indicator
FWHM	full width at half maximum
GXe	gas xenon
h	hour
HOMOfree	highest occupied molecular orbital
ICP	intramolecular charge transfer
ICP-MS	Inductively coupled plasma mass spectrometry
k	slope between intensities
kT	product of Boltzmann constant
L	liter
lin	linear
LOD = 3σ/k	limit of detection
LSXe	liquid scintillator
LUMO	lowest unoccupied
LXE	liquid xenon
m	meter
M	molar
M06-2X	global hybrid functional with 54% HF exchange
MeCN	acetonitrile
min	minute
mL	milliliter
mM	milli molar

mm^2	millimeter square
MOhm	ultrapure water
mol	mol
mW	milli watt
n	nano
NEXT-100	Neutrino Experiment with a Xenon TPC
p	pico
PCM	polarizable continuum model
Psi	unit of pressure
py	pyrene
R&D	research and development
R^2	linear regression
Rf	retention factor
ROI	region of interest
rt	room temperature
SDD	solid-state drive
SMD	surface-mount device
SN_2	nucleophilic substitution reaction
STP	standard temperature and pressure
TDDFT	time-dependent density-functional theory
TIRFM	total internal reflection fluorescence microscope
TPC	time projection chamber
TRIS	tris(hydroxymethyl)aminomethane
Triton-X	detergent
UV	spectroscopy
λ_{ex}	excitation wavelength
λ_{max}	maximum wavelength
μ	micro
σ	standard deviation

Appendix B Experimental procedure

B1. Experimental Procedure for Chapter 2

1.1. General procedure

Commercially available chemicals were purchased from Alfa Aesar, Milipore Sigma and Acros Organics and were used without further purification, unless otherwise specified. Deionized (DI) water for ultratrace analysis was purchased from Sigma Aldrich and acetonitrile used was of LCMS grade. All reactions were performed under atmospheric conditions unless otherwise mentioned. ^1H NMRs were acquired on 300 MHz and 500 MHz spectrometers and referenced to the internal solvent signals (7.26 ppm in $CDCl_3$ or 3.33 ppm in CD_3OD). ^{13}C NMRs were acquired on 75 MHz and 125 MHz spectrometers referenced to the internal solvent signals (central peak 77.00 ppm in $CDCl_3$ or 45.00 ppm in CD_3OD). NMR data are reported as follows: chemical shift (in ppm, δ), integration, multiplicity (s = singlet, d = doublet, t = triplet, q = quartet, m = multiplet, br = broad), coupling constant (in Hz). Thin-layer chromatography was performed on silica gel-coated aluminium plates (EMD Merck F254, 250 μm thickness). 254 nm ultraviolet light and ninhydrin stain (for amine-containing molecules) were used to visualize spots. Flash chromatography was performed over Silicycle Silicaflash P60 silica gel (mesh 230–400) and standard grade activated Alumina (mesh 50–300). Melting points were recorded in capillary tubes on a Mel-Temp II apparatus and were uncorrected. IR spectra were recorded in Bruker Alpha-P FT-IR Spectrometer by attenuated total reflectance on a diamond sample plate. HRMS data were recorded in Shimadzu TOF spectrometer in the Shimadzu Center for Advanced Analytical Chemistry at UT Arlington.

All fluorescence spectra were measured in a Cary Eclipse Fluorescence Spectrophotometer from Agilent Technologies (Product Number G8800A) at 25 °C. Unless otherwise specified, instrumental set up includes: PMT detector voltage = High, Excitation filter = Auto, Emission filter = Open, Excitation slit width = 5 nm, Emission slit width = 5 nm, scan control = medium, spectral range = 300 nm to 600 nm. For each species the λ_{max} value was first established via a two-dimensional excitation/ emission scan (for example, **Figure 2.3.1**) to establish the excitation wavelength for subsequent tests.

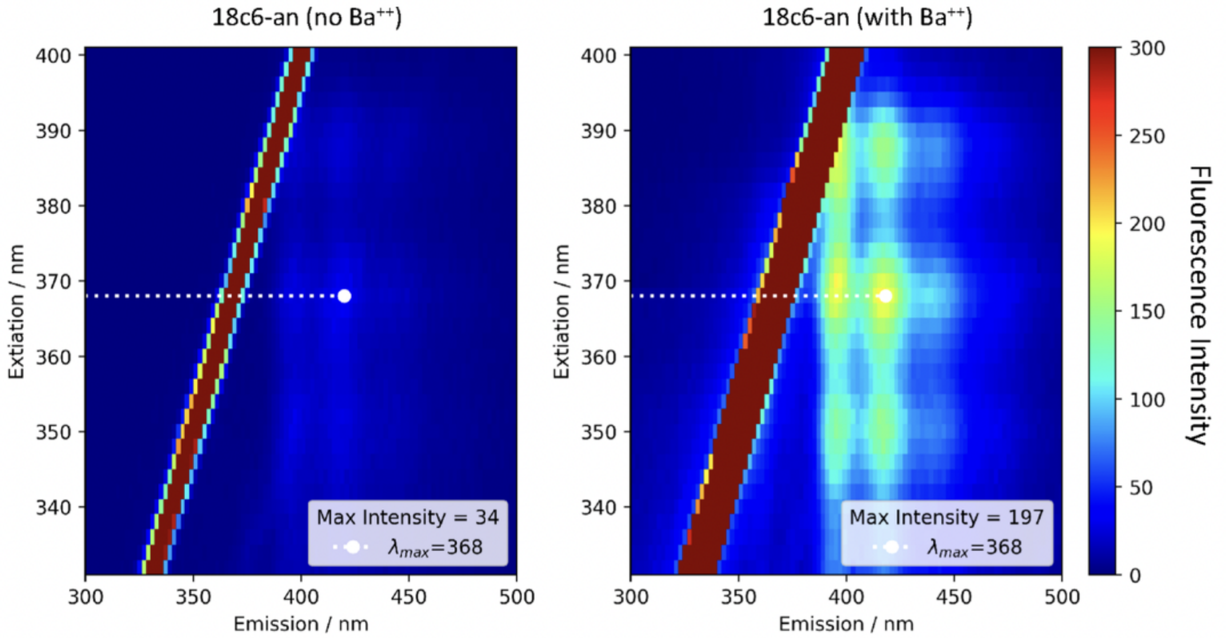

Figure 2.3.1. Fluorescence response of **18c6-an** shown as a function of emission and excitation. The diagonal band represents directly reflected/scattered light.

Fluorescence Studies: TRIS [tris(hydroxymethyl)aminomethane] buffer was prepared at 20 mM concentration and the pH of the solution was adjusted to 10.1 by titrating with 1 M NaOH. Stock solutions for fluorescence studies were prepared by dissolving the appropriate sample in 10:1 TRIS buffer and acetonitrile mixture using sonication and vortex instrument for total of 30 minutes. Different fluorescence samples in wet studies were prepared at concentration of 2 μM by diluting the appropriate volume of stock solution with TRIS buffer. Stock solution of barium (150 mM) was prepared by dissolving $BaClO_4$ salt in TRIS buffer. Samples were incubated for five minutes before reading the fluorescence intensity.

Jobs Plot Analysis: Each sample for Job's plot was prepared by maintaining the total concentration of barium solution and **18c6-an** sample at 40 μM (**Figure 2.10**). Fluorescence intensity was measured by obtaining the difference in fluorescence intensity value at 417 nm between sample with and without Barium. Fluorescence intensity at 1 mole fraction of **18c6-an** sample was normalized to 0.

Micelle Triton-X Studies: Critical micelle concentration was measured by obtaining the Icomplex/ Ifree values against varying concentration of Triton-X. The concentration of **18c6-py** sample and barium perchlorate solution was fixed at 2.1 μM and 7.5 mM respectively for each sample analyzed. Icomplex refers to fluorescence intensity of solution of Triton-X, **18c6-py** and barium and Ifree refers to the fluorescence intensity of solution of Triton-X and **18c6-py** without Barium. Critical micelle concentration was obtained using linear squares fitting method for fluorescence emission at 376 nm during excitation at 342 nm against increasing concentrations of Triton-X.

1.2. Synthesis

1-pyrenemethyl bromide (IV-b)[66,67] and 9-anthacenemethyl bromide[65] (IV-c):

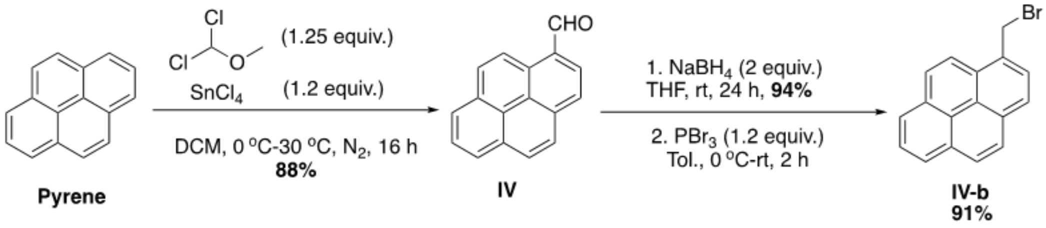

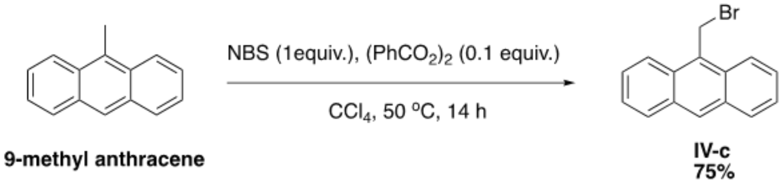

The synthesis of bromomethylpyrene **IV-b** was accomplished following the standard methodology described initially in Ref. 37 and 64. Briefly, pyrene was formylated with dichloromethyl methyl ether as a surrogate for chloroformate, when added to tin tetrachloride. The Friedel-Craft's acylation is achieved in good yields to provide **IV**. Reduction of the aldehyde under standard sodium borohydride conditions followed by PBr_3 mediated bromination led to **IV-b** in 72% overall yield. The 9-bromomethylanthracene **IV-c** was prepared directly through radical benzylic bromination of 9-methylanthracene with *N*-bromo succinimide and benzoyl peroxide initiator in one step to give fairly pure **IV-c**, which is pure enough to be used in subsequent reactions without further purification.

1-pyrenemethyl carboxaldehyde (IV)[66]: Pyrene (2.0 g, 10.0 mmol) was dissolved in 50 mL freshly distilled dichloromethane. The solution was cooled to 0 °C and purged with nitrogen, after which $SnCl_4$ (1.65 mL, 12.0 mmol) was added at once via microsyringe. α,α'-dichloromethyl methyl ether (1.15 mL, 12.5 mmol) was then added dropwise under N_2 while maintaining temperature below 5 °C. The resulting mixture was warmed slowly to reflux over 2 hours and further stirred for 16 hours at reflux conditions. After the completion of the reaction, the reaction mixture was first cooled below 10 °C, diluted with 25 mL dichloromethane, and hydrolyzed by carefully adding 50 mL cold water. The immiscible layers were suspended in a separatory funnel and the organic phase was separated and dried under Na_2SO_4. The crude product was concentrated in rotary evaporator and purified using column chromatography in silica gel (hexanes: ethyl acetate, 10:1) to obtain yellow solid Pyrene-4-carbaldehyde as the desired product (2.02 g, 88%). ^{1}H NMR (500 MHz, $CDCl_3$) δ 10.72 (s, 1H), 9.34 (d, *J* = 9.3 Hz, 1H), 8.36 (d, *J* = 7.9 Hz, 1H), 8.28 – 8.21 (m, 3H), 8.20 – 8.13 (m, 2H), 8.09 – 7.98 (m, 2H). ^{13}C{^{1}H} NMR (125 MHz, $CDCl_3$) δ 193.1, 135.5, 131.4, 131.0, 130.9, 130.8, 130.7, 130.4, 127.3, 127.2, 127.1, 126.9, 126.6, 124.6, 124.5, 124.0, 123.0.

1-pyrenemethanol (IV-a)[67]: $NaBH_4$ (152 mg, 4.0 mmol) was added in small portion into the solution of 1-pyrene-carboxaldehyde **IV** (461 mg, 2.0 mmol) in dry THF (10 mL) at room temperature. The reaction mixture was stirred for 16 hours after which a few drops (2-3 drops) of acetic acid were added to quench the excess $NaBH_4$. The clear solution was concentrated in a rotary evaporator. The resulting solid was dissolved in 15 mL dichloromethane and washed with 5 mL water twice. The washed organic solution was dried with anhydrous sodium sulfate and was concentrated to give pale-yellow solid 1-pyrenemethanol as the desired product. (441 mg, 94%). ^{1}H NMR (500 MHz, $CDCl_3$) δ 8.24 (d, *J* = 9.2 Hz, 1H), 8.16 (d, *J* = 7.3 Hz, 2H), 8.07 – 7.92 (m, 6H), 5.29 (s, 2H). ^{13}C{^{1}H} NMR (125 MHz, $CDCl_3$) δ 133.7, 131.2, 131.2, 130.8, 128.7, 127.8, 127.4, 127.4, 126.0, 125.9, 125.3, 125.3, 124.9, 124.7, 124.7, 122.9, 63.7.

1-pyrenemethyl bromide (IV-b)[67]: IV-a (100 mg, 0.43 mmol) was dissolved in 5 mL freshly distilled toluene and the reaction vial was sealed properly with rubber septum. PBr_3 (49 µL, 0.517 mmol) was added dropwise over 5 minutes at 0 °C and the reaction mixture was stirred for 1 hour at 0 °C and was slowly brought to room temperature. 2 mL saturated Na_2CO_3 was added slowly. The crude product was extracted using 5 mL dichloromethane twice. The combined organic phase was dried under anhydrous Na_2SO_4 and concentrated to obtain pale yellow solid. The crude solid was recrystallized in methanol to give pale yellow solid 1-pyrenemethyl bromide (**IV-b**) as a desired product (115 mg, 91%). Mp 138-140 °C. ^{1}H NMR (500 MHz, $CDCl_3$) δ 8.36 (d, *J* = 9.2 Hz, 1H), 8.22 (t, *J* = 7.0 Hz, 2H), 8.20 (d, *J* = 3.4 Hz, 1H), 8.12 – 7.98 (m, 5H), 5.24 (s, 2H); $^{13}C\{^{1}H\}$ NMR (125 MHz, $CDCl_3$) δ 132.0, 131.3, 130.8, 130.6, 129.1, 128.3, 128.1, 127.8, 127.4, 126.3, 125.7, 125.7, 125.2, 124.9, 124.7, 122.9, 32.3; IR (neat, cm^{-1}): 3035, 2988, 2954, 1594.

9-anthracenemethyl bromide (IV-c)[3]: A solution of 9-methyl anthracene (577 mg, 3.0 mmol), NBS (534 mg, 3 mmol) and benzoyl peroxide (75 mg, 0.3 mmol) in 10 mL CCl_4 was stirred for 14 hours at 50 °C. Solution was cooled to room temperature and undissolved solid was filtered and washed with 5 mL diethyl ether. Crude solid product was used as it is for the next step without further purification.

***N*-protected protected diethanolamine derivatives[63]:**

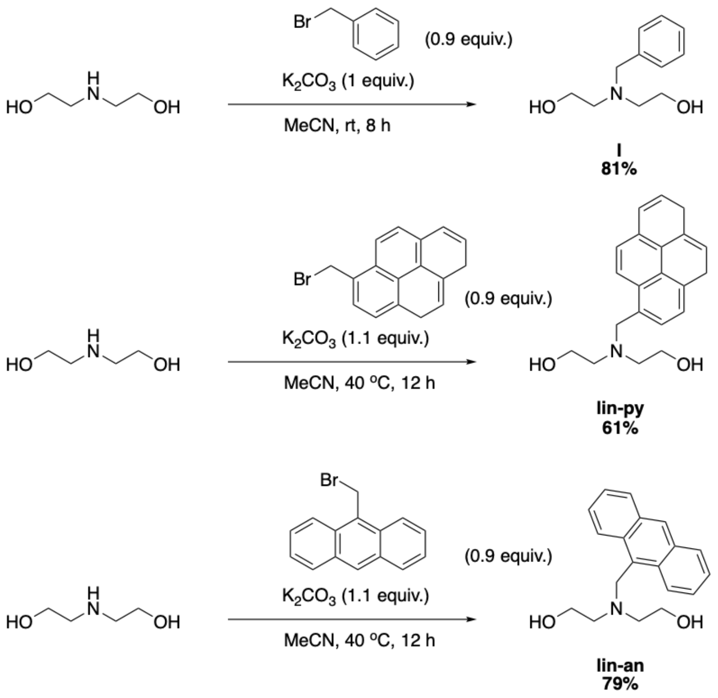

During the construction of the aza-crown ether systems, we found that better overall yields were obtained by the selective *N*-protection of diethanolamine. Benzyl protection proved more fruitful than N-Boc, based on our comparative studies[65]. The standard N-benzyl protection strategy was carried out with inorganic potassium carboxylate in acetonitrile to produce N-benzyl diethanolamine in good yield. Fortuitously, this approach was effective in producing N-pyrenylmethyldiethanolamine (**lin-py**) and N-anthracenylmethyldiethanolamine (**lin-an**) at slightly elevated temperatures, which were used as acyclic controls for the wet and dry studies in our report.

2,2'-(benzylazanediyl)diethanol (I): Benzyl bromide (3 mL, 25 mmol) was added dropwise into the solution of diethanolamine (2 g, 20 mmol) and potassium carbonate (3.4 g, 25 mmol) in 15 mL acetonitrile over 15 minutes at room temperature. The resulting solution was stirred for 14 hours at room temperature. Undissolved solid particles were filtered and washed with 5 mL acetonitrile. Filtrate was concentrated under rotary evaporator under reduced pressure. Crude product was purified in silica gel chromatography using hexanes and ethyl acetate in 1:1 ratio to obtain desired product as colorless liquid (3.15 g, 81%). ^{1}H NMR (500 MHz, $CDCl_3$) δ 7.34 – 7.12 (m, 5H), 3.66 (s, 2H), 3.56 (t, *J* = 5.4 Hz, 4H), 2.65 (t, *J* = 5.4 Hz, 4H); ^{13}C{^{1}H} NMR (125 MHz, $CDCl_3$) δ 138.7, 128.9, 128.3, 127.1, 59.5, 59.1, 55.7.

2,2'-((pyren-1-ylmethyl)azanediyl)diethanol (lin-py): IV-b or **IV-c** (0.9 mmol) was added into the solution of diethanolamine (105 mg, 1.0 mmol) and potassium carbonate (152 mg, 1.1 mmol) in 5 mL acetonitrile. The resulting solution was stirred for 14 hours at 40 °C. The solution was diluted with 5 mL acetonitrile and the undissolved solid particles were filtered and washed with 5 mL acetonitrile. Filtrate was concentrated under rotary evaporator under reduced pressure. Crude product was purified in silica gel chromatography using hexanes and ethyl acetate in 1:1 ratio to obtain desired product as pale yellow solid (176 mg, 61%). Mp 92 °C (decomp.). ^{1}H NMR (500 MHz, $CDCl_3$) δ 8.48 (d, *J* = 9.2 Hz, 1H), 8.18 (d, *J* = 7.6 Hz, 2H), 8.13 (dd, *J* = 10.9, 8.6 Hz, 2H), 8.06 – 7.95 (m, 4H), 4.39 (s, 2H), 3.57 (t, *J* = 5.3 Hz, 4H), 2.81 (t, *J* = 5.3 Hz, 4H); ^{13}C{^{1}H} NMR (125 MHz, $CDCl_3$) δ 132.1, 131.4, 131.1, 130.9, 129.8, 128.4, 127.9, 127.5, 127.4, 126.1, 125.3, 125.2, 124.9, 124.6, 123.3, , 59.9, 58.5, 56.2; IR (neat, cm- 1): 3253 (br), 3045, 2941, 2850, 1139; HRMS (ESI) calcd for C21H22NO2 [M+H]+, 320.1645; found, 320.1648.

2,2'-((anthracen-9-ylmethyl)azanediyl)diethanol (lin-an) lin-an was synthesized following a general reaction condition like **lin-py** (210 mg, 79%). Yellow solid. Mp 85 °C (decomp.); ^{1}H NMR (500 MHz, $CDCl_3$) δ 8.47 (s, 1H), 8.45 (d, *J* = 4.5 Hz, 2H), 8.02 (d, *J* = 8.4 Hz, 2H), 7.59 – 7.51 (m, 2H), 7.52 – 7.43 (m, 2H), 4.72 (s, 2H), 3.54 (t, *J* = 5.3 Hz, 4H), 2.82 (t, *J* = 5.3 Hz, 4H); ^{13}C{^{1}H} NMR (125 MHz, $CDCl_3$) δ 131.5, 131.3, 129.5, 128.2, 126.3, 125.0, 124.3, 59.9, 56.0, 51.7; IR (neat, cm-1): 3220 (br), 3058, 2950, 2858, 1125; HRMS (ESI) calcd for C19H22NO2 [M+H]+, 296.1645 found, 296.1644.

Ethylene glycol derivatives[64]**:**

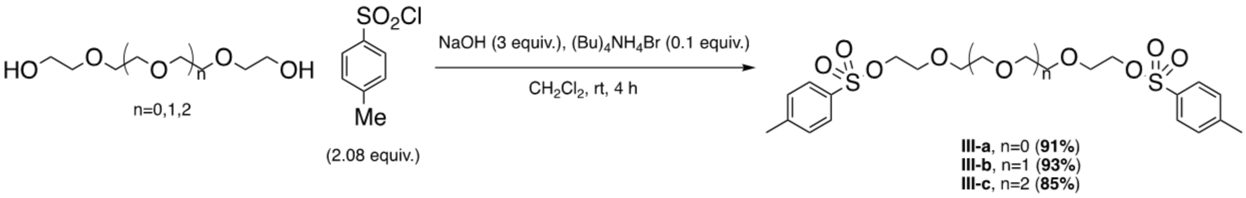

Terminally activated polyethylene glycol derivatives were prepared for cyclization with **I** by known methods[63]. Dimeric, trimeric, and tetrameric diols were reacted with toluenesulfonyl chloride under basic and phase transfer conditions to prepare the ditosylated crown ether fragments **IIIa-c** in excellent yields. A solution of p- toluenesulfonyl chloride (3.96 g, 20.8 mmol) in 10 mL CH_2Cl_2 was added dropwise into the mixture of NaOH (1.2 g, 30.0 mmol), diol (10.0 mmol) and tetrabutylammonium bromide (1.0 mmol) in 20 mL of water and CH_2Cl_2 (1:1) over 15 minutes at room temperature. The resulting mixture was stirred vigorously for 4 hours at room temperature. Organic phase was separated and washed with 5 mL water (X3). The combined organic phase was dried under anhydrous Na_2SO_4. The crude product was concentrated in rotary evaporator in reduced pressure and finally dried under high vacuum. Crude product was used as it is, and no further purification was carried out. In case of **III-a**, the crude product was obtained as white solid which was purified by recrystallization in methanol to obtain the desired product as white crystalline solid.

Triethylene glycol bis-p-toluenesulfonate (IIIa): White crystalline solid (91%). ^{1}H NMR (500 MHz, $CDCl_3$) δ 7.78 (d, *J* = 8.2 Hz, 4H), 7.33 (d, *J* = 8.1 Hz, 4H), 4.16 – 4.08 (m, 4H), 3.66 – 3.61 (m, 4H), 3.51 (s, 4H), 2.43 (s, 6H); ^{13}C{^{1}H} NMR (125 MHz, $CDCl_3$) δ 144.9, 133.0, 129.9, 128.0, 70.7, 69.3, 68.8, 21.7.

Tetraethylene glycol bis-p-toluenesulfonate (IIIb): Clear Liquid (91%). ^{1}H NMR (500 MHz, $CDCl_3$) δ 7.74 (d, *J* = 8.3 Hz, 4H), 7.30 (dd, *J* = 8.3, 4H), 4.20 – 3.92 (m, 4H), 3.63 (m, 4H), 3.53 – 3.46 (m, 8H), 2.40 (s, 6H); ^{13}C{^{1}H} NMR (125 MHz, $CDCl_3$) δ 144.9, 132.8, 129.9, 127.8, 70.5, 70.3, 69.4, 68.5, 21.5.

Pentaethylene glycol bis-p-toluenesulfonate (IIIc): Clear Liquid (91%). ^{1}H NMR (500 MHz, CDCl$_3$) δ 7.72 (d, *J* = 8.2 Hz, 4H), 7.28 (d, *J* = 8.1 Hz, 4H), 4.21 – 4.02 (m, 4H), 3.63 – 3.59 (m, 4H), 3.55 – 3.48 (m, 12H), 2.38 (s, 6H); ^{13}C{^{1}H} NMR (125 MHz, CDCl$_3$) δ 144.8, 132.8, 129.8, 127.8, 70.6, 70.4, 70.3, 69.2, 68.5, 21.5.

N_methylpyrenyl_monoazacrown ether[37,64] (15c5-py, 18c6-py, and 21c7-py) and N-methylanthracenyl monoazacrown ether (15c5-an, 18c6-an, and 21c7-an)[68]:

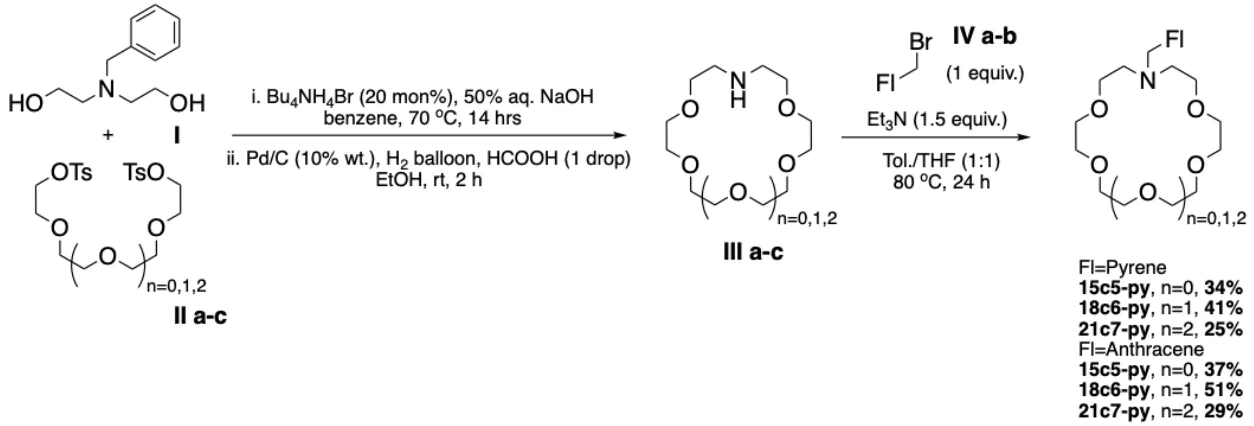

Protected diethanolamine **I** and activated ethylene glycol fragments **IIIa-c** were converted to their respective aza-crown ethers in parallel synthesis under elegant and well described phase transfer conditions in a water/benzene mixture at elevated temperatures. The *N*-benzyl-aza-crown ethers were then deprotected by hydrogenolysis under standard conditions at room temperature and slightly elevated (balloon) pressure. The purified aza-crown ethers were then covalently linked to pyrene (**py**, **IV-b**) or anthracene (**an**, **IV-c**) fluorophores via SN$_2$ reactions under basic and mixed solvent conditions to provide the desired products used in this study in synthetically useful overall yields (29-51% over three steps)[4-6]. N-benzyldiethanoamine (**I**) (195 mg, 1.0 mmol), tetrabutylammonium bromide (0.2 mmol) were mixed in 2 mL 50% NaOH solution. Solution of ethylene glycol bis-p-toluenesulfonate (**IIIa** or **IIIb** or **IIIc**) (1.0 mmol) in 12 mL benzene was then added. The resulting mixture was stirred vigorously at 70 °C for 14 hours. The solution was cooled, diluted with 2 mL benzene and 2 mL water and transferred in separatory funnel. The organic phase was separated, washed with water (3 X 4 mL), dried under anhydrous Magnesium sulfate and concentrated under reduced pressure. The crude product was extracted from the residue by washing with boiling hexanes (3 X 5 mL). The combined hexane wash was evaporated under reduced pressure to obtain clear viscous liquid as crude product. No further purification was carried out and the crude product was directly used for the next step reactions. **N.B**. During the synthesis of **Aza-21-crown-7**, Cesium chloride (3 equiv.) was used as template to facilitate the cyclization reaction in first step. In case of **Aza-18-crown-6**, addition of $BaBr_2$ (as described in literature) as template did not provide improved yield. Therefore, **Aza-15-crown-5** and **Aza-18-crown-6** were synthesized in the absence of templates. A solution of crude N-benzyl diethanolamine **I** (100 mg), 10% Pd/C and 1 drop formic acid in 5 mL ethanol was stirred under hydrogen atmosphere (H2 balloon) at room temperature for 2 hours. The catalyst was filtered under celite and washed with 5 mL ethanol. The filtrate was concentrated in rotary evaporator under reduced pressure to obtain clear liquid aza-crown ether product in crude form which was used directly for the next step. Crude aza-crown ether (50 mg) was added into solution of triethyl amine (1.5 equiv.) in 4 mL toluene and tetrahydrofuran (1:1) and the resulting solution was stirred under Nitrogen for 10 minutes. Bromomethyl pyrene or bromomethyl anthracene (1 equiv. with respect to crude aza- crown ether) was then added in small portion. The mixture was refluxed under stirring for 24 hours at 70 °C under Nitrogen. The reaction mixture was dried under reduced pressure and purified with alumina chromatography using gradient mobile phase from 5:1 hexanes/ethyl acetate to 1:1 hexanes/ethyl acetate to obtain the desired **1-(Pyren-1-ylmethyl)-aza-crown** (**15c5-py, 18c6-py and 21c7-py**) or **1-(Anthracen-9-ylmethyl)-aza-crown** (**15c5-an, 18c6-an and 21c7-an**). Each product was further purified in alumina column using 1% TEA in 1:1 hexanes and ethyl acetate prior to fluorescence studies.

1-(Pyren-1-ylmethyl)-aza-15-crown-5 (15c5-py): Yield 34% over three steps. Pale yellow viscous liquid. ^{1}H NMR (500 MHz, $CDCl_3$) δ 8.57 (d, *J* = 9.2 Hz, 1H), 8.17 (t, *J* = 7.8 Hz, 2H), 8.11 (dd, *J* = 8.4, 5.3 Hz, 2H), 8.06 – 7.98 (m, 4H), 4.37 (s, 2H), 3.74 – 3.60 (m, 16H), 2.94 (t, *J* = 5.9 Hz, 4H); ^{13}C{^{1}H} NMR (125 MHz, $CDCl_3$) δ 131.4, 131.0, 130.7, 128.1, 127.5, 127.1, 127.0, 125.8, 125.0, 125.0, 124.9, 124.5, 124.3, 71.1, 70.7, 70.2, 70.1, 59.3, 54.7. HRMS (ESI) calcd for C27H32NO4 [M+H]+, 434.2326 found, 434.2315.

1-(Pyren-1-ylmethyl)-aza-18-crown-6 (18c6-py): Yield: 41% over three steps. Pale yellow viscous liquid; ^{1}H NMR (500 MHz, CD3CN) δ 8.64 (d, *J* = 9.3 Hz, 1H), 8.27 – 8.20 (m, 2H), 8.20 – 8.14 (m, 2H), 8.12 –

8.01 (m, 4H), 4.31 (s, 2H), 3.61 – 3.48 (m, 20H), 2.81 (t, *J* = 5.7 Hz, 4H); $^{13}C\{^{1}H\}$ NMR (125 MHz, $CDCl_3$) δ 132.1, 131.4, 131.2, 129.8, 128.4, 127.9, 127.5, 126.1, 125.3, 124.6, 123.3, 70.9, 70.8, 70.7, 70.6, 60.0, 56.3. HRMS (ESI) calcd for C29H36NO5 [M+H]+, 478.2588 found, 478.2581.

1-(Pyren-1-ylmethyl)-aza-21-crown-7 (21c7-py): Yield: 25% over three steps; Pale yellow viscous liquid; ^{1}H NMR (500 MHz, $CDCl_3$) δ 8.62 (d, *J* = 9.0 Hz, 1H), 8.21 – 7.97 (m, 9H), 4.39 (s, 2H), 3.74 – 3.56 (m, 24H), 2.91 (t, *J* = 4.8 Hz, 4H); HRMS (ESI) calcd for C31H40NO6 [M+H]+, 522.2850 found, 522.2842.

1-(Anthracen-9-ylmethyl)-aza-15-crown-5 (15c5-an): Yield: 37%% over three steps; yellow viscous liquid; ^{1}H NMR (500 MHz, $CDCl_3$) δ 8.54 (d, *J* = 8.8 Hz, 2H), 8.40 (s, 1H), 7.98 (d, *J* = 8.8 Hz, 2H), 7.54-7.41 (m, 4H), 4.61 (s, 2H), 3.70 – 3.65 (m, 8H), 3.65 – 3.57 (m, 8H), 2.92 (t, *J* = 6.0 Hz, 4H); $^{13}C\{^{1}H\}$ NMR (125 MHz, $CDCl_3$) δ 131.5, 131.4, 130.5, 129.0, 127.5, 125.6, 125.3, 124.8, 71.0, 70.7, 70.1, 70.1, 54.2, 52.6; HRMS (ESI) calcd for C25H31NO5Na [M+Na]+, 432.2145 found, 432.2140.

1-(Anthracen-9-ylmethyl)-aza-18-crown-6 (18c6-an): Yield: 51% over three steps; yellow viscous liquid; ^{1}H NMR (500 MHz, $CDCl_3$) δ 8.56 (d, *J* = 8.9 Hz, 2H), 8.39 (s, 1H), 7.98 (d, *J* = 8.9 Hz, 2H), 7.56 – 7.37 (m, 4H), 4.60 (s, 2H), 3.84 – 3.45 (m, 20H), 2.89 (t, *J* = 5.2 Hz, 4H); $^{13}C\{^{1}H\}$ NMR (125 MHz, CD3CN) δ 132.3, 132.1, 129.7, 128.7, 128.2, 126.5, 126.3, 125.9, 71.3, 71.1, 70.8, 70.4, 54.7, 52.2; HRMS (ESI) calcd for C27H36NO5 [M+H]+, 454.2588 found, 454.2593.

1-(Anthracen-9-ylmethyl)-aza-21-crown-7 (21c7-an): Yield: 29% over three steps; yellow viscous liquid; ^{1}H NMR (300 MHz, $CDCl_3$) δ 8.58 (d, *J* = 8.5 Hz, 2H), 8.40 (s, 1H), 7.99 (d, *J* = 8.5 Hz, 2H), 7.57 – 7.37 (m, 4H), 4.62 (s, 2H), 3.78 – 3.46 (m, 24H), 2.88 (t, *J* = 5.4 Hz, 2H); $^{13}C\{^{1}H\}$ NMR (125 MHz, $CDCl_3$) δ 133.6, 131.5, 130.2, 129.0, 128.5, 125.7, 125.4, 124.9, 71.0, 71.0, 71.0, 70.6, 53.9, 51.8; HRMS (ESI) calcd for C29H40NO6 [M+H]+, 498.2850 found, 498.2849.

B2. Experimental procedure for Chapter 3

2.1. General Procedure

All reagents and solvents were used as purchased unless otherwise stated. The cyanoacrylate matrices were formed by setting commercially available CA Thin Adhesive from Stick Fast. All reagents and solvents were purchased from Sigma Aldrich, Alfa Aesar, and Fisher Scientific. Acetonitrile was of spectrophotometric and HPLC grade from Fisher Scientific. Ultrapure water was purchased from Sigma Aldrich. All metals and non-metal perchlorates were used as purchased. ^{1} H NMR spectra were acquired on 500 MHz JEOL spectrometers and referenced to the internal solvent signals (7.26 ppm in $CDCl_3$ or 1.90 ppm in CD_3CN).^{13}C{1 H} NMR spectra were acquired on 125 MHz spectrometers referenced to the internal solvent signals (central peak 77.00 ppm in $CDCl_3$). NMR data are reported as follows: chemical shift (in ppm, δ), integration, multiplicity (s = singlet, d = doublet, t = triplet, q = quartet, m = multiplet, br = broad), coupling constant (in Hz, J). Thin layer chromatography was performed on silica gel coated aluminum plates (EMD Merck F254, 250μm thickness). 254 nm ultraviolet light and ninhydrin stain (for amine containing molecules) were used to visualize components. Flash column chromatography was performed over Silicycle SilicaflashP60 silica gel (mesh 230-400) or standard grade activated Alumina (mesh 50-300). Melting points were recorded in capillary tubes on a MelTemp II apparatus and were uncorrected. IR spectra were recorded in a Bruker Alpha-P FT-IR Spectrometer by attenuated total reflectance on a diamond sample plate. HRMS data were recorded by time-of-flight mass analysis in the Shimadzu Center for Advanced Analytical Chemistry at UT Arlington. UV-Vis experiments were carried out in a Cary 50 Scan Spectrophotometer from Varian at 25 °C. Fluorescence experiments were performed in a Cary Eclipse Fluorescence Spectrophotometer from Agilent Technologies (Product Number G8800A) at 25 °C. Unless otherwise specified, instrumental set up includes: PMT detector voltage = High, Excitation filter = Auto, Emission filter = Open. All UV-Vis and Fluorescence measurements were taken using Buck Scientific type 18 quartz micro cuvette with 10 mM path length.

2.2. Synthesis

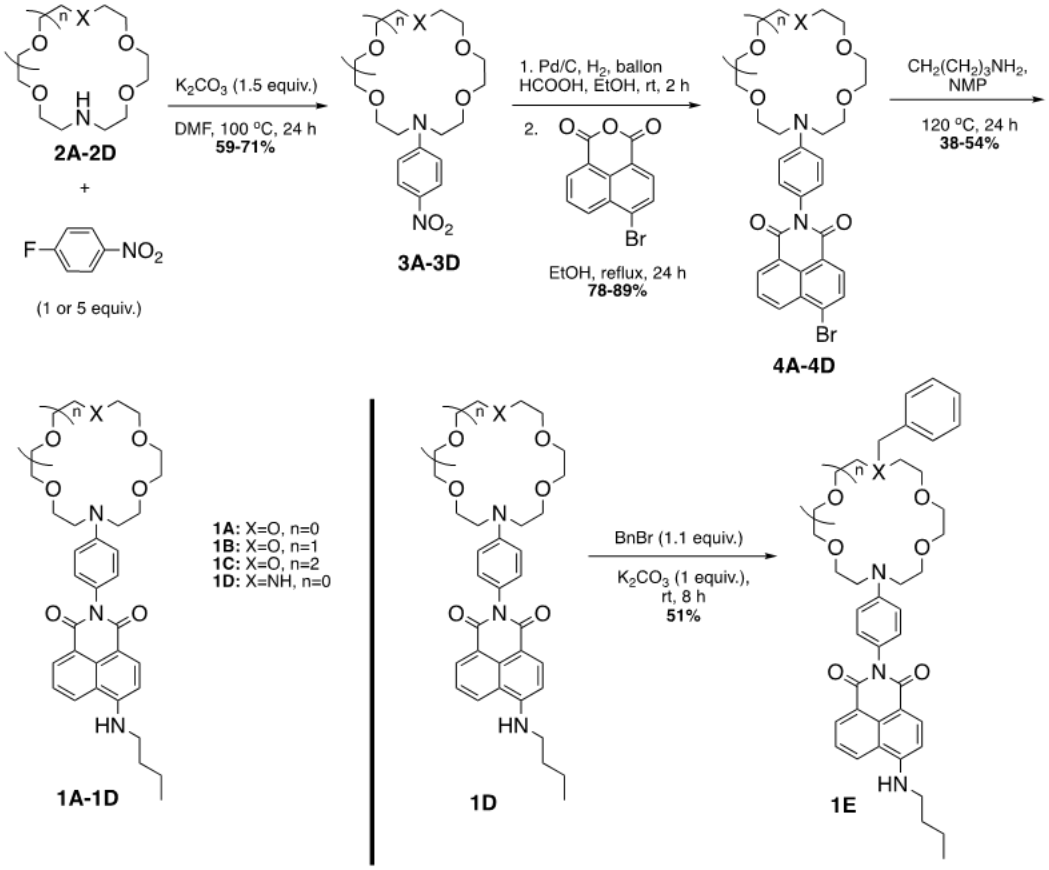

Nitroaniline derivatives (3A-3D):

An oven-dried pressure tube was charged with mono-aza crown ether (**2A** or **2B** or **2C**) or diaza crown ether (**2D**) (1.0 mmol), 4-fluoronitrobenzene (1.0 mmol for diaza-18-crown-6 ether or 5.0 mmol for monoaza crown ethers), potassium carbonate (1.5 mmol) and 5 mL DMF solvent. The mixture was heated in oil bath at 100 °C for 24 hours. After the tube was cooled down to room temperature, the reaction mixture was diluted by adding 5 mL deionized water. The crude product was then extracted with ethyl acetate (EtOAc) (10 mL × 3) in a separatory funnel. The combined organic fraction was washed with saturated brine solution and dried under anhydrous Magnesium sulfate. The crude product was concentrated in rotary evaporator and then purified in column chromatography using 1-5% methanol in dichloromethane. **N.B. 3A** and **3C** were isolated in crude form and were used as such in their respective next step.

4-bromonaphthalimide derivatives (4A, 4B and 4D):

A solution of crude Nitroaniline derivative, **3A** or **3B** or **3D** (1.0 mmol), 10% Pd/C by weight and 1 drop formic acid in 5 mL ethanol was stirred vigorously under hydrogen atmosphere (H_2 balloon) at room temperature until the yellow color disappeared. The mixture was filtered under short pad of celite and washed with excess ethanol. The combined filtrate was immediately concentrated in rotary evaporator under reduced pressure to obtain clear liquid of aniline derivative in crude form which was used directly for the next step. The crude aniline derivative was added into the mixture of 4-bromo-1,8-naphthalimide (0.9 mmol with respect to **3A/3B/3C**) and 4 mL ethanol. The resulting mixture was refluxed under condenser for 24 hours in oil bath. The reaction mixture was first cooled down to room temperature and then kept under ice-cold water, after which the precipitate formed. The crude solid product was filtered and recrystallized using small volume of ethanol. The recrystallized solid was washed with small volume of diethyl ether and dried under high vacuum to obtain 4- bromo-1,8-naphthalimide derivatives **4A** or **4B** or **4D**. **N.B. 4C** was obtained in a crude form and was used as such in the next step.

2-(4-(1,4,7,10-tetraoxa-13-azacyclopentadecan-13-yl)phenyl)-6-bromo-1H-benzo[de]isoquinoline-1,3(2H)-dione (4A): Yellow solid; R*f* = 0.36 (5% methanol in dichloromethane); ^{1}H NMR (500 MHz, CDCl3) δ 8.68 (d, *J* = 7.3 Hz, 1H), 8.59 (d, *J* = 7.8 Hz, 1H), 8.44 (d, *J* = 7.9 Hz, 1H), 8.05 (d, *J* = 7.9 Hz, 1H), 7.86 (dd, *J* = 8.5, 7.3 Hz, 1H), 7.11 (d, *J* = 9.0 Hz, 1H), 6.77 (d, *J* = 9.1 Hz, 1H), 3.83 – 3.76 (m, 4H), 3.72 – 3.59 (m, 16H); ^{13}C{^{1}H} NMR (125 MHz, CDCl3) δ 164.3, 164.2, 147.7, 133.4, 132.4, 131.6, 131.2, 130.8, 130.4, 129.4, 129.0, 128.2, 123.5, 122.8, 122.7, 111.8, 71.4, 70.3, 70.2, 68.5, 52.8; IR (neat, cm-1): 3365, 3063, 2890, 1710, 1661, 1514, 1124; HRMS (ESI) calcd for C28H30BrN2O6 [M+H]+ 569.1282 found, 569.1265.

2-(4-(1,4,7,10,13-pentaoxa-16-azacyclooctadecan-16-yl)phenyl)-6-bromo-1H-benzo[de]isoquinoline-1,3(2H)-dione (4B): Yellow solid; R*f* = 0.17 (5% methanol in dichloromethane); ^{1}H NMR (500 MHz, CDCl3) δ 8.69 (d, *J* = 6.8 Hz, 1H), 8.61 (d, *J* = 8.1 Hz, 1H), 8.45 (d, *J* = 7.8 Hz, 1H), 8.06 (d, *J* = 7.8 Hz, 1H), 7.87 (dd, *J* = 8.1, 7.6 Hz, 1H), 7.10 (d, *J* = 8.8 Hz, 2H), 6.79 (d, *J* = 8.9 Hz, 2H), 3.81 – 3.60 (m, 24H); ^{13}C{^{1}H} NMR (125 MHz, CDCl3) δ 164.3, 164.3, 148.1, 133.5, 132.5, 131.6, 131.2, 130.8, 130.5, 129.4, 129.1, 128.2, 123.6, 122.9, 122.7, 111.9, 70.9, 70.9, 70.8, 68.7, 51.4; IR (neat, cm-1): 3364, 3066, 2894, 1709, 1660, 1515, 1103; HRMS (ESI) calcd for C30H34BrN2O7 [M+H]+ 613.1545 found, 613.1547.

2-(4-(1,4,10,13-tetraoxa-7,16-diazacyclooctadecan-7-yl)phenyl)-6-bromo-1H-benzo[de]isoquinoline-1,3(2H)-dione (4D): Yellow solid; R*f* = 0.04 (5% methanol in dichloromethane); ^{1}H NMR (500 MHz, CDCl3) δ 8.69 (d, *J* = 7.2 Hz, 1H), 8.63 (d, *J* = 7.7 Hz, 1H), 8.45 (d, *J* = 7.8 Hz, 1H), 8.07 (d, *J* = 7.8 Hz, 1H), 7.91 – 7.85 (m, 1H), 7.31 (d, *J* = 5.5 Hz, 1H), 7.15 (d, *J* = 8.8 Hz, 1H), 6.92 (d, *J* = 8.8 Hz, 1H), 3.94 – 3.88 (m, 3H), 3.82 (br, 1H), 3.75 – 3.57 (m, 14H), 3.19 – 3.15 (m, 3H); ^{13}C{^{1}H} NMR (125 MHz, $CDCl_3$) δ 164.2, 164.2, 148.6, 133.7, 132.5, 131.7, 131.3, 130.9, 130.7, 129.6, 129.4, 129.2, 128.3, 123.4, 122.6, 115.5, 70.2, 70.0, 69.5, 66.1, 52.4, 48.3; IR (neat, cm-1): 3364, 3278, 3049, 2893, 1704, 1665, 1514, 1108; HRMS (ESI) calcd for C30H35BrN3O6 [M+H]+, 612.1704 found, 612.1683

4-aminonaphthalimide derivatives (1A-1D):

4-bromonaphthalimide derivative, **4A-4D** (0.2 mmol) was dissolved in 0.25 mL of N-methyl pyrrolidone (NMP) in an oven dried 1.5-dram vial. Then, n-butylamine (0.4 mmol) was added. The vial was heated to 120 ° C for 24 hours, after which the solution color turned to bright yellow. The solution was cooled down to room temperature and was diluted by adding 0.2 mL deionized water. The crude product was extracted using 0.5 mL ethyl acetate (EtOAc) three times. The combined ethyl acetate fraction was dried under anhydrous Magnesium sulfate and concentrated under reduced pressure. The crude product was purified in column chromatography using 1-5% methanol in dichloromethane to obtain desired product.

2-(4-(1,4,7,10-tetraoxa-13-azacyclopentadecan-13-yl)phenyl)6(butylamino)1Hbenzo[de]isoquinoline-1,3(2H)-dione (1A): Yield 48% (54 mg); Yellow solid; Rf = 0.18 (5% methanol in dichloromethane); ^{1}H NMR (500 MHz, CDCl3) δ 8.61 (d, J = 7.2 Hz, 1H), 8.50 (d, J = 8.4 Hz, 1H), 8.11 (d, J = 8.4 Hz, 1H), 7.63 (t, J = 7.8 Hz, 1H), 7.11 (d, J = 8.8 Hz, 2H), 6.77 (d, J = 8.8 Hz, 2H), 6.74 (d, J = 8.5 Hz, 1H), 5.27 (t, J = 4.5 Hz, 1H), 3.74 – 3.63 (m, 20H), 3.46 – 3.39 (m, 2H), 1.86 – 1.77 (m, 2H), 1.59 – 1.50 (m, 2H), 1.03 (t, J = 7.4 Hz, 3H); ^{13}C{^{1}H} NMR (125 MHz, $CDCl_3$) δ 165.4, 164.8, 149.6, 147.7, 134.9, 131.5, 130.3, 129.3, 125.9, 124.8, 123.7, 120.3, 111.9, 110.6, 104.5, 71.0, 70.9, 70.8, 68.7, 51.6, 43.5, 31.2, 20.5, 14.0; IR (neat, cm-1): 3361, 3047, 2824, 2859, 1688, 1643, 1574; HRMS (ESI) calcd for C32H40N3O6 $[M+H]^+$: 562.2917, found: 562.2910.

2-(4-(1,4,7,10,13-pentaoxa-16-azacyclooctadecan-16-yl)phenyl)-6-(butylamino)1Hbenzo[de]isoquinoline-1,3(2H)-dione (1B): Yield 54% (65 mg); Yellow solid; Rf = 0.15 (5% methanol in dichloromethane); ^{1}H NMR (500 MHz, $CDCl_3$) δ 8.61 (d, J = 7.1 Hz, 1H), 8.49 (d, J = 8.3 Hz, 1H), 8.11 (d, J = 8.4 Hz, 1H), 7.63 (t, J = 7.8 Hz, 1H), 7.11 (d, J = 8.6 Hz, 2H), 6.77 (d, J = 8.7 Hz, 2H), 6.74 (d, J = 8.6 Hz, 2H), 5.28 (br, 1H), 3.80 – 3.60 (m, 24H), 3.48 – 3.38 (m, 2H), 1.85 – 1.77 (m, 2H), 1.60 – 1.50 (m, 2H), 1.03 (t, J = 7.3 Hz, 3H); ^{13}C{^{1}H} NMR (125 MHz, $CDCl_3$) δ 165.4, 164.8, 149.6, 147.7, 134.9, 131.5, 130.3, 129.3, 126.0, 124.8, 123.7, 120.3, 112.0, 110.6, 104.5, 70.9, 70.9, 70.8, 68.8, 51.6, 43.5, 31.2, 20.4, 14.0; IR (neat, cm-1): 3366, 3054, 2860, 1688, 1641, 1573; HRMS (ESI) calcd for C34H44N3O7 $[M+H]^+$: 606.3174, found: 606.3158.

2-(4-(1,4,7,10,13,16-hexaoxa-19-azacyclohenicosan-19-yl)phenyl)-6-(butylamino)-1Hbenzo[de]isoquinoline-1,3(2H)-dione (1C): Yield 41% (53 mg); Yellow solid; Rf = 0.25 (5% methanol in dichloromethane); ^{1}H NMR (500 MHz, $CDCl_3$) δ 8.61 (d, J = 7.1 Hz, 1H), 8.49 (d, J = 8.4 Hz, 1H), 8.10 (d, J = 8.1 Hz, 1H), 7.67 – 7.60 (m, 1H), 7.10 (d, J = 8.8 Hz, 2H), 6.80 – 6.71 (m, 3H), 5.23 (t, J = 4.7 Hz, 1H), 3.76 – 3.59 (m, 28H), 3.45 – 3.38 (m, 2H), 1.85 – 1.76 (m, 2H), 1.55 – 1.51 (m, 2H), 1.03 (t, J = 7.4 Hz, 3H); IR (neat, cm-1): 3369, 3048, 2908, 2866, 1688, 1647, 1575; HRMS (ESI) calcd for C36H48N3O8 $[M+H]^+$:650.3436, found: 650.3418.

2-(4-(1,4,10,13-tetraoxa-7,16-diazacyclooctadecan-7-yl)phenyl)-6-(butylamino)-1Hbenzo[de]isoquinoline-1,3(2H)-dione (1D): Yield 38% (46 mg); Yellow solid, Rf = 0.025 (5% methanol in dichloromethane); ^{1}H NMR (500 MHz, CDCl3) δ 8.61 (d, J = 7.0 Hz, 1H), 8.49 (d, J = 8.2 Hz, 1H), 8.11 (d, J = 8.2 Hz, 1H), 7.63 (t, J = 7.7 Hz, 1H), 7.11 (d, J = 7.4 Hz, 2H), 6.79 (d, J = 7.3 Hz, 2H), 6.74 (d, J = 8.3 Hz, 1H), 5.29 (br, 1H), 3.79 – 3.53 (m, 20H), 3.47 – 3.38 (m, 2H), 2.97 – 2.82 (m, 4H), 1.84 – 1.77 (m, 2H), 1.58 – 1.49 (m, 2H), 1.03 (t, J = 7.3 Hz, 3H); ^{13}C{^{1}H} NMR (125 MHz, CDCl3) δ 165.3, 164.8, 149.6, 147.8, 134.9, 131.5, 130.3, 129.7, 129.3, 126.0, 124.7, 123.6, 122.3, 120.3, 112.6, 104.4, 70.6, 70.4, 68.9, 51.3, 48.9, 43.5, 31.1, 20.4, 13.9; IR (neat, cm-1): 3364, 3022, 2922, 1688, 1641, 1577; HRMS (ESI) calcd for C34H45N4O6 $[M+H]^+$: 605.3334, found: 605.3327.

2-(4-(16-benzyl-1,4,10,13-tetraoxa-7,16-diazacyclooctadecan-7-yl)phenyl)-6-(butylamino)-1Hbenzo[de]isoquinoline-1,3(2H)-dione (1E): 4-aminonaphthalimide derivative **1D** (0.05 mmol, 30.2 mg), potassium carbonate (0.05 mmol, 6.9 mg) and 0.5 mL acetonitrile were added into a 1.5-dram vial. Benzyl bromide (0.055 mmol, 6.5 µL) was then added dropwise under Nitrogen atmosphere. The resulting mixture was then stirred at room temperature for 8 hours. The reaction mixture was filtered and the solid was washed with acetonitrile. The filtrate solution containing crude product was concentrated under S5 reduced pressure and was purified in column chromatography using 2% methanol in dichloromethane to obtain desired product. Yield 51% (18 mg); yellow solid, Rf = 0.075 (5% methanol in dichloromethane); ^{1}H NMR (500 MHz, CDCl3) δ 8.62 (d, J = 7.3 Hz, 1H), 8.50 (d, J = 8.3 Hz, 1H), 8.11 (d, J = 8.4 Hz, 1H), 7.67 – 7.60 (m, 1H), 7.36 – 7.28 (m, 5H), 7.11 (d, J = 8.7 Hz, 2H), 6.77 (d, J = 8.9 Hz, 2H), 6.75 (d, J = 8.5 Hz, 1H), 5.25 (t, J = 5.1 Hz, 1H), 3.76 – 3.59 (m, 22H), 3.47 – 3.39 (m, 2H), 2.90 – 2.79 (m, 4H), 1.86 – 1.76 (m, 2H), 1.60 – 1.52 (m, 3H), 1.04 (t, J = 7.4 Hz, 4H); ^{13}C{^{1}H} NMR (125 MHz, CDCl3) δ 165.0, 164.8, 149.62, 147.7, 134.9, 131.5, 130.3, 129.3, 129.0, 128.3, 125.9, 124.8, 120.3, 113.8, 113.5, 112.0, 111.91, 110.6, 104.5, 71.1, 70.7, 68.9, 53.8, 51.6, 43.5, 31.2, 20.5, 14.0; IR (neat, cm-1): 3357, 3070, 2924, 1702, 1643, 1575; HRMS (ESI) calcd for C41H51N4O6 $[M+H]^+$: 695.3803, found: 695.3789.

B3. Experimental Procedure for Chapter 4

3.1 General Procedure

All reagents and solvents were used as purchased unless otherwise stated. The cyanoacrylate matrices were formed by setting commercially available CA Thin Adhesive from Stick Fast. All reagents and solvents were purchased from Sigma Aldrich, Alfa Aesar, and Fisher Scientific. Acetonitrile was of spectrophotometric and HPLC grade from Fisher Scientific. Ultrapure water was purchased from Sigma Aldrich. All metals and non-metal perchlorates were used as purchased. ^{1} H NMR spectra were acquired on 500 MHz JEOL spectrometers and referenced to the internal solvent signals (7.26 ppm in $CDCl_3$ or 1.90 ppm in CD_3CN).^{13}C{1 H} NMR spectra were acquired on 125 MHz spectrometers referenced to the internal solvent signals (central peak 77.00 ppm in $CDCl_3$). NMR data are reported as follows: chemical shift (in ppm, δ), integration, multiplicity (s = singlet, d = doublet, t = triplet, q = quartet, m = multiplet, br = broad), coupling constant (in Hz, J). Thin layer chromatography was performed on silica gel coated aluminum plates (EMD Merck F254, 250μm thickness). 254 nm ultraviolet light and ninhydrin stain (for amine containing molecules) were used to visualize components. Flash column chromatography was performed over Silicycle SilicaflashP60 silica gel (mesh 230-400) or standard grade activated Alumina (mesh 50-300). Melting points were recorded in capillary tubes on a MelTemp II apparatus and were uncorrected. IR spectra were recorded in a Bruker Alpha-P FT-IR Spectrometer by attenuated total reflectance on a diamond sample plate. HRMS data were recorded by time-of-flight mass analysis in the Shimadzu Center for Advanced Analytical Chemistry at UT Arlington. UV-Vis experiments were carried out in a Cary 50 Scan Spectrophotometer from Varian at 25 °C. Fluorescence experiments were performed in a Cary Eclipse Fluorescence Spectrophotometer from Agilent Technologies (Product Number G8800A) at 25 °C. Unless otherwise specified, instrumental set up includes: PMT detector voltage = High, Excitation filter = Auto, Emission filter = Open. All UV-Vis and Fluorescence measurements were taken using Buck Scientific type 18 quartz micro cuvette with 10 mM path length.

Biological Studies: Cytotoxicity of **6B** was evaluated by performing MTT assay. HeLa cells were seeded in 96-well plates (10,000 cells/plate) and incubated for 24 h for the completion of cell attachment. The old media was removed, and cells were treated with the various doses of the **6B** (0-100 μM). The **6B** (10 mM in acetonitrile) was directly diluted in the cell media so that the final concentration of acetonitrile in the cell media is always less than 1%. Following the 24 h incubation, the old media was replaced with fresh media containing 0.5 mg/mL MTT assay and incubated for 3 h. After that, formazan crystals were dissolved with DMSO, and the absorption of the purple-colored formazan solutions was scanned at 540 nm with a microplate reader (Multiskan). The cell viability was expressed as the percentage of the control group.

3.2 Synthesis

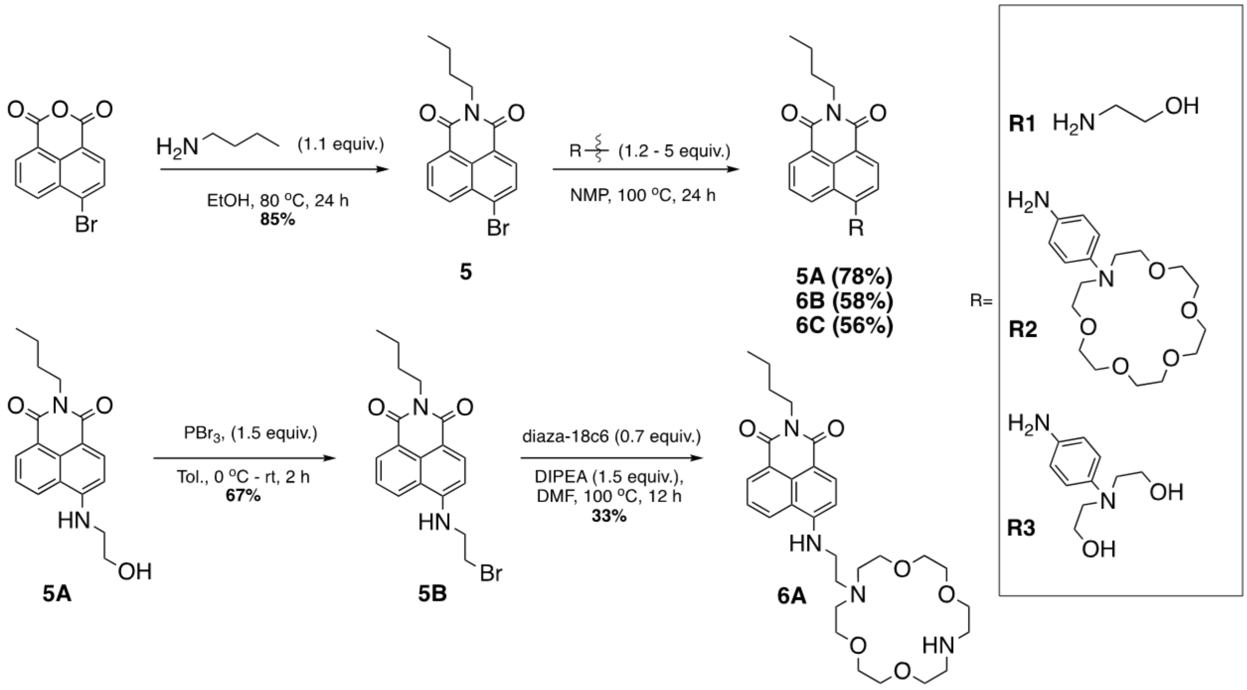

***6-bromo-2-butyl-1H-benzo[de]isoquinoline-1,3(2H)-dione* (5):** 4-bromo-1,8-napthalic anhydride (1.4 g, 5 mmol) dissolved in ethanol (10 mL) with butylamine (5.6 mmol, 550 µL) added dropwise to the reaction and left under refluxed at 80 °C for 24 h. Reaction mixture was first cooled to rt, and after cooled in ice bathed followed by filtration. The residue collected was washed with cold ethanol and dried. Yield 85% (1.4 g, 5 mmol); Brown solid; ^{1}H NMR (500 MHz, $CDCl_3$) δ 8.63 (t, *J* = 6.6 Hz, 1H), 8.53 (d, *J* = 8.0 Hz, 1H), 8.38 (d, *J* = 7.5 Hz, 1H), 8.01 (d, *J* = 7.5 Hz, 1H), 7.82 (t, *J* = 7.4 Hz, 1H), 4.16 (t, 5.6 Hz, 2H), 1.79 – 1.67 (m, 2H), 1.51 – 1.36 (m, 2H), 0.97 (t, *J* = 6.7 Hz, 3H); ^{13}C{^{1}H} NMR (125 MHz, $CDCl_3$) δ 163.7, 163.7, 133.3, 132.1, 131.3, 131.1, 130.7, 130.2, 129.0, 128.1, 123.2, 122.4, 40.5, 30.2, 20.5, 13.9.

Butylamine naphtalemide derivatives (5A, 6B, 6C).

Compound **5** (0.2 mmol) was dissolved in 0.25 mL of N-methyl pyrrolidone (NMP) in an oven-dried 1.5-dram vial. Then, nucleophile **B, C** (0.4 mmol) or **ethanolamine** (1 mmol) was added. The vial was heated to 120 ° C for 24 hours, after which the solution color turned to bright yellow. The solution was cooled down to room temperature and was diluted by adding 0.2 mL deionized water. The crude product was extracted using 0.5 mL ethyl acetate (EtOAc) three times. The combined ethyl acetate fraction was dried under anhydrous Magnesium sulfate and concentrated under reduced pressure. The crude product was purified in column chromatography using 1-5% methanol in dichloromethane to obtain desired product.

2-butyl-6-((2-hydroxyethyl)amino)-1H-benzo[de]isoquinoline-1,3(2H)-dione **(5A):** Yield 78% (312 mg, 1 mmol scale of 5), yellow solid. ^{1}H NMR (500 MHz, $CDCl_3$) δ 8.55 (d, *J* = 7.2 Hz, 1H), 8.42 (d, *J* = 8.4 Hz, 1H), 8.11 (d, *J* = 8.3 Hz, 1H), 7.60 (dd, *J* = 7.9 Hz, 1H), 6.71 (d, *J* = 8.4 Hz, 1H), 5.72 (br, 1H), 4.21 – 4.11 (m, 2H), 4.06 (t, 5.7 Hz, 2H), 3.61 – 3.52 (m, 2H), 1.77 – 1.66 (m, 2H), 1.50 – 1.38 (m, 2H), 0.97 (t, *J* = 7.4 Hz, 3H); ^{13}C{^{1}H} NMR (125 MHz, $CDCl_3$) δ 164.7, 164.3, 149.4, 134.4, 131.3, 129.8, 126.0, 124.9, 123.2, 120.5, 110.9, 104.6, 60.6, 45.4, 40.1, 30.4, 20.5, 14.0.

6-((4-(1,4,7,10,13-pentaoxa-16-azacyclooctadecan-16-yl)phenyl)amino)-2-butyl-1H-benzo[de]isoquinoline-1,3(2H)-dione **(6B):** Yield 58% (35 mg, 0.1 mmol scale of 5), red solid, mp. 220 °C (decomp.).; ^{1}H NMR (500 MHz, $CDCl_3$) δ 8.61 (d, *J* = 7.2 Hz, 1H), 8.36 (d, *J* = 8.4 Hz, 1H), 8.25 (d, *J* = 8.3 Hz, 1H), 7.67 (dd, *J* = 7.8 Hz, 1H), 7.16 (d, *J* = 8.7 Hz, 2H), 6.95 (d, *J* = 8.4 Hz, 1H), 6.76 (d, *J* = 8.2 Hz, 2H), 4.21 – 4.13 (m, 2H), 3.75 (t, *J* = 5.8 Hz, 4H), 3.71 – 3.62 (m, 20H), 1.77 – 1.66 (m, 2H), 1.48 – 1.38 (m, 2H), 0.96 (t, *J* = 7.4 Hz, 3H); ^{13}C{^{1}H} NMR (125 MHz, $CDCl_3$) δ 164.8, 164.2, 149.0, 146.6, 134.0, 131.4, 130.1, 126.6, 126.1, 125.1, 123.4, 120.7, 112.6, 111.5, 107.1, 70.9, 70.8, 68.8, 51.6, 40.1, 30.4, 20.5, 14.0; IR (neat, cm-1): 3337, 2970, 2861, 1683, 1641, 1576; HRMS (ESI) calcd for C34H44N3O7 $[M+H]^+$, 606.74 found, 606.3165.

***6-((4-(bis(2-hydroxyethyl)amino)phenyl)amino)-2-butyl-1H-benzo[de]isoquinoline-1,3(2H)-dione* (6C):** Yield 56% (25 mg, 0.1 mmmol scale of 5), red solid, m.p.164 °C (decomp.). ^{1}H NMR (500 MHz, CD_3CN) δ 8.52 (dd, *J* = 7.3 Hz, 1H), 8.49 (d, *J* = 8.5 Hz, 1H), 8.24 (d, *J* = 8.5 Hz, 1H), 7.70 (dd, *J* = 8.2, 7.4 Hz, 1H), 7.69 (br, 1H), 7.19 (d, *J* = 8.9 Hz, 2H), 6.90 (d, *J* = 8.5 Hz, 1H), 6.83 (d, *J* = 9.0 Hz, 2H), 4.13 – 4.01 (m, 2H), 3.78 – 3.65 (m, 4H), 3.54 (t, *J* = 5.7 Hz, 4H), 3.32 (br, 2H), 1.70 – 1.57 (m, 2H), 1.47 – 1.34 (m, 2H), 0.96 (t, *J* = 7.4 Hz, 3H); ^{13}C{^{1}H} NMR (125 MHz, $CDCl_3$) δ 164.8, 164.2, 148.8, 146.4, 134.0, 131.4, 130.1, 128.5, 126.4, 126.2, 125.1, 123.3, 120.8, 113.7, 111.7, 107.2, 60.8, 55.5, 40.1, 30.4, 20.5, 14.0; MP 87-91C IR (neat, cm-1): 3319, 2971, 2925, 1674, 1634, 1576; HRMS (ESI) calcd for C26H30N3O4 $[M+H]^+$, 448.54 found, 488.2230.

***6-((2-(1,4,10,13-tetraoxa-7,16-diazacyclooctadecan-7-yl)ethyl)amino)-2-butyl-1H-benzo[de]isoquinoline-1,3(2H)-dione* (6A):** Compound **5A** (50 mg, 0.16 mmol) was dissolved in 2 mL freshly distilled toluene and the reaction vial was sealed properly with rubber septum. PBr_3 (23 μL, 0.24 mmol) was added dropwise over 5 minutes at 0 °C and the reaction mixture was stirred for 1 hour at 0 °C and was slowly brought to room temperature. 2 mL saturated Na_2CO_3 was added slowly. The crude product was extracted using 5 mL dichloromethane twice. The combined organic phase was dried under anhydrous Na_2SO_4 and concentrated to obtain yellow solid. The crude solid was recrystallized in methanol giving crude product dark yellow color in 67% yield (51 mg). Compaund **5B** and diaza-crown ether were dissolved in DMF with addition of DIPEA (1.5 equiv.) and left at 100 °C for 12 h. Reaction mixture was extracted using water and DCM, dried with Sodium sulfate, and concentrated under reduced pressure. Chromatography column was performed using 1-5% MeOH in DCM. Yield 33% (18.4 mg, 0.1 mmol scale of 5B); Yellow solid. Mp. 148-155 ˚C; ^{1}H NMR (500 MHz, $CDCl_3$) δ 8.54 (d, *J* = 7.2 Hz, 1H), 8.46 (d, *J* = 8.2 Hz, 1H), 8.41 (d, *J* = 8.4 Hz, 1H), 7.60 (t, *J* = 7.8 Hz, 1H), 7.08 (br, 1H), 6.62 (d, *J* = 8.5 Hz, 1H), 4.14 (t, 2H), 3.73 (s, 4H), 3.55 (d, *J* = 19.0 Hz, 12H), 3.42 (d, *J* = 4.6 Hz, 2H), 2.92 (s, 2H), 2.88 (t, 2H), 2.83 – 2.77 (m, 4H), 1.69 (dt, *J* = 15.2, 7.7 Hz, 2H), 1.47 – 1.38 (m, 2H), 0.95 (t, *J* = 7.4 Hz, 3H); ^{13}C{^{1}H} NMR (125 MHz, $CDCl_3$) δ 164.9, 164.3, 150.2, 134.6, 131.1, 130.1, 128.1, 124.6, 122.8, 120.8, 109.7, 104.0, 70.3, 70.19, 69.4, 55.7, 52.5, 49.1, 41.6, 40.0, 30.4, 20.5, 14.0; IR (neat, cm-1): 3355, 2960, 2858, 1683, 1643, 1581; HRMS (ESI) calcd for C30H44N3O7 $[M+H]^+$, 558.70 found, 558.330.

B4. Experimental procedure for Chapter 5

4.1. General procedure

Fluorescence spectra were recorded using a Cary Eclipse Fluorescence Spectrophotometer from Agilent Technologies (Product Number G8800A) at room temperature (25 °C). Instrumental set up: PMT detector voltage-High, Excitation filter-Auto, Emission filter-Open, Excitation slit width-5 nm, Emission slit width-10 nm, scan control-medium, spectral range 420 nm to 700 nm. Cary eclipse solid sample holder was used for glass substrate imaging. AFM imaging was done using Cyper ES version 16, with SHR300 and Multy75GD-G probes. Analyzation was performed by using Gwyddion promgram, on height retrace images at polynomial degree 1 method. ^{1}H NMR spectra were recorded on 300 MHz or 500 MHz spectrometers and referenced to the residual solvent signals (7.26 ppm $CHCl_3$ in $CDCl_3$ or 3.33 ppm CHD_2OD in CD_3OD). $^{13}C\{^1H\}$ NMR spectra were recorded on 75 MHz or 125 MHz spectrometers referenced to the residual solvent signal (77.0 ppm in $CDCl_3$ or 45.0 ppm in CD_3OD). NMR data are reported as follows: chemical shift (δ, ppm), integration (H), multiplicity (s-singlet, d-doublet, t-triplet, q-quartet, m-multiplet, br-broad), coupling constant (*J,* Hz). High resolution mass spectrometry (HRMS) data were recorded using a Shimadzu TOF spectrometer in the Shimadzu Center for Advanced Analytical Chemistry at UT Arlington. Fourier transform- infrared (FT-IR) spectra were recorded using a Bruker Alpha-P FT-IR spectrophotometer by attenuated total reflectance on a diamond sample plate. Thin layer chromatography was performed on silica gel-coated aluminum plates (EMD Merck F254, 250 μm thickness). Flash chromatography was performed over Silicycle Silicafash P60 silica gel (mesh 230 – 400) or standard grade activated Alumina (mesh 50–300). Melting points were recorded in capillary tubes on a Mel-Temp II apparatus and were uncorrected. Commercially available chemicals were used without further purification unless specified. Toluene was freshly dried and distilled prior to use. Ultrapure water from a Water Pro BT water station was used for piranha cleaning the substrate. The glass substrate used is Ted Pella, micro cover glass, 22*30 mm, No. 1 (0.13 - 0.16 mm) thick.

4.2. Synthesis

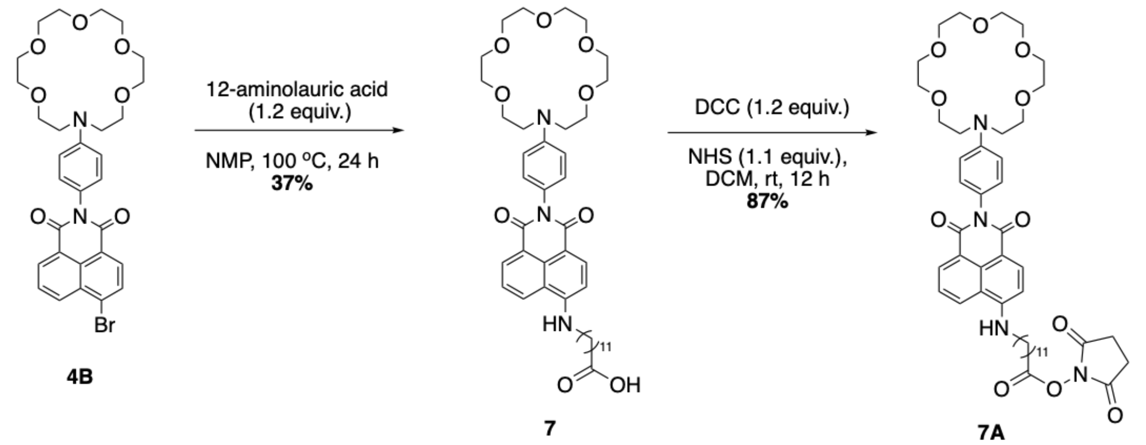

Scheme 5. Synthesis of the 18c6-Napthalimide-NHS molecule **7A**.

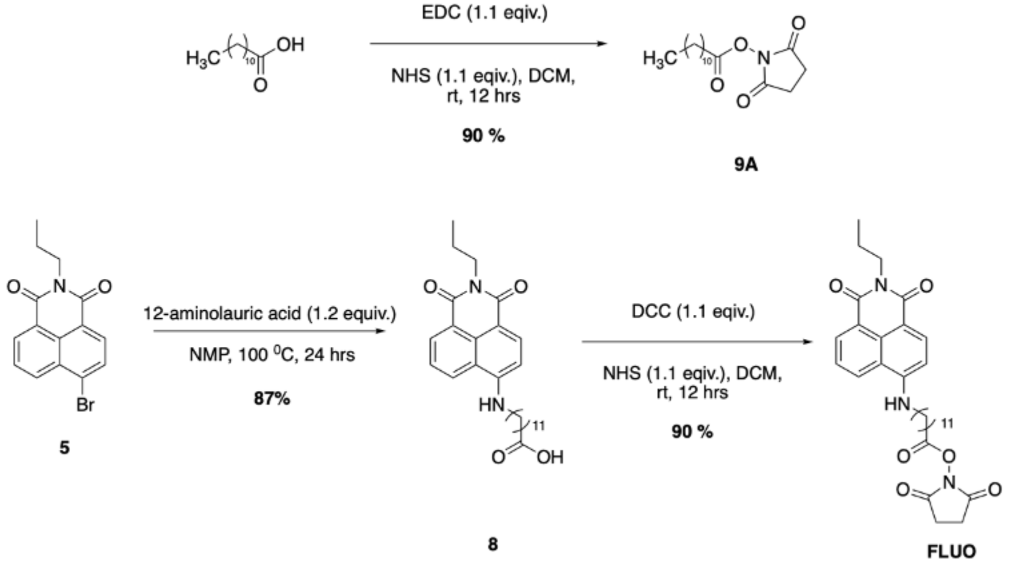

Scheme 5.1. Synthesis of the **FLUO** molecule and spacer **9A**.

4-bromonaphthalimide derivative (**4B** or **5**) (0.2 mmol) was dissolved in 0.25 mL of N-methyl pyrrolidone (NMP) in an oven-dried 1.5-dram vial. Then, n-butylamine (0.4 mmol) was added. The vial was heated to 120 °C for 24 hours, after which the solution color turned bright yellow. The solution was cooled down to room temperature and was diluted by adding 0.2 mL of deionized water. The crude product was extracted using 0.5 mL ethyl acetate (EtOAc) three times. The combined ethyl acetate fraction was dried under anhydrous Magnesium sulfate and concentrated under reduced pressure. The crude product was obtained as one fluorescent spot on TLC under the longwave UV lamp and was used to proceed to the next step. The dodecanoic acid derivative was dissolved in 1 mL dichloromethane (DCM). Reactants N-hydroxysuccinimide (NHS), and dicyclohexylacarbodiimide (DCC) (1.05 equiv. each) were dissolved in 1 ml DCM and added dropwise to the starting material solution. The resulting mixture was then stirred at room temperature for 12 hours. The reaction mixture was extracted using water and brine. The filtrate solution containing crude product was concentrated under S5 reduced pressure and was purified in column chromatography 1-5% methanol in dichloromethane to obtain a product.

2,5-dioxopyrrolidin-1-yl12-((2-(4-(1,4,7,10,13-pentaoxa-16-azacyclooctadecan-16-yl)phenyl)-1,3 dioxo-2,3-dihydro-1H-benzo[de]isoquinolin-6-yl)amino)dodecanoate (7A): Yellow solid (16.5mg, 87%). Mp. 55 °C (decomp.). IR (neat, cm^{-1}): 3325, 2922, 2852, 1813, 1783, 1740, 1708, 1665, 1609, 1587. ^{1}H NMR (500 MHz, $CDCl_3$) δ 8.67 (dt, *J* = 10.7, 5.4 Hz, 1H), 8.61 – 8.55 (m, 1H), 8.46 – 8.40 (m, 1H), 8.04 (d, *J* = 7.9 Hz, 1H), 7.88 – 7.82 (m, 1H), 7.14 – 7.04 (m, 2H), 6.78 (dd, *J* = 9.2, 2.9 Hz, 2H), 3.91 – 3.36 (m, 24H), 2.82 (d, *J* = 5.7 Hz, 4H), 2.59 (td, *J* = 7.6, 1.7 Hz, 2H), 1.77 – 1.64 (m, 2H), 1.50 (p, *J* = 7.4 Hz, 2H), 1.47–1.08 (m,16H). $^{13}C\{^1H\}$ NMR (126 MHz, $CDCl_3$) δ 169.35, 168.79, 164.30, 164.28, 161.30, 148.04, 133.48, 132.46, 131.62, 131.23, 130.81, 130.47, 129.23, 129.07, 128.23, 123.55, 122.94, 122.68, 115.35, 112.59, 111.92, 71.29. 70.97, 70.92, 70.85, 70.69, 70.41, 70.08, 68.68, 51.61, 38.26, 34.01, 31.00, 30.02, 29.58, 29.49, 29.43, 29.31, 29.25, 29.08, 28.93, 28.79, 26.88, 25.68, 25.03, 24.62. IR (neat, cm-1): 3366, 3054, 2860, 1707, 1664, 1641, 1573; HRMS (ESI) calcd for C46H60N4O11 $[M+H]^+$, predicted: 844.43, found: 845.4431.

2,5-dioxopyrrolidin-1-yl12-((2-butyl-1,3-dioxo-2,3-dihydro-1H-benzo[de]isoqinolin-6-yl)amino)dodecanoate (Fluo): Yellow solid. Yield 90% (65.8 mg, 0.2 mmol), m.p. 67 °C (decomp.). ^{1}H NMR (500 MHz, $CDCl_3$) δ 8.59 – 8.53 (m, 1H), 8.45 (d, *J* = 8.4 Hz, 1H), 8.07 (dd, *J* = 8.4, 1.0 Hz, 1H), 7.60 (td, *J* = 7.8, 2.1 Hz, 1H), 6.70 (dd, *J* = 8.5, 2.3 Hz, 1H), 4.16 – 4.10 (m, 3H), 3.38 (t, *J* = 7.2 Hz, 3H), 2.82 (d, *J* = 5.3 Hz, 4H), 2.59 (t, *J* = 7.5 Hz, 2H). $^{13}C\{^1H\}$ NMR (126 MHz, $CDCl_3$) δ 169.30, 168.79, 164.81, 149.49, 134.57, 131.16, 129.90, 125.79, 124.74, 123.35, 120.24, 110.39, 104.42, 60.50, 43.82, 40.07, 33.89, 31.68, 31.01, 30.41, 29.63, 28.87, 28.79, 27.22, 25.68, 24.97, 24.61, 22.74, 20.53, 14.21, 13.98. IR (neat, cm^{-1}): 3326, 2925, 2850, 1814, 1784, 1736, 1683, 1630. HRMS (ESI) calcd for C32H41N3O6 $[M+H]^+$, predicted: 563.68, found: 564.2835.

2,5-dioxopyrrolidin-1-yl dodecanoate (9A)[154]: White crystals. Yield 50% (40 mg, 0.2 mmol). ^1H NMR (500 MHz, $CDCl_3$) δ 2.82 (d, *J* = 6.1 Hz, 4H), 2.59 (t, *J* = 7.5 Hz, 2H), 1.73 (p, *J* = 7.5 Hz, 2H), 1.60 (d, *J* = 37.0 Hz, 2H), 1.45 – 1.34 (m, 2H), 1.34 – 1.14 (m, 14H), 0.87 (t, *J* = 6.9 Hz, 3H). $^{13}C\{^1H\}$ NMR (126 MHz, $CDCl_3$) δ 169.28 (2 X C=O), 168.80, 31.91, 31.03, 29.39, 29.29, 29.17, 28.87, 28.74, 28.01, 25.68 (2 XCH_2), 24.66, 22.74, 14.19.

Appendix C ^{1}H and ^{13}C NMR Spectra

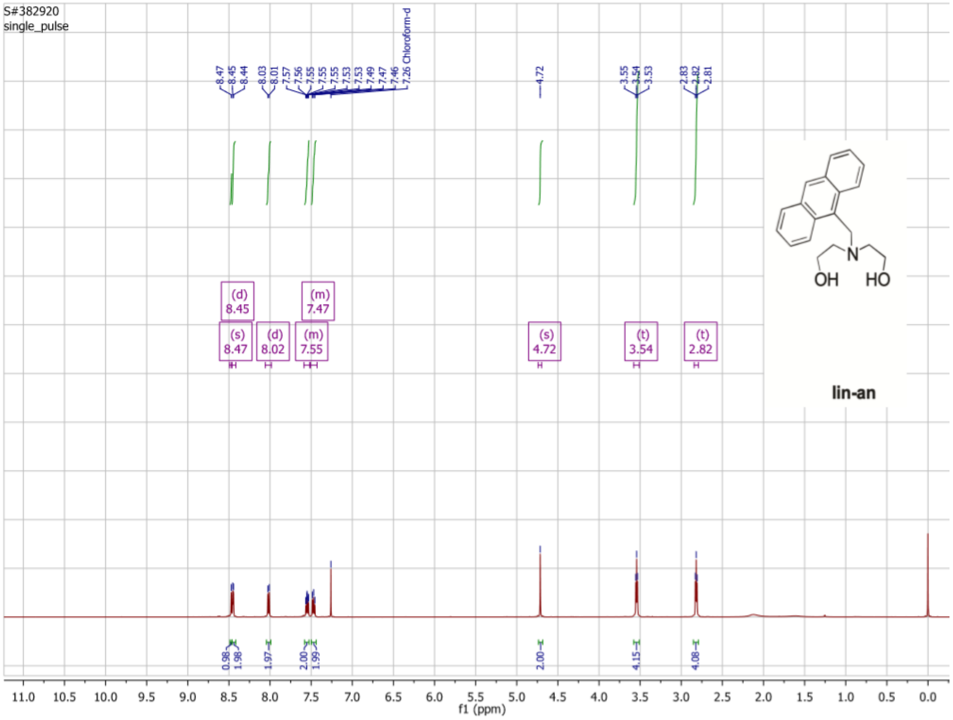

^{1}H NMR ($CDCl_3$, 500 MHz)

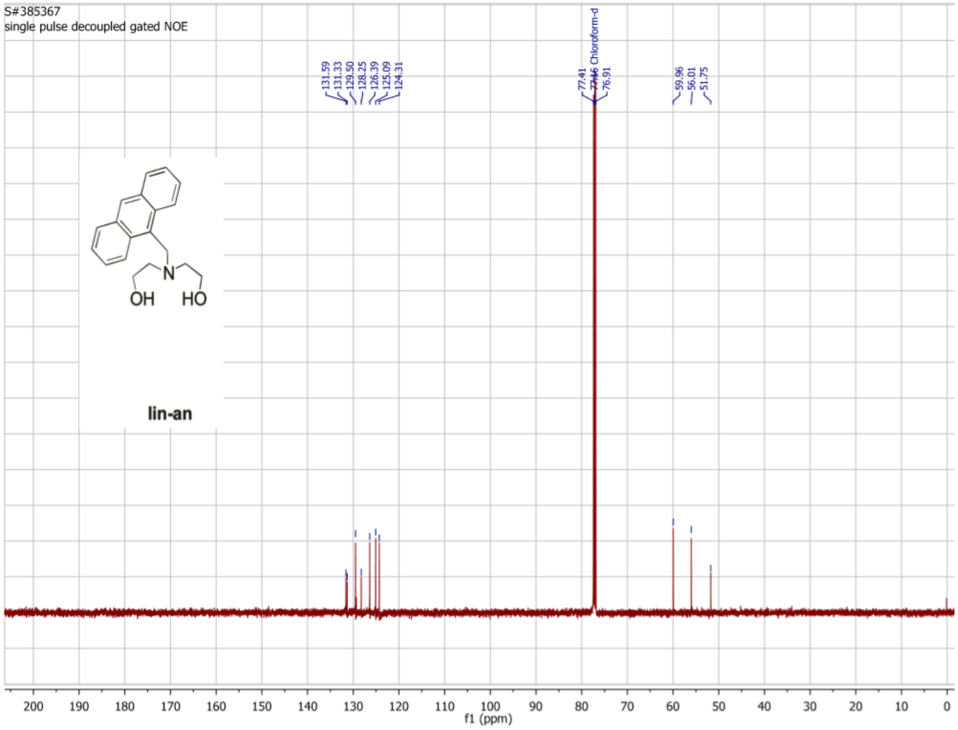

^{13}C NMR ($CDCl_3$, 125 MHz)

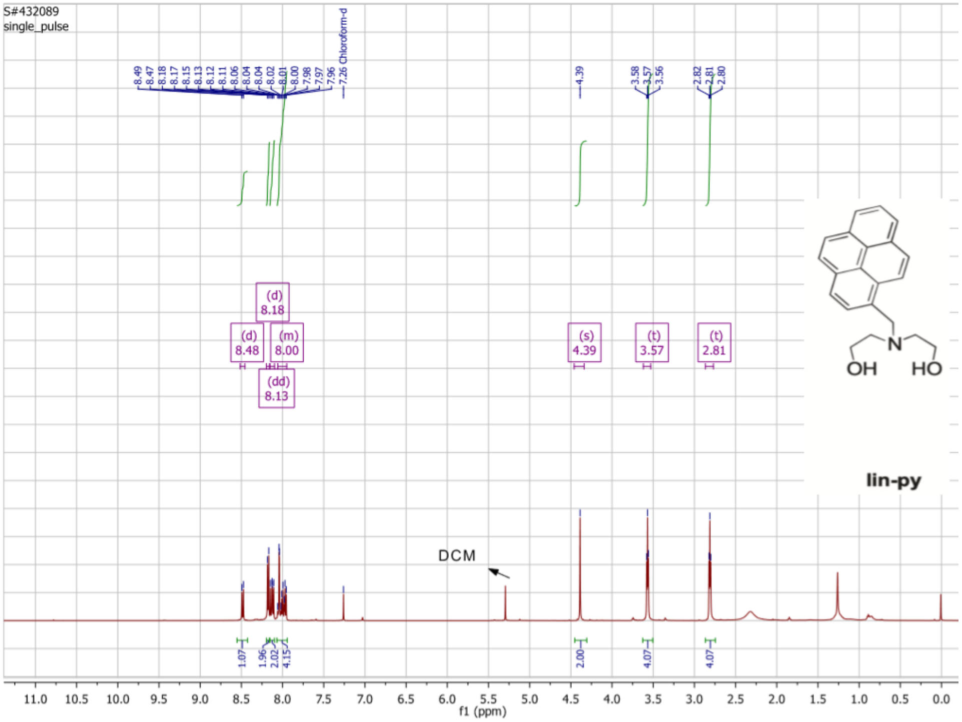

^1H NMR ($CDCl_3$, 500 MHz)

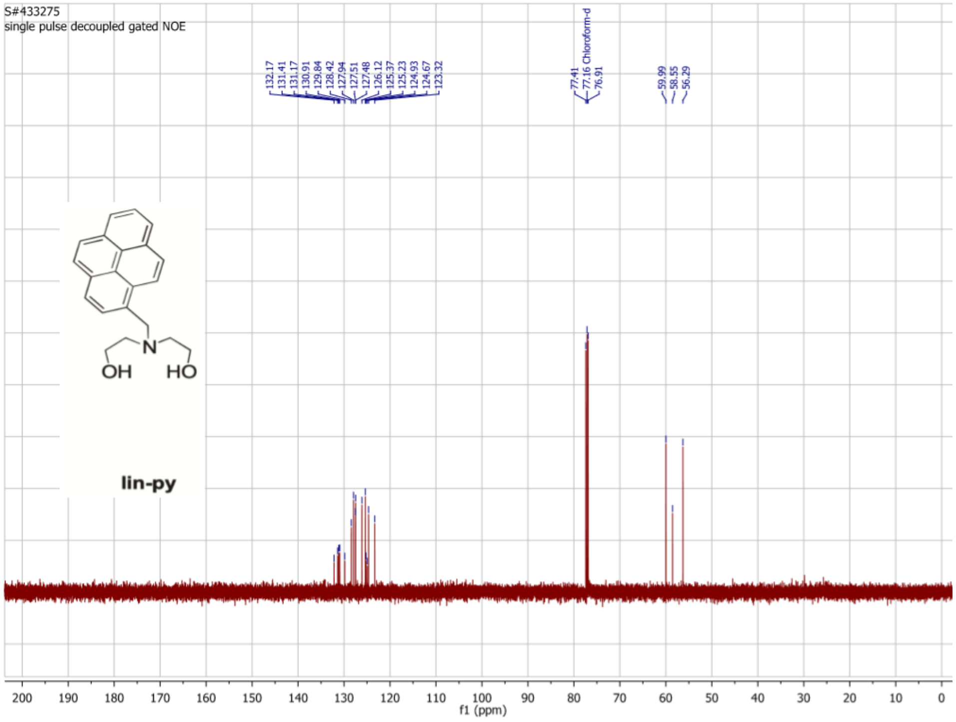

^{13}C NMR ($CDCl_3$, 125 MHz)

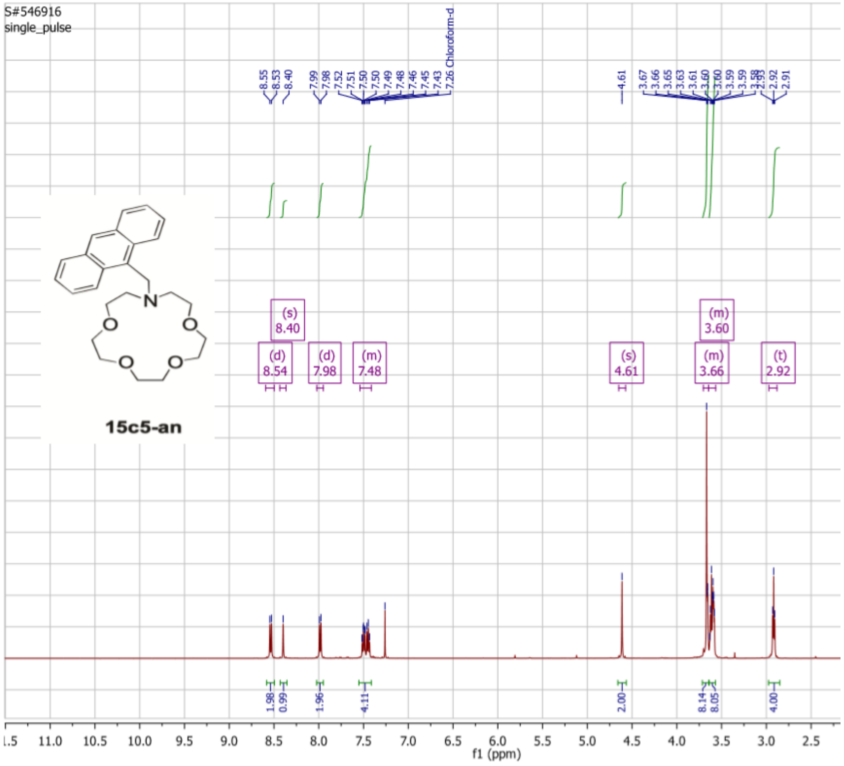

^{1}H NMR (CDCl$_3$, 500 MHz)

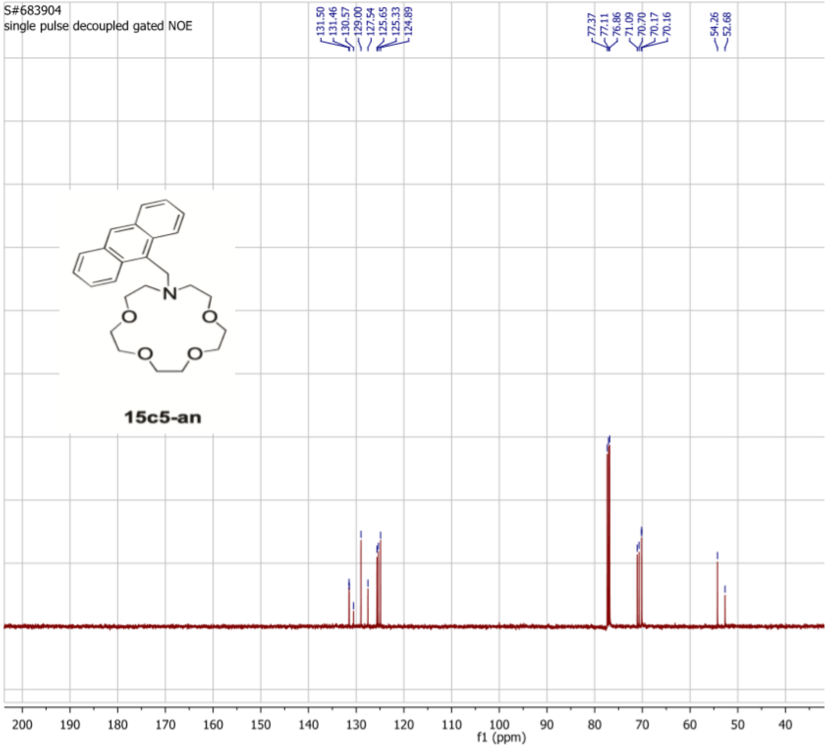

^{13}C NMR (CDCl$_3$, 125 MHz)

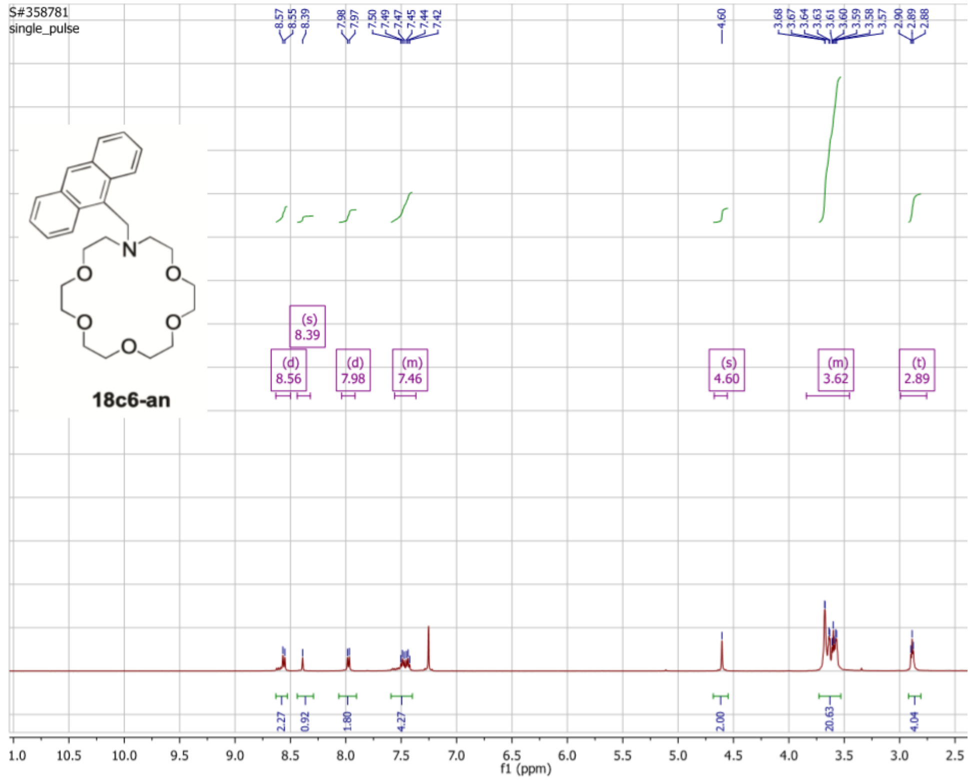

^{1}H NMR (CDCl$_3$, 500 MHz)

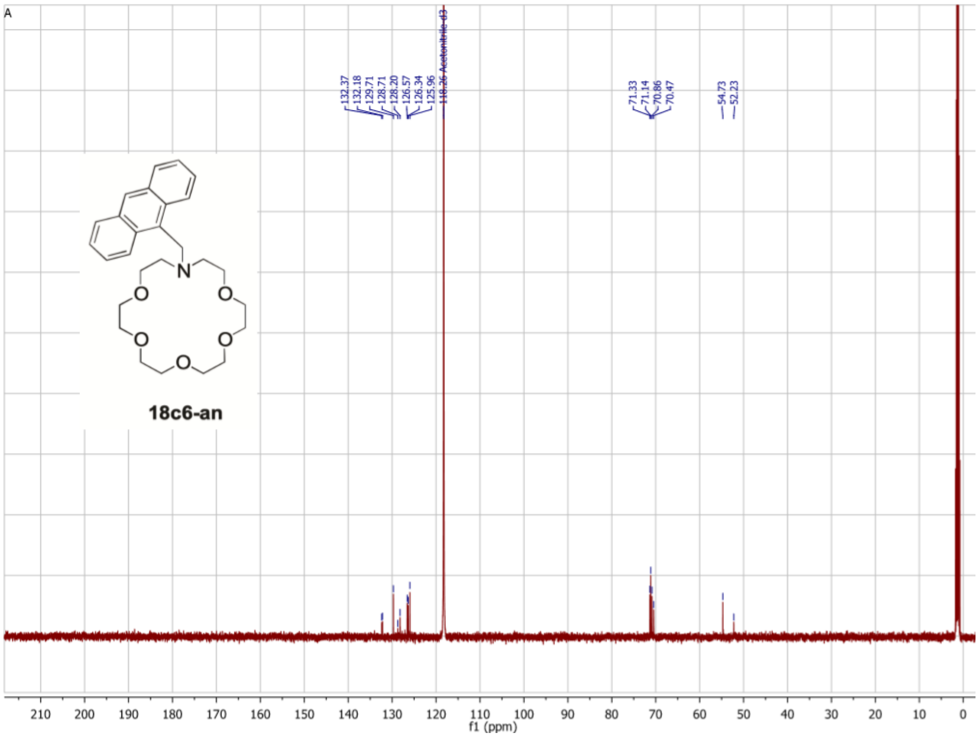

^{13}C NMR (CDCl$_3$, 125 MHz)

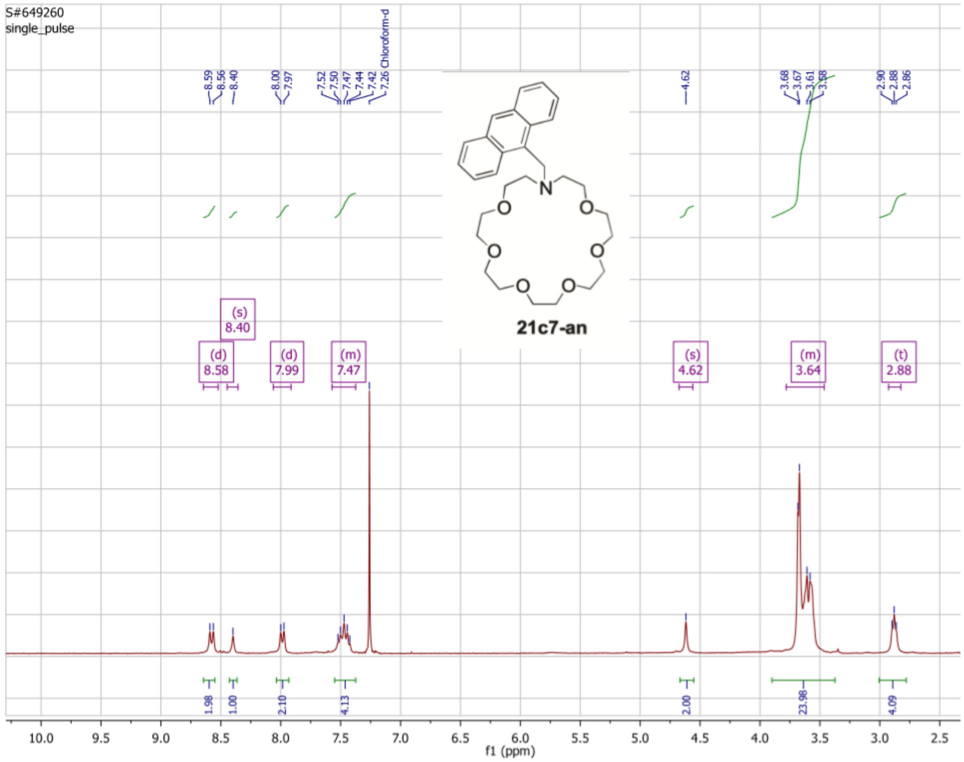

^{1}H NMR (CDCl$_3$, 500 MHz)

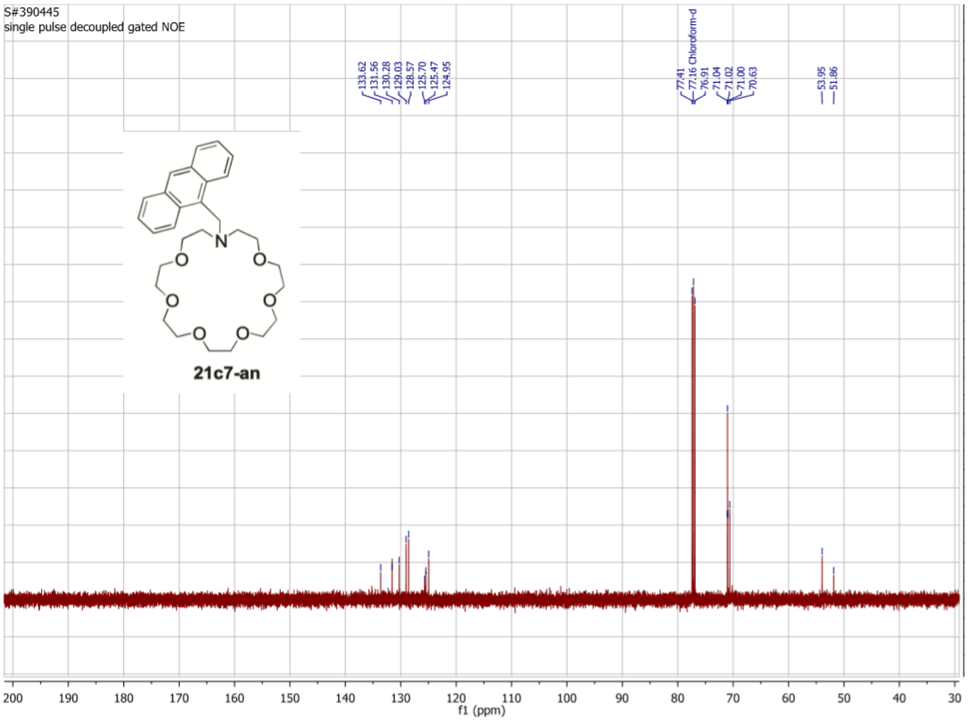

^{13}C NMR (CDCl$_3$, 125 MHz)

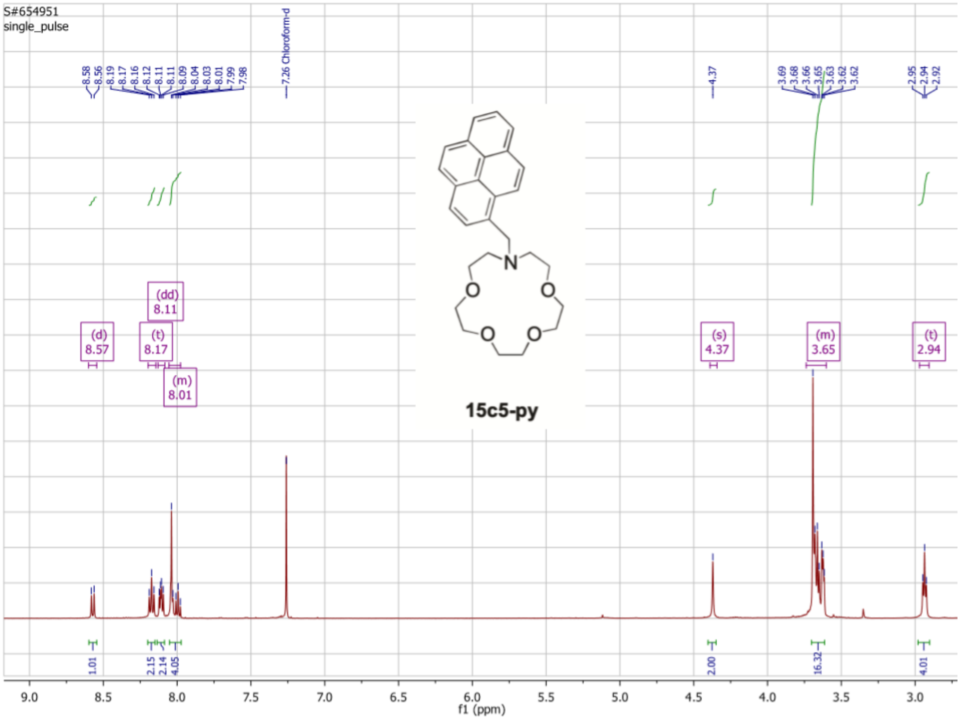

^{1}H NMR (CDCl$_3$, 500 MHz)

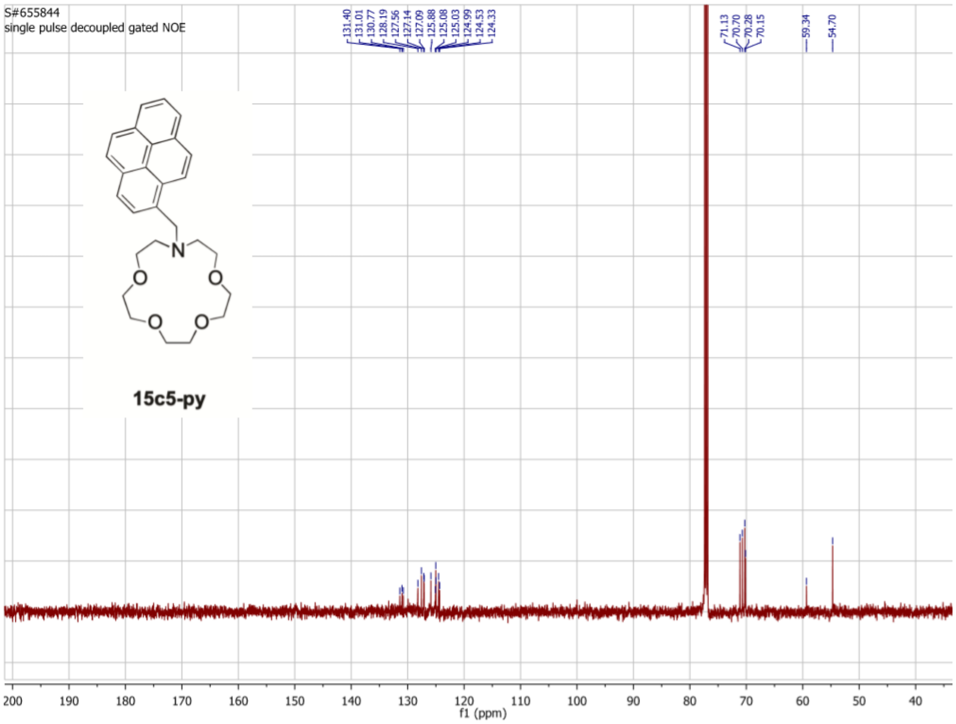

^{13}C NMR (CDCl$_3$, 125 MHz)

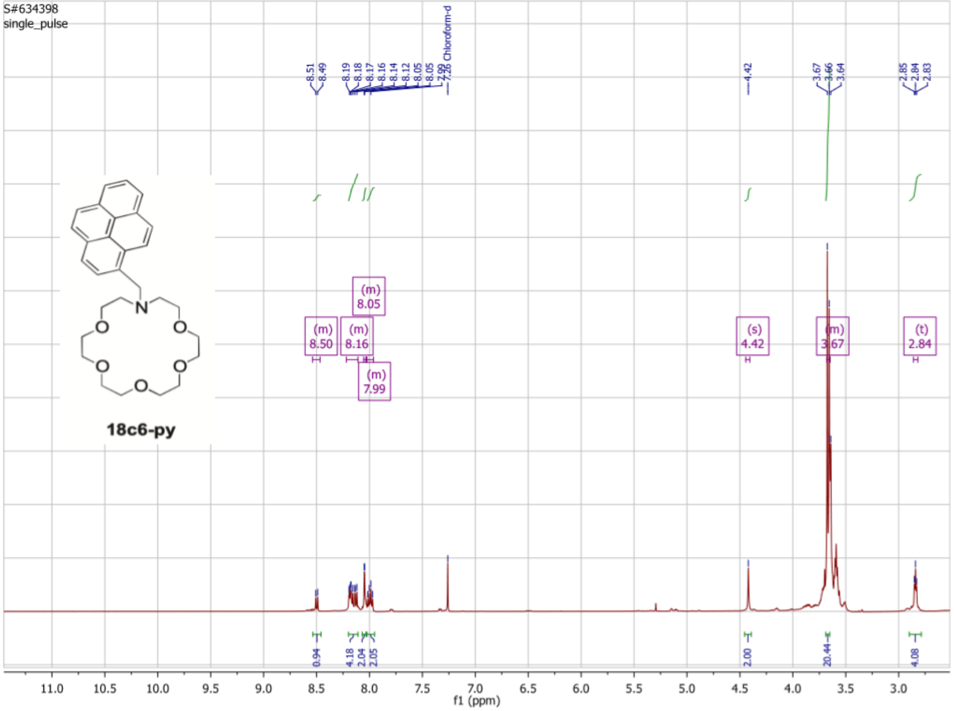

^{1}H NMR (CDCl$_3$, 500 MHz)

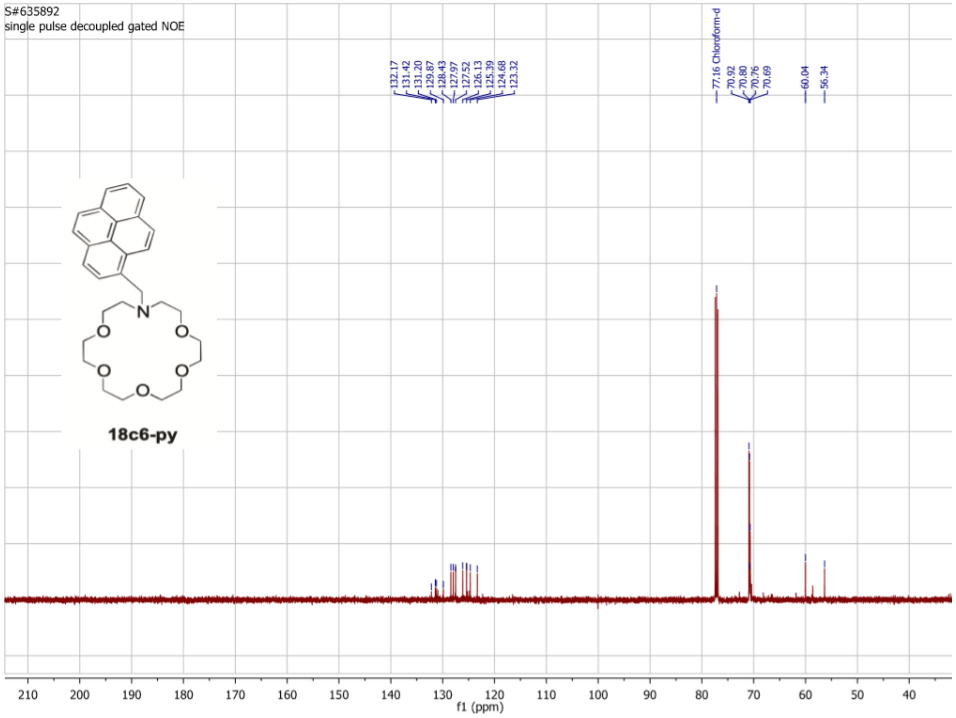

^{13}C NMR (CDCl$_3$, 125 MHz)

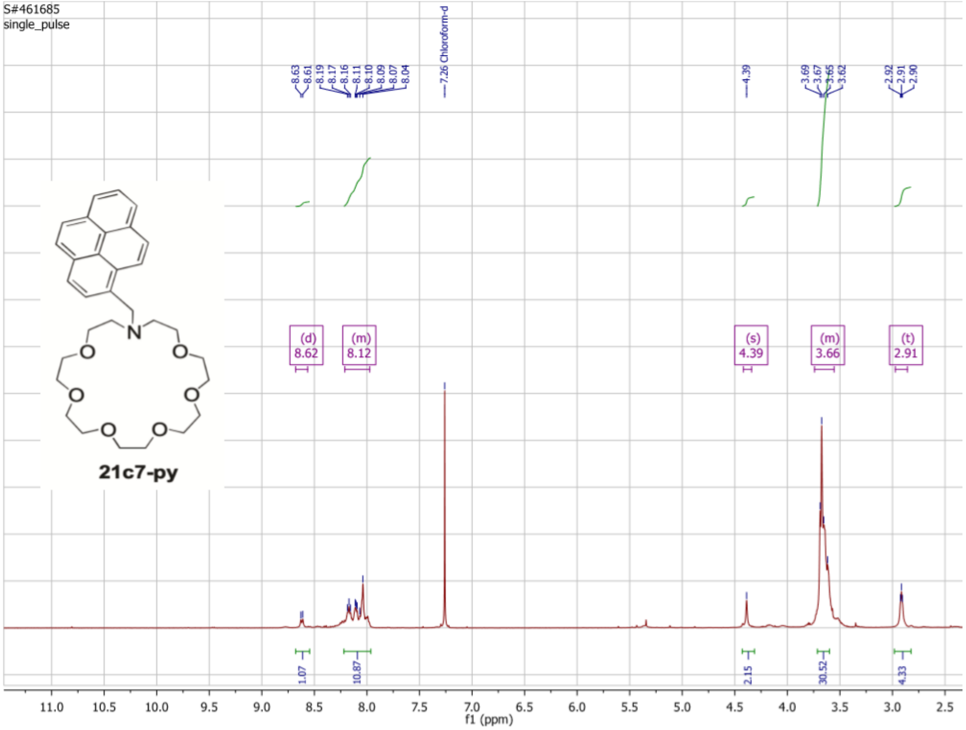

^{1}H NMR ($CDCl_3$, 500 MHz)

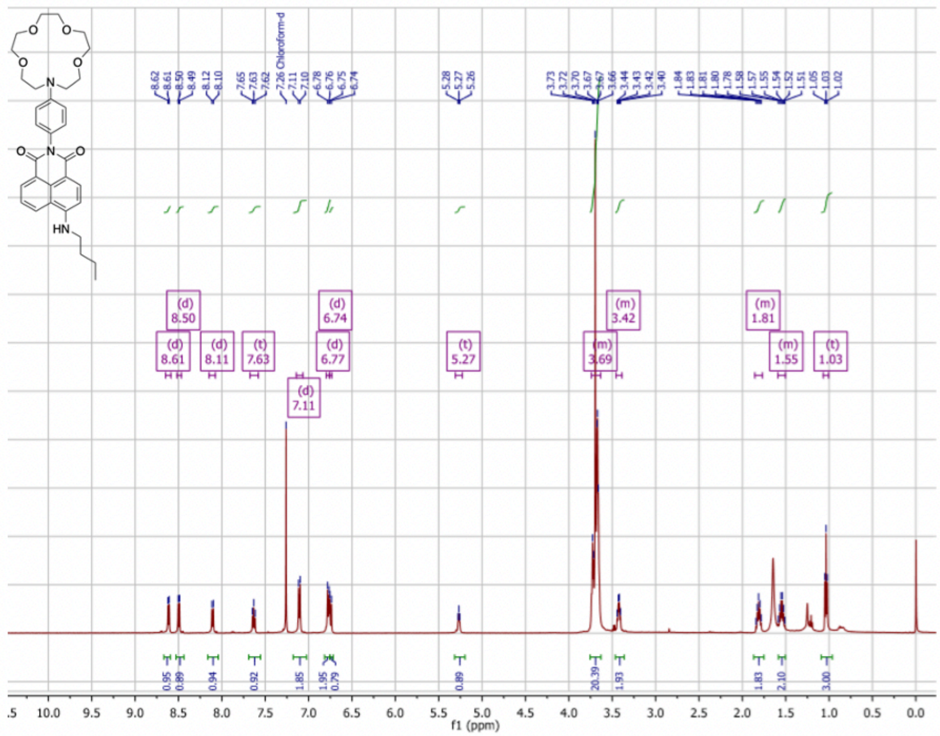

1A ^{1}H NMR (CDCl$_3$, 500 MHz)

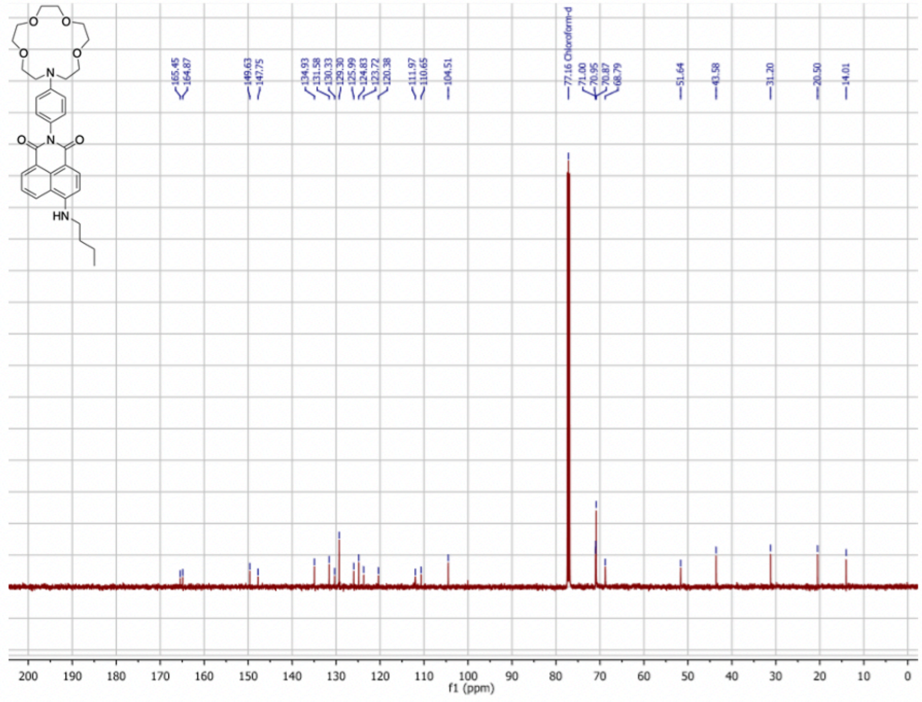

1A ^{13}C NMR (CDCl$_3$, 125 MHz)

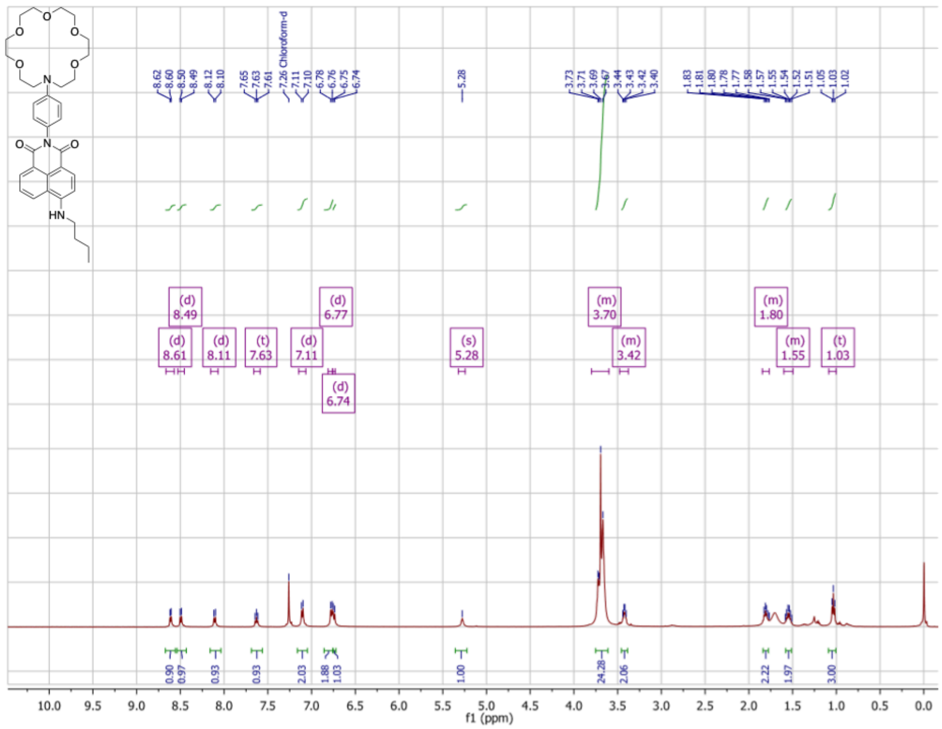

1B ^{1}H NMR (CDCl$_3$, 500 MHz)

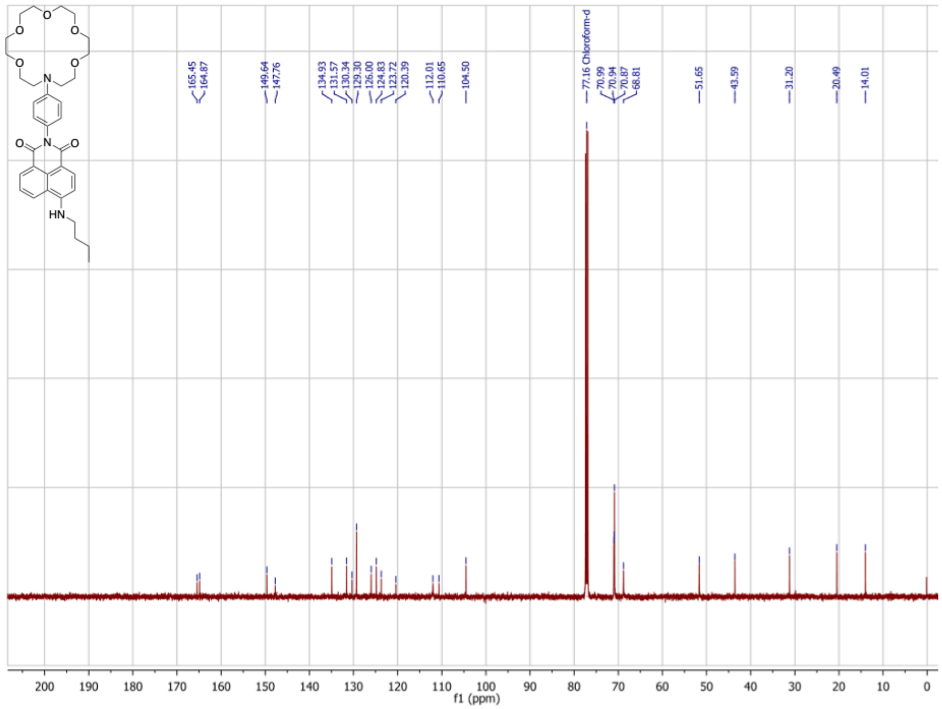

1B ^{13}C NMR (CDCl$_3$, 125 MHz)

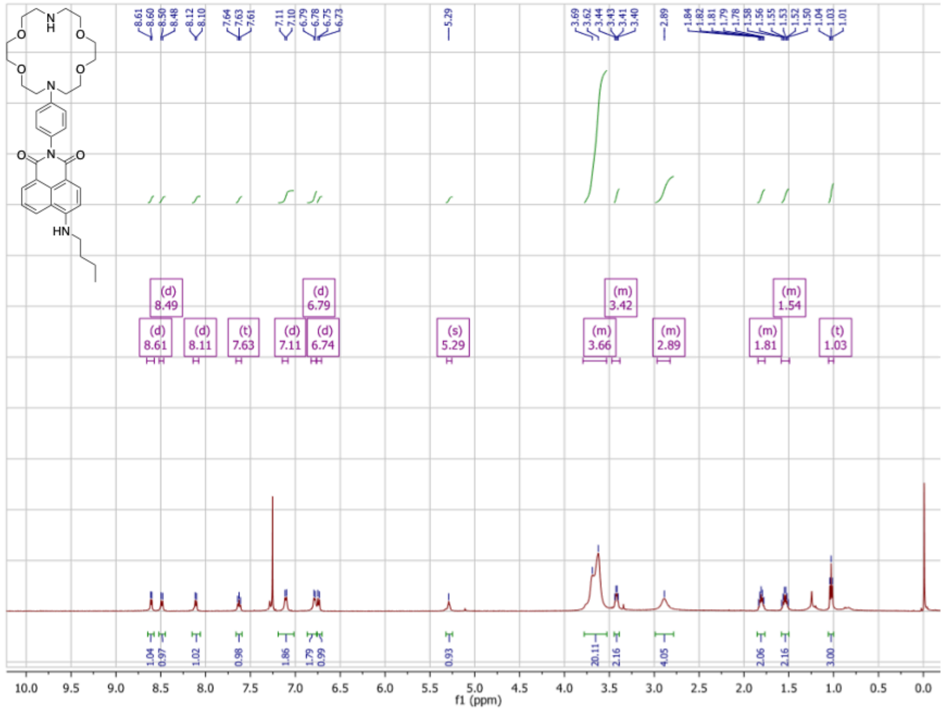

1D ^{1}H NMR ($CDCl_3$, 500 MHz)

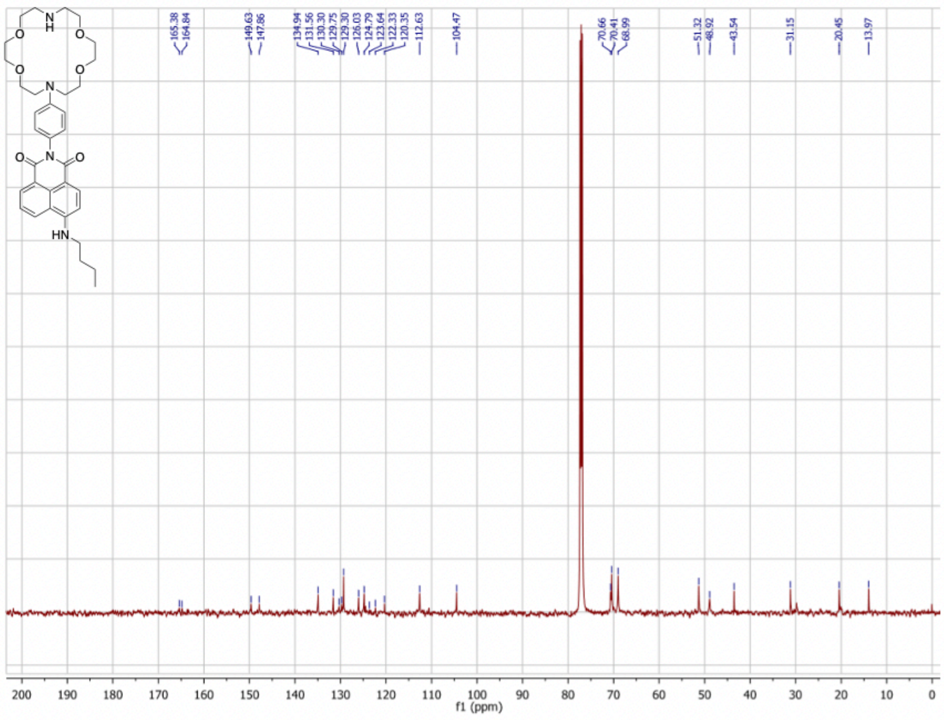

1D ^{13}C NMR ($CDCl_3$, 125 MHz)

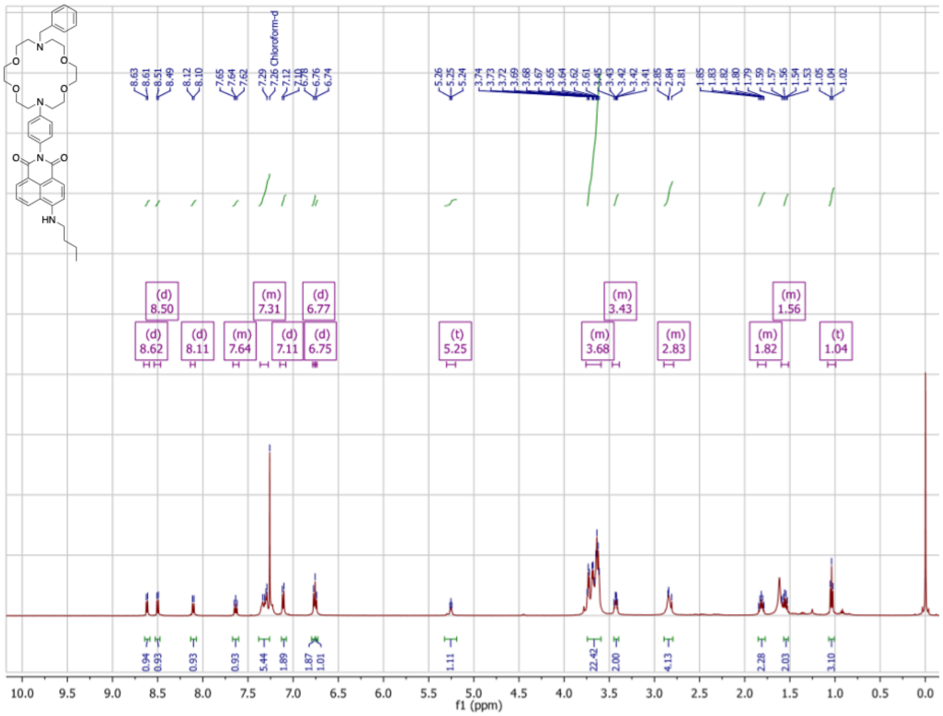

1E ^{1}H NMR (CDCl$_3$, 500 MHz)

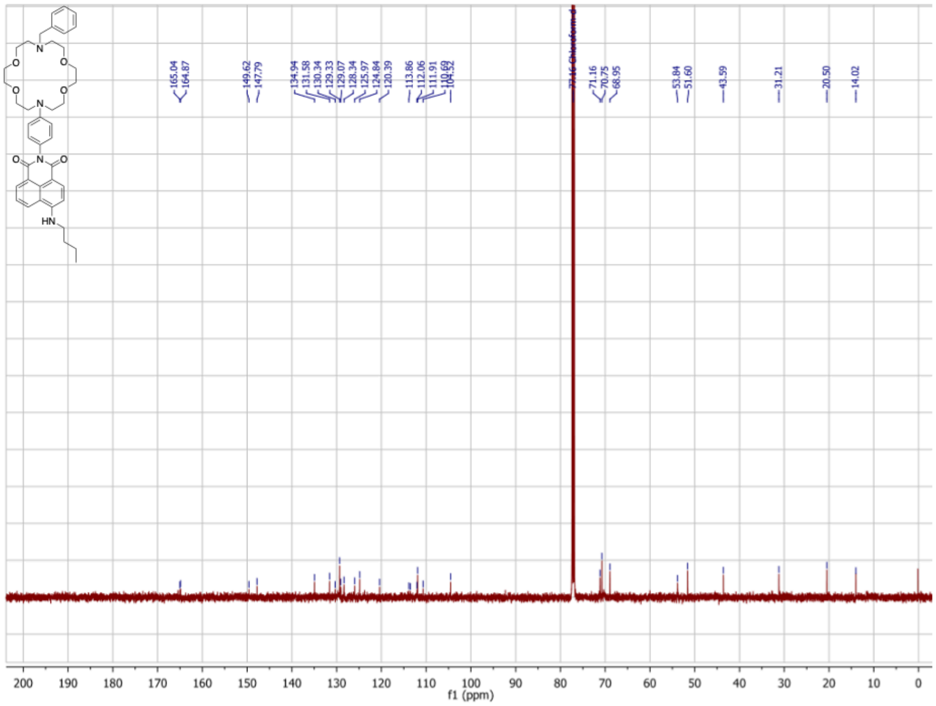

1E ^{13}C NMR (CDCl$_3$, 125 MHz)

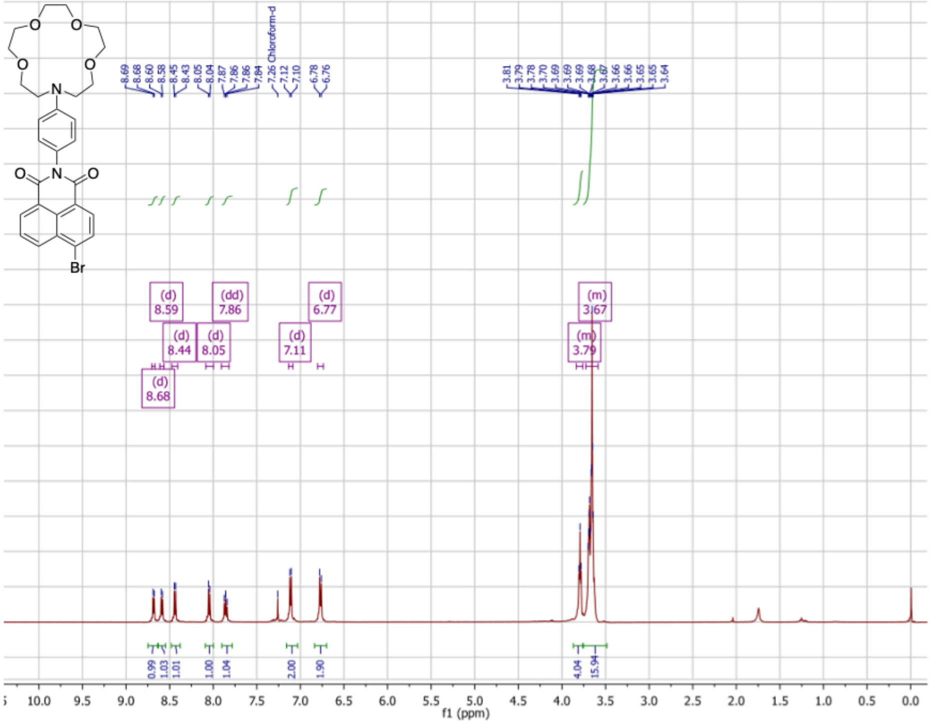

4A ^{1}H NMR (CDCl$_3$, 500 MHz)

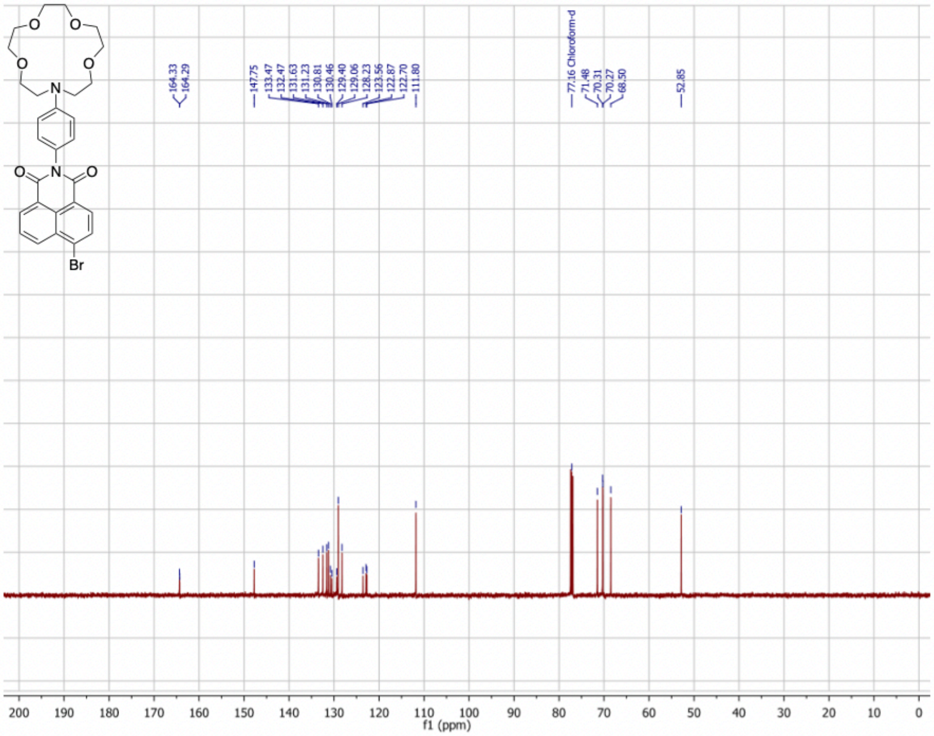

4A ^{13}C NMR (CDCl$_3$, 125 MHz)

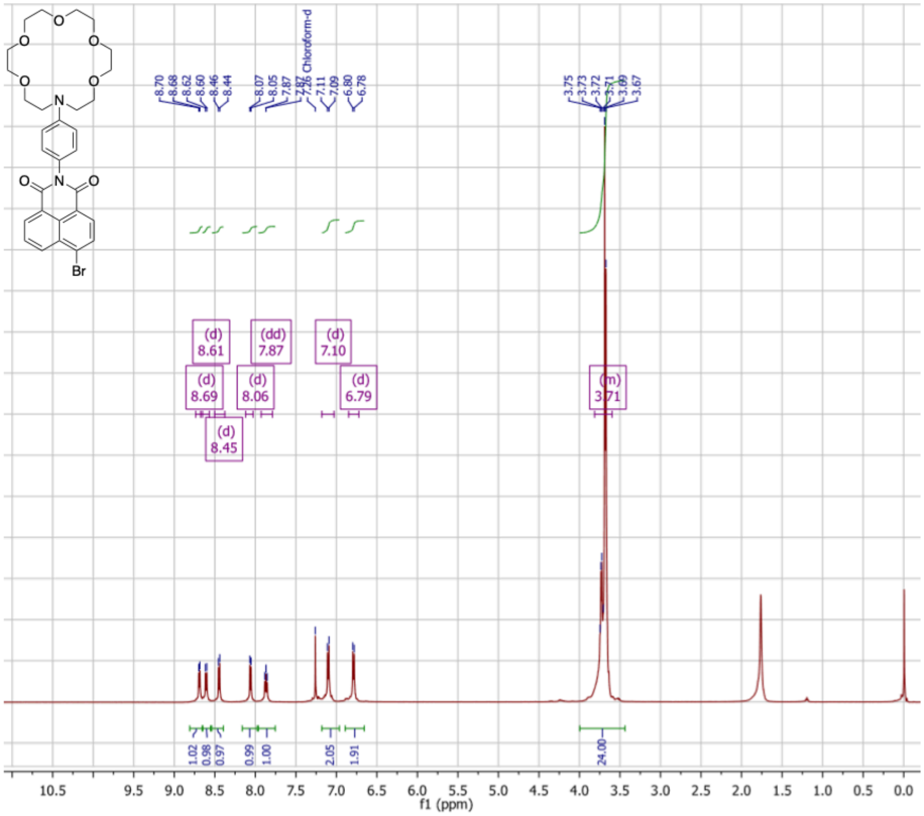

4B ^{1}H NMR ($CDCl_3$,500 MHz)

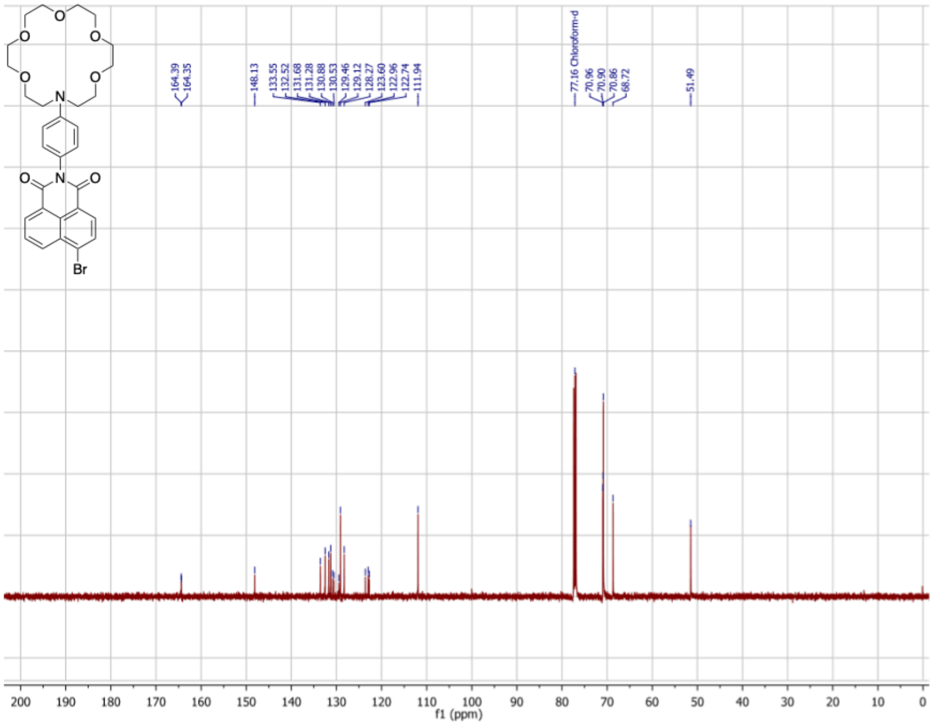

4B ^{13}C NMR ($CDCl_3$, 125 MHz)

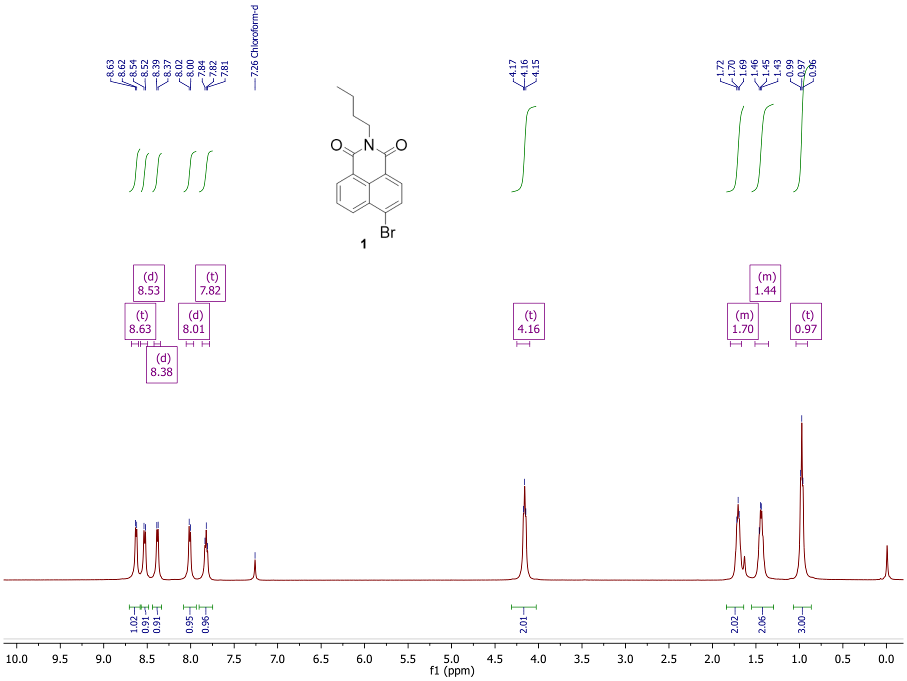

^{1}H NMR (CDCl$_3$, 500 MHz)

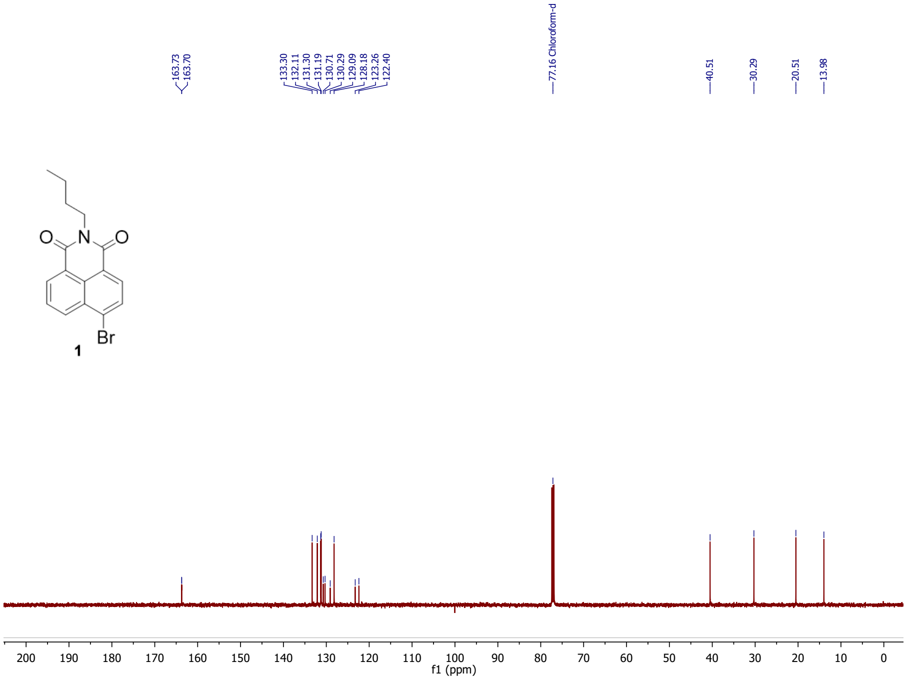

^{13}C NMR (CDCl$_3$, 125 MHz)

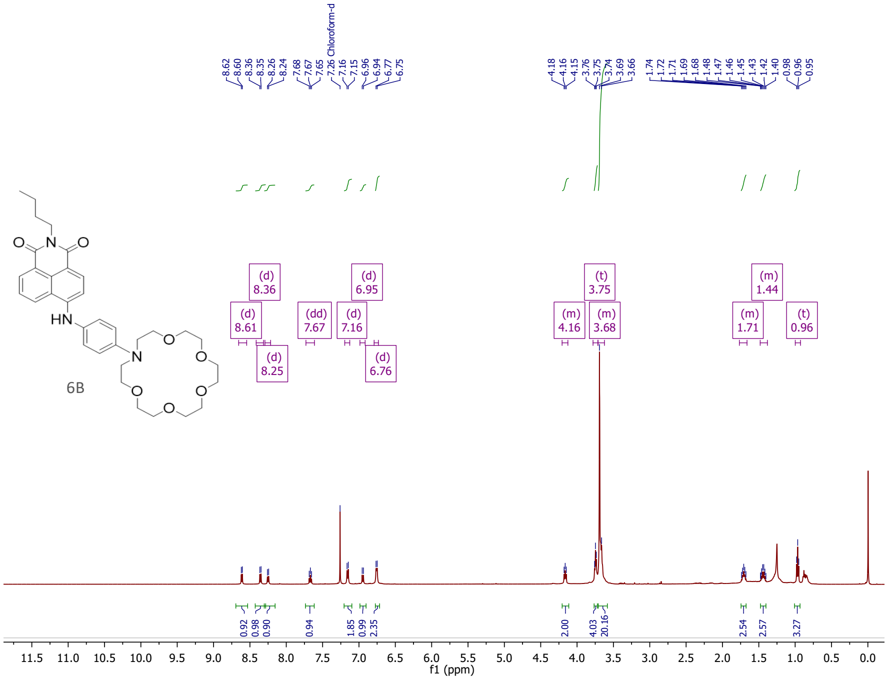

^{1}H NMR (CDCl$_3$, 500 MHz)

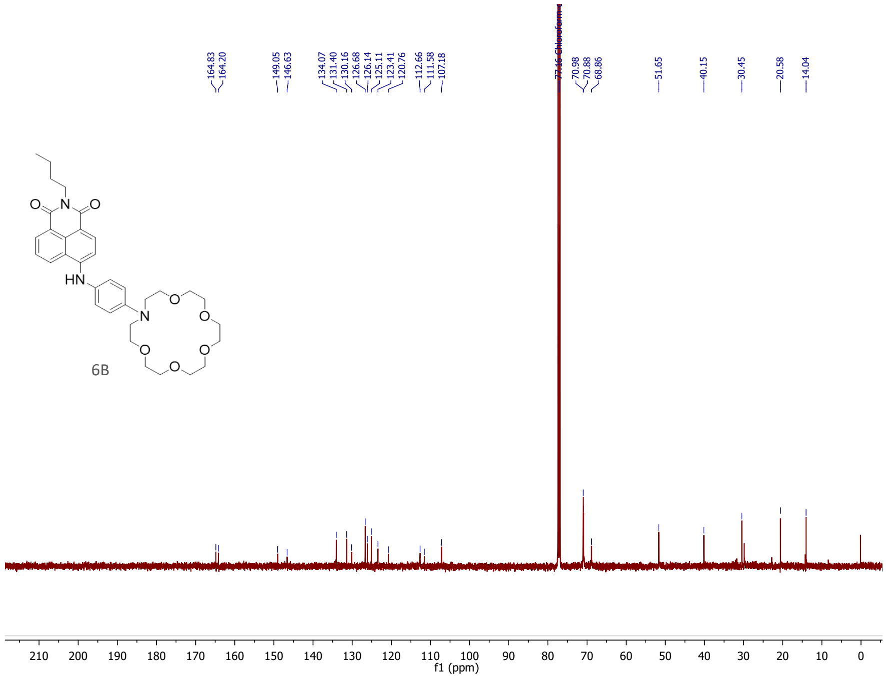

^{13}C NMR (CDCl$_3$, 125 MHz)

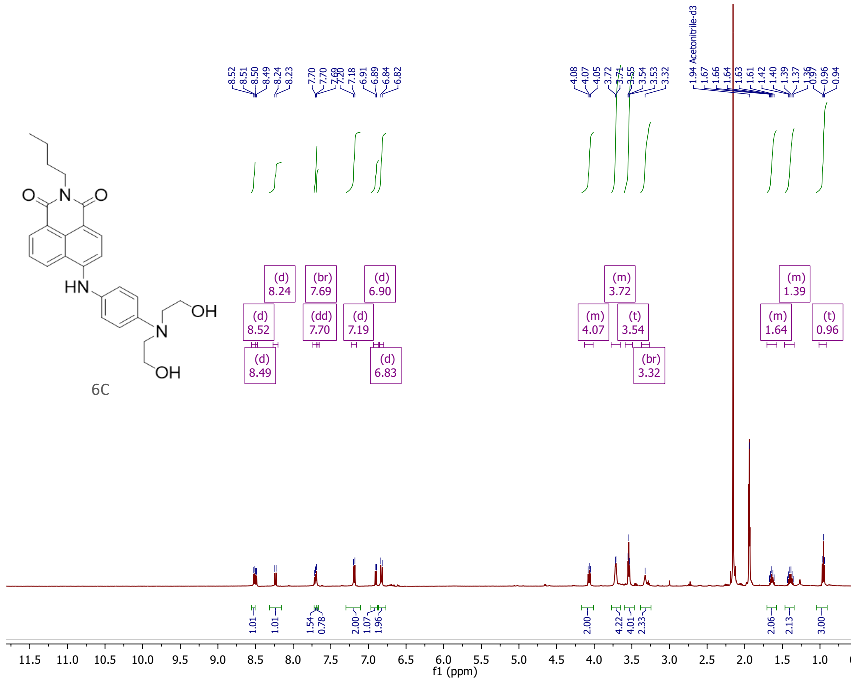

^{1}H NMR (CDCl$_3$, 500 MHz)

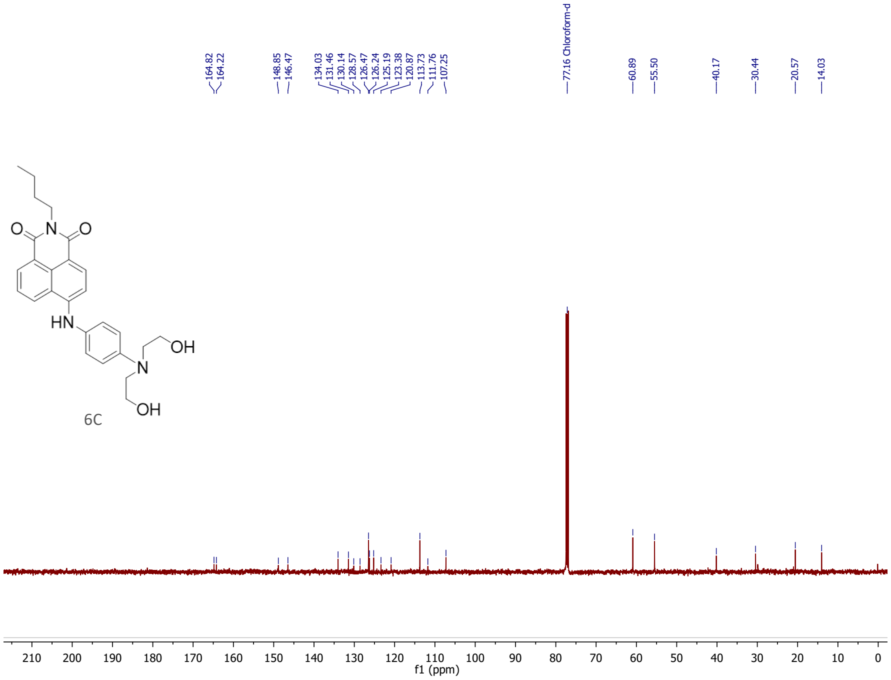

^{13}C NMR (CDCl$_3$, 125 MHz)

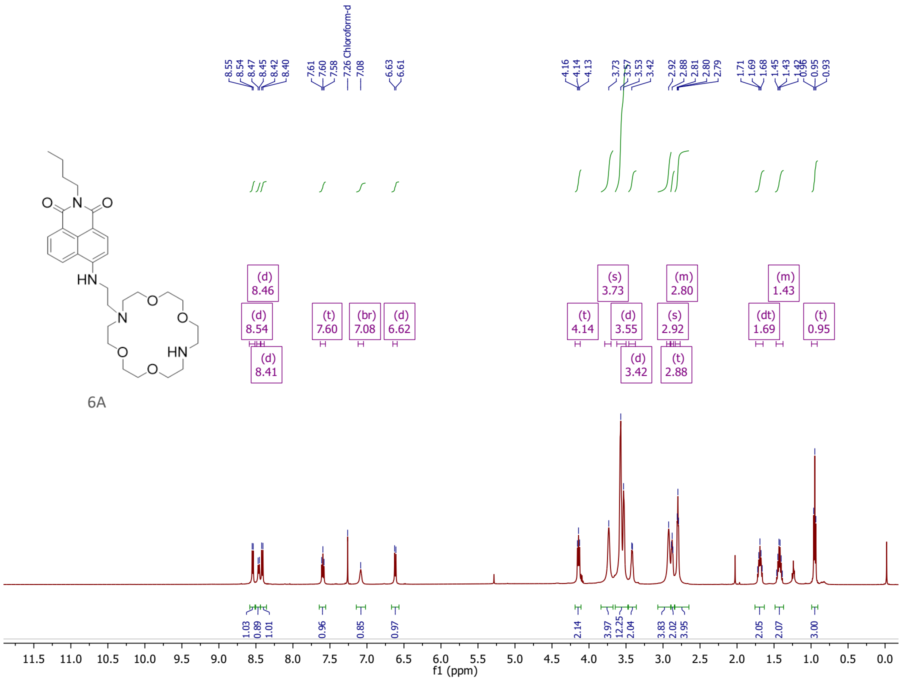

^{1}H NMR (CDCl$_3$, 500 MHz)

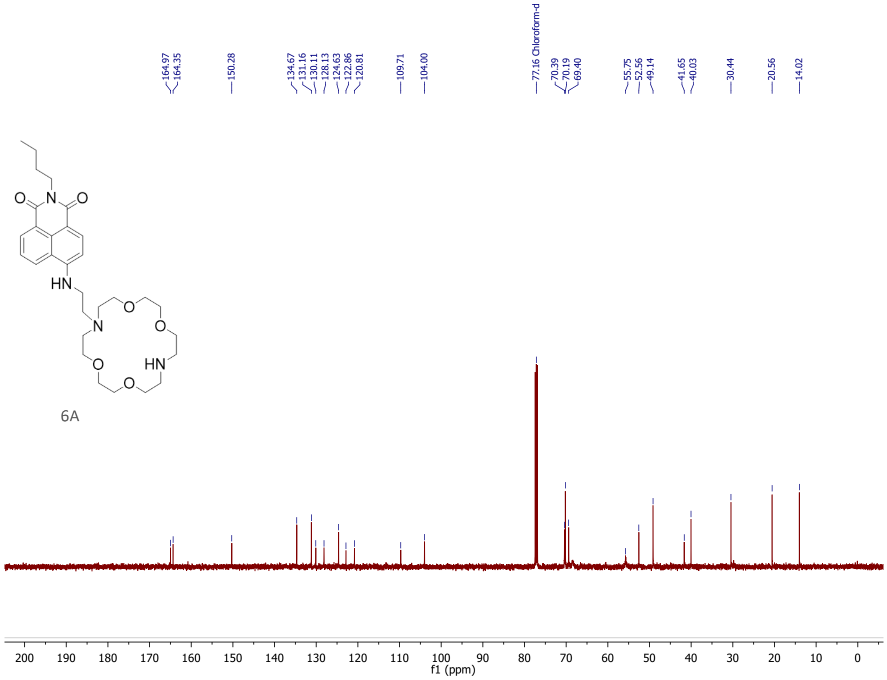

^{13}C NMR (CDCl$_3$, 125 MHz)

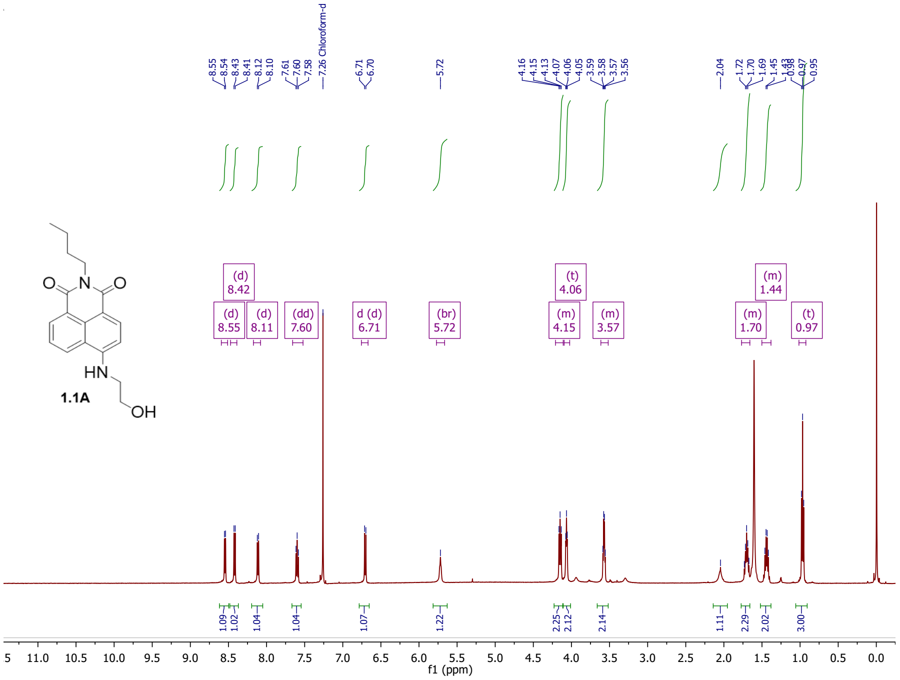

^{1}H NMR (CDCl$_3$, 500 MHz)

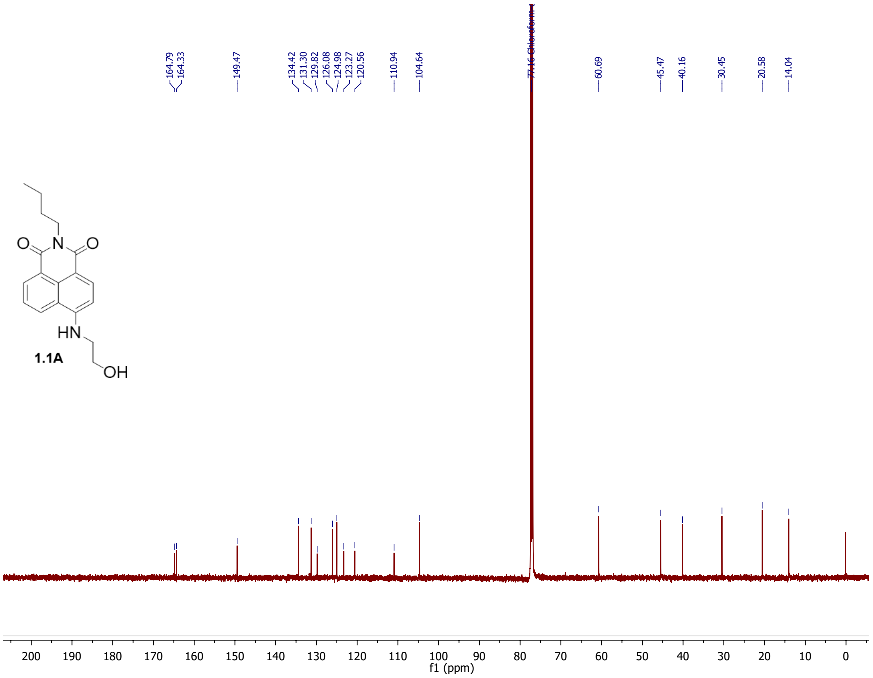

^{13}C NMR (CDCl$_3$, 125 MHz)

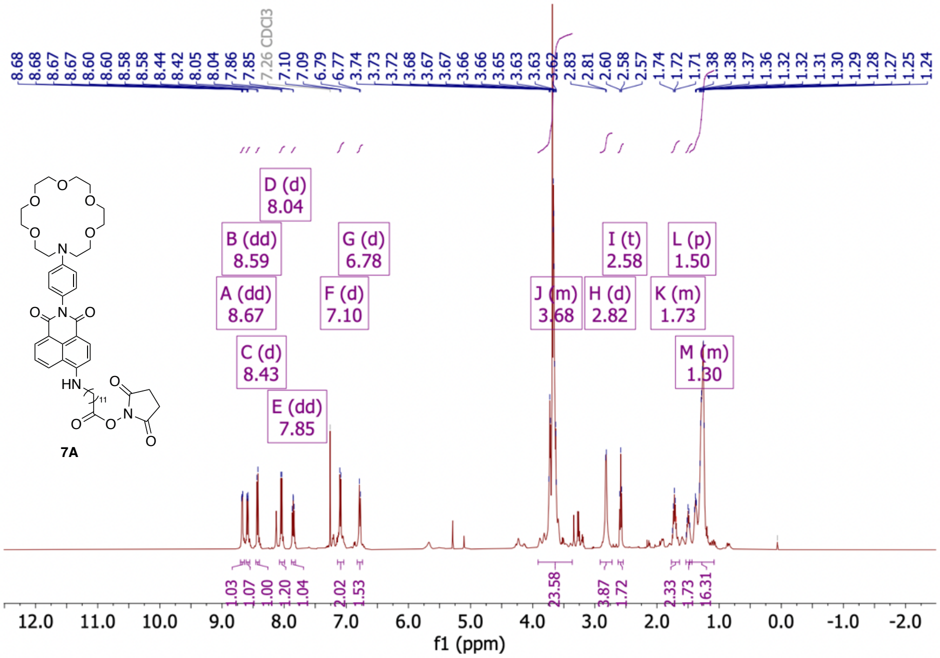

^{1}H NMR (CDCl$_3$, 500 MHz)

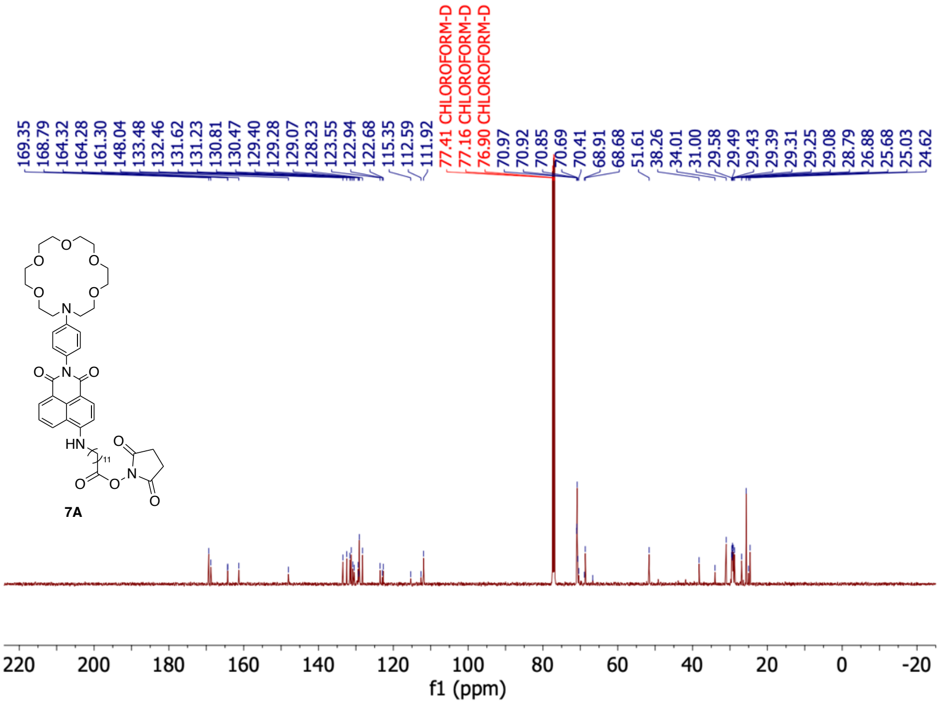

^{13}C NMR (CDCl$_3$, 125 MHz)

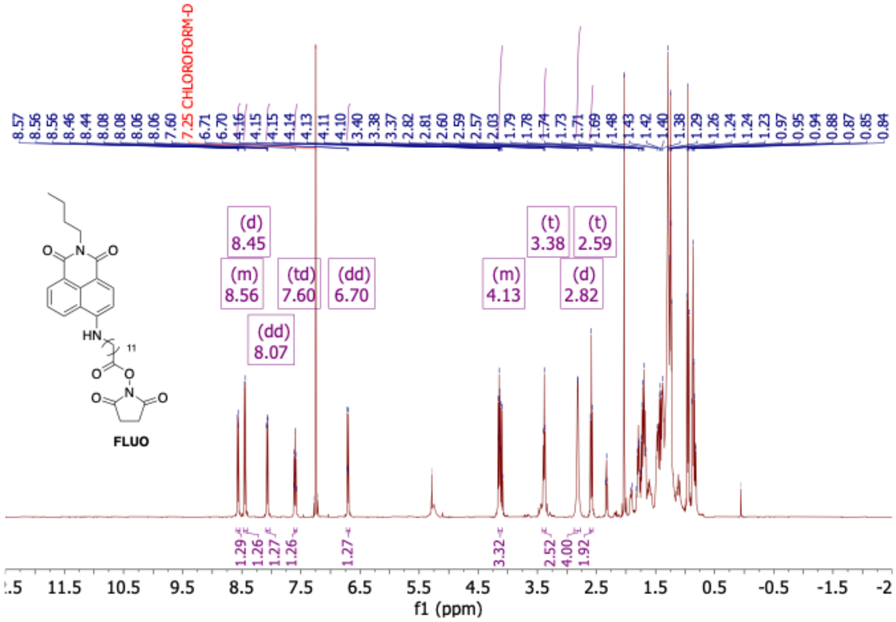

^{1}H NMR (CDCl$_3$, 500 MHz)

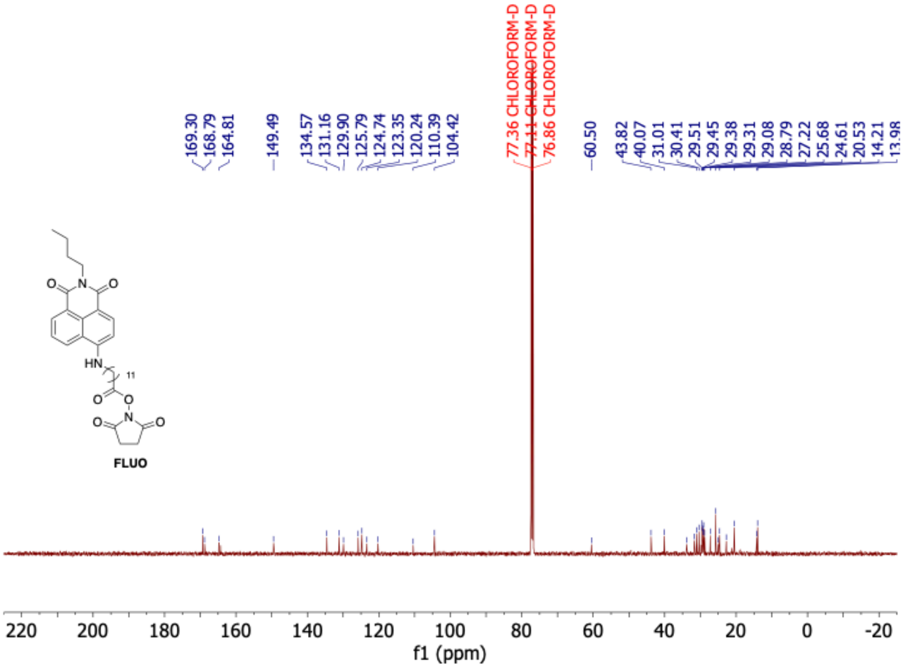

^{13}C NMR (CDCl$_3$, 125 MHz)

Reference

1. Simón, A., et al. Boosting Background Suppression in the next Experiment through Richardson-Lucy Deconvolution, 2021. arXiv:2102.11921v3.
2. Albert, J. B., et al. Search for Neutrinoless Double-Beta Decay with the Upgraded EXO-200 Detector. *Phys. Rev. Lett.* **2018**, *120*, 072701.
3. Hilke, H. J. Time Projection Chambers. *Rep. Prog. Phys.* **2010**, *73* (11), 116201.
4. Jones, B.; McDonald A.; Nygren, D. Single-molecule fluorescence imaging as a technique for barium tagging in neutrinoless double beta decay. *J. Instrum.* **2016**, *11*, P12011.
5. Chang, D.; Mohapatra, R. N. Comment on the 'Seesaw' Mechanism for Small Neutrino Masses. *Phys. Rev.* **1985**, *D32*, 1248.
6. Minkowski, P. μ → eγ at a rate of one out of 109 muon decays. *Phys. Lett.* **1977**, *B67*, 421–428.
7. Gell-Mann, M.; Ramond, P.; Slansky, R. Complex spinors and unified theories. *Supergravity*, *ed*. P. van Nieuwenhuizen DZ Free. *North–Holland*, *Amsterdam,* (1979).
8. Yanagida, T. *et al*. Proceedings of the workshop on the unified theory and the baryon number in the universe (1979).
9. Mohapatra, R. N.; Senjanović, G. Neutrino masses and mixings in gauge models with spontaneous parity violation. *Phys. Rev.* **1981**, D23, 165.
10. Fukugita, M.; Yanagida, T. Baryogenesis Without Grand Unification. *Phys. Lett.* **1986**, *B174*, 45–47.
11. Gando, A. *et al*. Search for Majorana Neutrinos near the Inverted Mass Hierarchy Region with KamLAND-Zen. *Phys*. *Rev*. *Lett*. **2016**, *117*, 082503, (2016).
12. Gomez-Cadenas, J. J.; Martin-Albo, J.; Mezzetto, M.; Monrabal, F.; Sorel, M. The Search for neutrinoless double beta decay. *Riv. Nuovo Cim.* **2012**, *35*, 29–98.
13. Bilenky, S. M.; Giunti, C. Neutrinoless double-beta decay: A brief review. *Mod. Phys. Lett.* **2012**, *A27*, 1230015.
14. Vergados, J. D.; Ejiri, H.; Simkovic, F. Theory of Neutrinoless Double Beta Decay. *Rept. Prog. Phys.* **2012**, *75*, 106301.

15. Martín-Albo, J. *et al*. Sensitivity of NEXT-100 to Neutrinoless Double Beta Decay. *JHEP 05*, **2016**, 159.
16. Novella, P. *et al*. Measurement of radon-induced backgrounds in the NEXT double beta decay experiment. *JHEP 10*, **2018**, 112.
17. Rupp, N. Radon background in liquid xenon detectors. *JINST 13*, **2018,** C02001.
18. Carson, M. J. *et al*. Neutron background in large scale xenon detectors for dark matter searches. *Astropart. Phys.* **2004**, *21,* 667–687.
19. Alvarez, V. *et al*. Radiopurity control in the NEXT-100 double beta decay experiment: procedures and initial measurements. *JINST 8*, **2013**, T01002.
20. Cebrián, S. *et al*. Radiopurity assessment of the tracking readout for the NEXT double beta decay experiment. *JINST 10*, **2015**, P05006.
21. Cebrián, S. *et al*. Radiopurity assessment of the energy readout for the NEXT double beta decay experiment. *JINST 12,* **2017**, T08003.
22. Agostini, M. *et al*. Improved Limit on Neutrinoless Double-β Decay of 76Ge from GERDA Phase II. *Phys. Rev. Lett.* ***2018**, 120*, 132503.
23. Aalseth, C. E. *et al*. Search for Neutrinoless Double β Decay in 76Ge with the Majorana Demonstrator. *Phys. Rev. Lett.* **2018**, *120*, 132502.
24. Renner, J. *et al*. Initial results on energy resolution of the NEXT-White detector. *JINST 13*, **2018**, P10020.
25. Moe, M. K. New approach to the detection of neutrinoless double-beta decay. *Phys. Rev.* **1991**, *C44*, 931–934.
26. McDonald, A. D. *et al*. Demonstration of Single Barium Ion Sensitivity for Neutrinoless Double Beta Decay using Single-Molecule Fluorescence Imaging. *Phys. Rev. Lett.* ***2018**, 120*, 132504.
27. Chambers, C. *et al*. Imaging individual ba atoms in solid xenon for barium tagging in nexo. *Unpublished* (2018).
28. Albert, J. B. *et al*. Measurements of the ion fraction and mobility of α- and β -decay products in liquid xenon using the EXO-200 detector. *Phys. Rev.* **2015**, *C92*, 045504.

29. Sinclair, D. *et al*. Prospects for Barium Tagging in Gaseous Xenon. *J. Phys. Conf. Ser.* **2011**, *309*, 012005.

30. Mong, B. *et al*. Spectroscopy of Ba and Ba+ deposits in solid xenon for barium tagging in nEXO. *Phys. Rev.* **2015***, A91*, 022505.

31. Nygren, D. Detection of the barium daughter in ^{136}Xe to ^{136}Ba + 2e$^-$ by in situ single-molecule fluorescence imaging. *Nucl. Instruments Methods Phys. Res. Sect. A: Accel. Spectrometers, Detect. Assoc. Equip.* **2016**, 824, 2–5.

32. Stuurman, N. & Vale, R. Imaging single molecules using total internal reflection fluorescence microscopy (2006).

33. Fish, K. N. Total internal reflection fluorescence (tirf) microscopy. *Curr. Protoc. Cytom.* **2009**, *50*, 12–18.

34. Thomas, D. *et al*. A comparison of fluorescent Ca^{2+} indicator properties and their use in measuring elementary and global Ca^{2+} signals. *Cell calcium* ***2000****, 28*, 213–23.

35. Lu, Y.; Paige, M. F. An ensemble and single-molecule fluorescence spectroscopy investigation of calcium green 1, a calcium-ion sensor. *J. Fluoresc.* **2007**, *17*, 739–748.

36. Oliver, E.; Baker, G.; Fugate, R. D.; Tablin, F.; Crowe, J. H. Effects of temperature on calcium-sensitive fluorescent probes. *Biophys. J.* ***2000****, 78*, 2116–2126.

37. Nakahara, Y.; Kida, T.; Nakatsuji, Y.; Akashi, M. New fluorescence method for the determination of the critical micelle concentration by photosensitive monoazacryptand derivatives. *Langmuir,* **2005**, *21*, 6688–6695.

38. Axelrod, D. [1] total internal reflection fluorescence microscopy in cell biology. In *Methods in enzymology*, vol. 361, 1–33 (Elsevier, 2003).

39. Monrabal, F. *et al*. The Next White (NEW) Detector. *JINST 13,* **2018**, P12010.

40. Byrnes, N. *et al*. Progress toward Barium Tagging in High-Pressure Xenon Gas with Single-Molecule Fluorescence Imaging. In *9th Symposium on Large TPCs for Low-Energy Rare Event Detection* (*TPC2018*) *Paris*, *France*, *December 12–14*, *2018* (2019).

41. Nakahara, Y.; Kida, T.; Nakatsuji, Y.; Akashi, M. A novel fluorescent indicator for Ba^{2+} in aqueous micellar solutions. *Chem*. *Commun*, **2004**, 224–225.

42. Chaichana, K.; Phutlaprungrueang, N.; Chaicharoenwimolkul, L.; Promkatkaew, M.; Kongsriprapan, S. A selective fluorescence probe based on naphthalene for the detection of barium (ii). *Spectrochimica Acta Part A: Mol. Biomol. Spectrosc.* **2019**, *207,* 118–122.

43. Kondo, S.; Takahashi, T.; Takiguchi, Y.; Unno, M. Synthesis and photophysical properties of a 2, 2'-bianthracene-based receptor bearing two aza-15-crown-5 ethers for naked-eye detection of barium ion. *Tetrahedron letters.* **2011**, *52*, 453–457.

44. Gomez-Cadenas, J. J. Status and prospects of the NEXT experiment for neutrinoless double beta decay searches (2019).

45. Bollen, G. "ion surfing" with radiofrequency carpets. *Int. J. Mass Spectrom.* **2011***, 299*, 131–138.

46. Brunner, T. *et al*. An RF-only ion-funnel for extraction from high-pressure gases. *Int. J. Mass Spectrom.* **2015**, *379*, 110.

47. Gornea, R. *et al*. Search for double beta decay with the exo-200 tpc and prospects for barium ion tagging in liquid xenon. In *Journal of Physics: Conference Series*, **2011**, *309,* 012003.

48. Escudero, D. Revising intramolecular photoinduced electron transfer (pet) from first-principles. *Acc. Chem. Res.* **2016***, 49,* 1816–1824.

49. Hughes, W. *et al*. Aza-crown ether-core substituted naphthalene diimide fluorescence "turn-on" probe for selective detection of Ca^{2+}. *Sensors Actuators B: Chem.* **2017**, *244,* 854–860.

50. Roy, B. *et al*. Amplified fluorescence emission of bolaamphiphilic perylene-azacrown ether derivatives directed towards molecular recognition events. *Phys. Chem. Chem. Phys.* **2016**, *18,* 13239–13245.

51. Dhenadhayalan, N. *et al*. Silicon quantum dot-based fluorescence turn-on metal ion sensors in live cells. *ACS Appl. Mater. Interfaces,* **2016**, *8,* 23953–23962.

52. Späth, A.; Koch, C.; König, B. Luminescent hybrids combining a metal complex and a crown ether–receptors for peptidic ammonium phosphates. *Eur. J. Inorg. Chem.* **2010**, 2926–2935.

53. Krakowiak, K. E.; Bradshaw, J. S.; Zamecka-Krakowiak, D. J. Synthesis of aza-crown ethers. *Chem. Rev.* ***1989***, *89,* 929–972.

54. Wang, Q.; Wang, X.; Li, L. Density functional theory study on a fluorescent chemosensor device of aza-crown ether. *J. Phys. Org. Chem.* **2014**, *27*, 546–554.

55. Gromov, S. P. *et al*. N-methylbenzoazacrown ethers with the nitrogen atom conjugated with the benzene ring: the improved synthesis and the reasons for the high stability of complexes with metal and ammonium cations. *J. Phys. Org. Chem.* **2009**, *22*, 823–833.
56. Lochman, L.; Svec, J.; Roh, J.; Novakova, V. The role of the size of aza-crown recognition moiety in azaphthalocyanine fluorescence sensors for alkali and alkaline earth metal cations. *Dye. Pigments.* **2015***, 121*, 178–187.
57. Shinkai, S.; Kinda, H.; Manabe, O. Photo responsive complexation of metal cations with an azobenzene-crown-azobenzene bridge immobilized in polymer supports. *J. Am. Chem. Soc.* **1982**, *104*, 2933–2934.
58. Moerner, W.; Fromm, D. P. Methods of single-molecule fluorescence spectroscopy and microscopy. *Rev. Sci. instruments.* **2003***, 74,* 3597–3619.
59. Steed, J. W. First-and second-sphere coordination chemistry of alkali metal crown ether complexes. *Coord. Chem. Rev.* **2001**, *215,* 171–221.
60. Birks, J. B. The Pyrene Excimer. *Acta Phys. Polonica.* **1968**, *34*, 603–617.
61. Mizoue, L. S.; Tellinghuisen, J. Calorimetric vs. van’t hoff binding enthalpies from isothermal titration calorimetry: Ba2+-crown ether complexation. *Biophys. Chemistry.* **2004**, *110*, 15–24.
62. Clark, C. D.; De Bruyn, W. J.; Ting, J.; Scholle, W. Solution medium effects on the photochemical degradation of pyrene in water. *J. Photochem. Photobiol. A: Chem.* ***2007***, *186*, 342–348.
63. Zhan, W. *et al*. Integrating docking scores, interaction profiles and molecular descriptors to improve the accuracy of molecular docking: toward the discovery of novel akt1 inhibitors. *Eur. journal medicinal chemistry.* ***2014***, *75*, 11–20.
64. Luk’yanenko, N.; Basok, S.; Kulygina, E. Y.; Bogashchenko, T. Y.; Yakovenko, I. Synthesis of monoazacrown ethers under phase-transfer catalysis. *Russ. J. Org. Chem.* **2012**, *48,* 1345–1352.
65. Malwal, S. R.; Chakrapani, H. Benzosulfones as photochemically activated sulfur dioxide (so 2) donors. *Org. & biomolecular chemistry.* **2015**, *13,* 2399–2406.
66. Bair, K. W. *et al*. 2-[(Arylmethyl)amino]-2-methyl-1,3-propanediol DNA intercalators. An examination of the effects of aromatic ring variation on antitumor activity and DNA binding. *J. Med. Chem*. **1991**, *34,*1983-1990.

67. Zeng, Z.; Torriero, A. A. J.; Bond, A. M.; Spiccia, M. Fluorescent and Electrochemical Sensing of Polyphosphate Nucleotides by Ferrocene Functionalised with Two ZnII(TACN)(pyrene) Complexes. *Chem. Eur. J.* **2010***, 16*, 9154–9163.
68. Mao, H.; Thorne, J. B.; Pharr, J. S.; Gawley, R. E. Effect of crown ether ring size on binding and fluorescence response to saxitoxin in anthracylmethyl monoazacrown ether chemosensors. *Can. J. Chem.* **2006***, 84,* 1273-1279.
69. Chambers, C.; Walton, T.; Fairbank, D.; Craycraft, A.; Yahne, D.; Todd, J.; Iverson, A.; Fairbank, W.; Alamre, A.; Albert, J.; et al. Imaging individual barium atoms in solid xenon for barium tagging in nEXO. Nature **2019**, *569*, 203.
70. McDonald, A. D.; Jones, B. J. P.; Nygren, D. R.; Adams, C.; Álvarez, V.; Azevedo, C. D. R.; Benlloch-Rodríguez, J. M.; Borges, F. I. G. M.; Botas, A.; Carcel, S.; et al. Demonstration of single-barium-ion´ sensitivity for neutrinoless double-beta decay using single-molecule fluorescence imaging. Phys. Rev. Lett. **2018**, *120*, 132504.
71. Nygren, D. R. Detection of the barium daughter in ^{136}Xe ^{136}Ba + 2e^{-} by in situ single-molecule fluorescence imaging. Nucl. Instrum. Methods Phys. Res., Sect. A. **2016**, *2,* 824.
72. De Silva, A. P.; Gunaratne, H. Q. N.; Gunnlaugsson, T.; Huxley, A. J. M.; McCoy, C. P.; Rademacher, J. T.; Rice, T. E. Signaling recognition events with fluorescent sensors and switches. Chem. Rev. **1997**, *97*, 1515−1566.
73. Valeur, B.; Leray, I. Design principles of fluorescent molecular sensors for cation recognition. Coord. Chem. Rev. **2000**, *205*, 3−40.
74. Hamilton, G. R. C.; Sahoo, S. K.; Kamila, S.; Singh, N.; Kaur, N.; Hyland, B. W.; Callan, J. F. Optical probes for the detection of protons, and alkali and alkaline earth metal cations. Chem. Soc. Rev. **2015**, *44*, 4415−4432.
75. Duke, R. M.; Veale, E. B.; Pfeffer, F. M.; Kruger, P. E.; Gunnlaugsson, T. Colorimetric and fluorescent anion sensors: an overview of recent developments in the use of 1,8-naphthalimidebased chemosensors. Chem. Soc. Rev. **2010**, *39*, 3936−3953.

76. Panchenko, P. A.; Fedorova, O. A.; Fedorov, Y. V. Fluorescent and colorimetric chemosensors for cations based on 1,8-naphthalimide derivatives: design principles and optical signalling mechanisms. Russ. Chem. Rev. **2014**, *83*, 155.

77. Panchenko, P. A.; Fedorov, Y. V.; Fedorova, O. A.; Jonusauskas, G. Comparative analysis of the PET and ICT sensor properties of 1,8- naphthalimides containing aza-15-crown-5 ether moiety. Dyes Pigm. **2013**, *98*, 347−357.

78. Gao, Z.; Hao, Y.; Zheng, M.; Chen, Y. A fluorescent dye with large Stoke's shift and high stability: synthesis and application to live cell imaging. RSC Adv. **2017**, *7*, 7604−7609.

79. Alfimov, M.; Gromov, S. Applied Fluorescence in Chemistry, Biology and Medicine; Springer, 1999; pp 161−178.

80. Hou, C.; Urbanec, A. M.; Cao, H. A rapid Hg^{2+} sensor based on aza-15-crown-5 ether functionalized 1,8-naphthalimide. Tetrahedron Lett. **2011**, *52*, 4903−4905.

81. Panchenko, P. A.; Park, V. V.; Fedorova, O. A.; Fedorov, Y. V.; Kataev, E. A. Cation-dependent spectral properties of fluorescent complexon based on 1,8-naphthalimide with PET mechanism of optical response. Russ. Chem. Bull. **2015**, *64*, 1871−1876.

82. Panchenko, P. A.; Fedorov, Y. V.; Fedorova, O. A. Selective fluorometric sensing of Hg2+ in aqueous solution by the inhibition of PET from dithia-15-crown-5 ether receptor conjugated to 4-amino1,8-naphthalimide fluorophore. J. Photochem. Photobiol. **2018**, *364*,124−129.

83. Panchenko, P. A.; Polyakova, A. S.; Fedorov, Y. V.; Fedorova, O. A. Chemoselective detection of Ag^{+} in purely aqueous solution using fluorescence 'turn-on'probe based on crown-containing 4-methoxy-1,8-naphthalimide. Mendeleev Commun. **2019**, *29*, 155−157.

84. Georgiev, N. I.; Dimitrova, M. D.; Todorova, Y. D.; Bojinov, V. B. Synthesis, chemosensing properties and logic behaviour of a novel ratiometric 1,8-naphthalimide probe based on ICT and PET. Dyes Pigm. **2016**, *131*, 9−17.

85. Fernandez-Alonso, S.; Corrales, T.; Pablos, J. L.; Catalina, F.´Solid fluorescence sensors obtained by functionalization of photocrosslinked water-swollen acrylic membranes with 4-piperazine naphthalimide derivatives. Polymer. **2017**, *124*, 139−150.

86. Aderinto, S. O.; Zhang, H.; Wu, H.; Chen, C.; Zhang, J.; Peng, H.; Yang, Z.; Wang, F. Synthesis and studies of two proton−receptor fluorescent probes based on 1,8-naphthalimide. Color. Technol. **2017**, *133*, 40−49.

87. Georgiev, N. I.; Krasteva, P. V.; Bojinov, V. B. A ratiometric 4-amido-1,8-naphthalimide fluorescent probe based on excimermonomer emission for determination of pH and water content in organic solvents. *J. Lumin.* **2019**, *212*, 271−278.

88. Licchelli, M.; Orbelli Biroli, A.; Poggi, A. A prototype for the chemosensing of Ba^{2+} based on self-assembling fluorescence enhancement. Org. Lett. **2006**, *8*, 915−918.

89. Patnaik, P. Handbook of Inorganic Chemicals; McGraw-Hill: New York, 2003; Vol. 529.

90. Zhao, J.-M.; Zong, Q.-S.; Chen, C.-F. Complexation of triptycene-based macrotricyclic host toward (9-anthracylmethyl) benzylammonium salt: a Ba^{2+} selective fluorescence probe. *J. Org. Chem*. **2010**, *75*, 5092−5098.

91. Saluja, P.; Kaur, N.; Singh, N.; Jang, D. O. A benzthiazole-based tripodal chemosensor for Ba^{2+} recognition under biological conditions. Tetrahedron Lett. **2011**, *52*, 6705−6708.

92. Banerjee, T.; Suresh, M.; Ghosh, H. N.; Das, A. Competitive binding of Ba^{2+} and Sr^{2+} to 18-Crown-6 in a Receptor with a 1-Methoxyanthraquinone Analogue as the Other Binding Site. *Eur. J. Inorg. Chem*. **2011**, 4680−4690.

93. Basa, P. N.; Bhowmick, A.; Schulz, M. M.; Sykes, A. G. Siteselective imination of an anthracenone sensor: selective fluorescence detection of barium (II). *J. Org. Chem*. **2011**, *76*, 7866−7871.

94. Guo, H.; Kuwabara, T. Colorimetric Chemosensor for Barium Metal Ions Using Tris (bipyridinium−crown ether) Conjugate. *Chem. Lett.* **2013**, *42*, 194−196.

95. García Grajeda, B. A.; Soto Acosta, S. G.; Aguila, S. A.; Peinado Guevara, H.; Díaz García, M. E.; Cruz Enríquez, A.; Campos Gaxiola, J. J. Selective and colorimetric detection of Ba^{2+} ions in aqueous solutions using 11-mercaptoundecylphosphonic acid functionalized gold nanoparticles. *RSC Adv*. **2017**, *7*, 31611.

96. Li, F.; Zhong, K.; Hou, S.; Tang, L.; Bian, Y. A simple and efficient fluorescent probe for detecting Ba^{2+} and its various applications. *Tetrahedron Lett.* **2020**, *61*, 151558.

97. Kravchenko, J.; Darrah, T. H.; Miller, R. K.; Lyerly, H. K.; Vengosh, A. A review of the health impacts of barium from natural and anthropogenic exposure. *Environ. Geochem. Health.* **2014**, *36*, 797−814.
98. Łukasik-Głębocka, M.; Sommerfeld, K.; Hanć, A.; Grzegorowski, A.; Barałkiewicz, D.; Gaca, M.; Zielinska-Psuja, B. Barium determination in gastric contents, blood and urine by inductively coupled plasma mass spectrometry in the case of oral barium chloride poisoning. *J. Anal. Toxicol.* **2014**, *38*, 380−382.
99. Thapa, P.; Arnquist, I.; Byrnes, N.; Denisenko, A.; Foss, F.; Jones, B.; McDonald, A.; Nygren, D.; Woodruff, K. Barium chemosensors with Dry-phase fluorescence for neutrinoless Double Beta Decay. *Sci. Rep*. **2019**, *9*, 15097.
100. Yang, C.; Liu, L.; Zeng, T.; Yang, D.; Yao, Z.; Zhao, Y.; Wu, H.- C. Highly sensitive simultaneous detection of lead (II) and barium (II) with G-quadruplex DNA in α-hemolysin nanopore. *Anal. Chem*. **2013**, *85*, 7302−7307.
101. Xu, L.; Chen, Y.; Zhang, R.; Gao, T.; Zhang, Y.; Shen, X.; Pei, R. A highly Sensitive Turn-on Fluorescent Sensor for Ba2+ Based on G-Quadruplexes. *J. Fluoresc*. **2017**, *27*, 569−574.
102. Ravichandiran, P.; Subramaniyan, S. A.; Bella, A. P.; Johnson, P. M.; Kim, A. R.; Shim, K. S.; Yoo, D. J. Simple fluorescence turn-on chemosensor for selective detection of Ba2+ ion and its live-cell imaging. *Anal. Chem.* **2019**, *91*, 10095−10101.
103. Adams, C.; Alvarez, V.; Arazi, L.; Arnquist, I.; Azevedo, C.; Bailey, K.; Ballester, F.; Benlloch-Rodriguez, J.; Borges, F.; Byrnes, N.; et al. Sensitivity of a tonne-scale NEXT detector for neutrinoless double beta decay searches, 2020. arXiv:2005.06467.
104. Rivilla, I.; Aparicio, B.; Bueno, J. M.; Casanova, D.; Tonnele, ́ C.; Freixa, Z.; Herrero, P.; Rogero, C.; Miranda, J. I.; Martínez-Ojeda, R. M.; et al. Fluorescent bicolour sensor for low-background neutrinoless double β decay experiments. *Nature*. **2020**, *583*, 48−54.
105. Koonrugsa, N.; Fuangswasdi, S. Metal ion chemosensors based on diaza-18-crown-6 coupling with azobenzene dye. *Spectrochim. Acta, Part A.* **2019**, *215*, 15−23.
106. Zhao, Y.; Truhlar, D. G. The M06 suite of density functionals for main group thermochemistry, thermochemical kinetics, noncovalent interactions, excited states, and transition elements: two new

functionals and systematic testing of four M06-class functionals and 12 other functionals. *Theor. Chem. Acc.* **2008**, *120*, 215−241.

107. Dolg, M.; Wedig, U.; Stoll, H.; Preuss, H. Energy-adjusted abinitio pseudopotentials for the first row transition elements. *J. Chem. Phys*. **1987**, *86*, 866−872.
108. Kaupp, M.; Schleyer, P. v. R.; Stoll, H.; Preuss, H. Pseudopotential approaches to Ca, Sr, and Ba hydrides. Why are some alkaline earth MX2 compounds bent? *J. Chem. Phys*. **1991**, *94*, 1360−1366.
109. Bergner, A.; Dolg, M.; Küchle, W.; Stoll, H.; Preuß, H. Ab initio energy-adjusted pseudopotentials for elements of groups 13−17*. Mol. Phys*. **1993**, *80*, 1431−1441.
110. Dolg, M.; Stoll, H.; Preuss, H.; Pitzer, R. M. Relativistic and correlation effects for element 105 (hahnium, Ha): a comparative study of M and MO (M= Nb, Ta, Ha) using energy-adjusted ab initio pseudopotentials. *J. Phys. Chem.* **1993**, *97*, 5852−5859.
111. Weigend, F.; Ahlrichs, R. Balanced basis sets of split valence, triple zeta valence and quadruple zeta valence quality for H to Rn: Design and assessment of accuracy. *Phys. Chem. Chem. Phys*. **2005**, *7*, 3297−3305.
112. Weigend, F. Accurate Coulomb-fitting basis sets for H to Rn. *Phys. Chem.* **2006**, *8*, 1057−1065.
113. Runge, E.; Gross, E. K. U. Density-functional theory for timedependent systems. *Phys. Rev. Lett*. **1984**, *52*, 997.
114. Marenich, A. V.; Cramer, C. J.; Truhlar, D. G. Universal solvation model based on solute electron density and on a continuum model of the solvent defined by the bulk dielectric constant and atomic surface tensions. *J. Phys. Chem. B***. 2009**, *113*, 6378−6396.
115. Hall, R. J.; Davidson, M. M.; Burton, N. A.; Hillier, I. H. Combined density functional, self-consistent reaction field model of solvation*. J. Phys. Chem*. **1995**, *99*, 921−924.
116. Frisch, M. J.; Trucks, G. W.; Schlegel, H. B.; Scuseria, G. E.; Robb, M. A., Jr.; Cheeseman, G.; Scalmani, V.; Barone, B.; Mennucci, G. A.; Petersson, H.; et al. Gaussian 09, R. A. 1; Gaussian Inc.: Wallingford CT, 2009.

117. Fabbrizzi, L.; Licchelli, M.; Pallavicini, P.; Perotti, A.; Taglietti, A.; Sacchi, D. Fluorescent sensors for transition metals based on electron-transfer and energy-transfer mechanisms. *Chem.-Eur. J.* **1996***, 2*, 75−82.

118. Callan, J. F.; de Silva, A. P.; Magri, D. C. Luminescent sensors and switches in the early 21st century. *Tetrahedron.* **2005**, *61*, 8551−8588.

119. Veale, E. B.; Kitchen, J. A.; Gunnlaugsson, T. Fluorescent trenbased 4-amino-1,8-naphthalimide sensor for Cu (II) based on the use of the (fluorophore−spacer−receptor) photoinduced electron transfer (PET) principle*. Supramol. Chem*. **2013**, *25*, 101−108.

120. Abdurahman, A.; Hele, T. J. H.; Gu, Q.; Zhang, J.; Peng, Q.; Zhang, M.; Friend, R. H.; Li, F.; Evans, E. W. Understanding the luminescent nature of organic radicals for efficient doublet emitters and pure-red light-emitting diodes. *Nat. Mater.* **2020**, *19*, 1224−1229.

121. Wang, L.; Qin, W.; Tang, X.; Dou, W.; Liu, W.; Teng, Q.; Yao, X. A selective, cell-permeable fluorescent probe for Al^{3+} in living cells. *Org. Biomol. Chem.* **2010**, *8*, 3751−3757.

122. Lee, H.; Lee, H.-S.; Reibenspies, J. H.; Hancock, R. D. Mechanism of “turn-on” fluorescent sensors for mercury (II) in solution and its implications for ligand design. *Inorg. Chem*. **2012**, *51*, 10904−10915.

123. Bainglass, E.; Jones, B. P.; Foss, F.; Huda, M.; Nygren, D. Mobility and Clustering of Barium Ions and Dications in High Pressure Xenon Gas. *Phys. Rev. A*. **2018**, *97*, 062509.

124. Tomiyasu T.; Okada M.; Imura R.; Sakamoto H. Vertical variations in the concentration of mercury in soils around Sakurajima Volcano, Southern Kyushu, Japan. *Science of The Total Environment*. **2003**, *304* (1), 221-230.

125. Schroeder WH, Keeler G, Kock H, Roussel P, Schneeberger D, Schaedlich F. International Field Intercomparison of Atmospheric Mercury Measurement Methods. In: Porcella DB, Huckabee JW, Wheatley B, editors. Mercury as a Global Pollutant: Proceedings of the Third International Conference held in Whistler, British Columbia, July 10–14, 1994. Dordrecht: Springer Netherlands; 1995. p. 611-20.

126. Sheu G.R.; Mason R.P. An Examination of Methods for the Measurements of Reactive Gaseous Mercury in the Atmosphere. *Environ. Sci. Technol*. **2001**, *35* (6), 1209-1216.

127. Thorneloe S.A.; Kosson D.S.; Sanchez F.; Garrabrants A.C.; Helms G. Evaluating the Fate of Metals in Air Pollution Control Residues from Coal-Fired Power Plants. *Environ. Sci. Technol*. **2010**, *44* (19), 7351-7356.

128. Tchounwou P.B.; Yedjou C.G.; Patlolla A.K.; Sutton D.J. Heavy metal toxicity and the environment. *Exp. Suppl*. **2012**, *101*, 133-164.

129. Tchounwou P.B.; Ayensu W.K.; Ninashvili N.; Sutton D. Review: Environmental exposure to mercury and its toxicopathologic implications for public health. *Environ. Toxicol.* **2003**, *18* (3), 149-175.

130. Baker J.P.; Mercury, Vaccines, and Autism. *A. J. Public Health*. **2008**, *98* (2), 244-53.

131. Nolan EM, Lippard SJ. Tools and Tactics for the Optical Detection of Mercuric Ion. *Chem Rev.* **2008**,*108* (9), 3443-3480.

132. Oh S.; Jeon J.; Jeong J.; Park J.; Oh E.T.; Park H.J.; *et al.* Fluorescent Detection of Methyl Mercury in Aqueous Solution and Live Cells Using Fluorescent Probe and Micelle Systems. *Anal Chem*. **2020**, *92* (7), 4917-4925.

133. Zhang Y.; Xiao J.Y.; Zhu Y.; Tian L.J.; Wang W.K.; Zhu T.T.; *et al*. Fluorescence Sensor Based on Biosynthetic CdSe/CdS Quantum Dots and Liposome Carrier Signal Amplification for Mercury Detection. *Anal. Chem*. **2020**, *92* (5), 3990-3997.

134. Chasapis C.T.; Loutsidou A.C.; Spiliopoulou C.A.; Stefanidou M.E. *Arch. Toxicol.* **2012**, *86,* 521-534.

135. Cui W.R.; Zhang C.R.; Jiang W.; Liang R.P.; Wen S.H.; Peng D.; et al. Covalent Organic Framework Nanosheet-Based Ultrasensitive and Selective Colorimetric Sensor for Trace Hg^{2+} Detection. *ACS Sustain. Chem. Eng.* **2019**, *7* (10), 9408-9415.

136. Xiaoxiong Z.; Wenjun Z.; Cuiliu L.; Xiaohong Q.; Chengyu Z. Eu3+-Postdoped UIO-66-Type Metal–Organic Framework as a Luminescent Sensor for Hg^{2+} Detection in Aqueous Media. Inorg. Chem. **2019**, *58* (6), 3910-3915.

137. Malek A.; Bera K.; Biswas S.; Perumal G.; Das AK.; Doble M.; et al. Development of a Next-Generation Fluorescent Turn-On Sensor to Simultaneously Detect and Detoxify Mercury in Living Samples. *Anal. Chem.* **2019**, *91* (5), 3533-3538.

138. Chatterjee A.; Banerjee M.; Khandare DG.; Gawas R.U.; Mascarenhas S.C.; Ganguly A.; et al. Aggregation-Induced Emission-Based Chemodosimeter Approach for Selective Sensing and Imaging of Hg(II) and Methylmercury Species. *Anal. Chem*. **2017**, *89* (23), 12698-12704.

139. Shaily; Kumar A.; Ahmed N. Indirect Approach for CN– Detection: Development of "Naked-Eye" Hg^{2+}-Induced Turn-Off Fluorescence and Turn-On Cyanide Sensing by the Hg^{2+} Displacement Approach. Ind. Eng. Chem. Res. **2017**, *56* (22), 6358-6368.

140. Zhang S.; Zhang D.; Zhang X.; Shang D.; Xue Z.; Shan D.; et al. Ultratrace Naked-Eye Colorimetric Detection of Hg^{2+} in Wastewater and Serum Utilizing Mercury-Stimulated Peroxidase Mimetic Activity of Reduced Graphene Oxide-PEI-Pd Nanohybrids. *Anal. Chem*. **2017**, *89* (6), 3538-3544.

141. Ge Y, Liu A, Ji R, Shen S, Cao X. Detection of Hg^{2+} by a FRET ratiometric fluorescent probe based on a novel pyrido[1,2-a]benzimidazole-rhodamine system. Sens. Actuators, B: Chemical. **2017**, *251*, 410-415.

142. Ge Y.; Xing X.; Liu A.; Ji R.; Shen S.; Cao X. A novel imidazo[1,5-a]pyridine-rhodamine FRET system as an efficient ratiometric fluorescent probe for Hg2+ in living cells. Dyes Pigm. **2017**, *146*, 136-142.

143. Rosa V.; Gaspari A.P.S.; Folgosa F.; Cordas C.M.; Tavares P.; Santos-Silva T.; et al. Imine ligands based on ferrocene: synthesis, structural and Mössbauer characterization and evaluation as chromogenic and electrochemical sensors for Hg^{2+}. *New J. Chemistry*. **2018**, *42* (5), 3334-3343.

144. Dong J.; Hu J.; Baigude H.; Zhang H.; A novel ferrocenyl–naphthalimide as a multichannel probe for the detection of Cu(ii) and Hg(ii) in aqueous media and living cells. Dalton Trans. **2018**, *47* (2), 314-322.

145. Maity A.; Sil A.; Nad S.; Patra S.K. A highly selective, sensitive and reusable BODIPY based 'OFF/ON' fluorescence chemosensor for the detection of Hg^{2+} Ions. Sens. Actuators B: Chemical. **2018**, *255*, 299-308.

146. Thapa P.; Byrnes N.K.; Denisenko A.A.; Mao J.X.; McDonald A.D.; Newhouse C.A.; Vuong T.T.; Woodruff K.; Nam K.; Nygren D.R.; Benjamin J.P.J.; Foss F.W.Jr. Demonstration of Selective Single-Barium Ion Detection with Dry Diazacrown Ether Naphthalimide Turn-on Chemosensors. *ACS Sens.* **2021**, *6*, 192-202.

147. Byrnes N.K.; Denisenko A. A.; Foss F.W.Jr.; Jones B.J.P.; McDonald A.D.; Nygren D.R.; Thapa P.; Woodruff K. for the NEXT Collaboration. Barium Tagging with Selective, Dry-Functional, Single Molecule Sensitive On-Off Fluorophores for the NEXT Experiment, 2019. arXiv:1909.04677v1.

148. Schreiber, F. Structure and growth of self-assembling monolayers. *Prog. Surf. Sci.*; **2000**, *65* (5-8), 151–257.

149. Patra D.; Barakat C. Synchronous fluorescence spectroscopic study of solvatochromic curcumin dye. *Spectrochim. Acta A Mol. Biomol.* **2011**, *79*, 1034–1041.

150. DeQuan L.; Swanson B.I.; Robinson J.M.; Hoffbauer M.A. Porphyrin Based Self-Assembled Monolayer Thin Films: Synthesis and Characterization *J. Am. Chem. Soc*. **1993**, *115*, 6975-6980.

151. Reichardt C.; Eschner M.; Schafer G. Syntheses and UV–visible spectroscopic properties of new 'fluorophilic' fluorine- and perfluoroalkyl-substituted solvatochromic pyridinium *N*-phenolate betaine dyes. J. Phys. Org. Chem. **2001**, *14*, 737-751.

152. Barfield M. Nuclear spin-spin coupling via nonbonded interactions. 1. Conformational and substituent effects on vicinal carbon-13-proton and carbon-13-carbon-13 coupling constants. *J. Am. Chem, Soc.* **1980**, 102, 1-7.

153. Shlyakhtenko L.S., Gall A.A., Lyubchenko Y.L. (2012) Mica Functionalization for Imaging of DNA and Protein-DNA Complexes with Atomic Force Microscopy. In: Tatjes D., Roth J. (eds) Cell Imaging Techniques. Methods in Molecular Biology (Methods and Protocols), vol 931. Humana Press, Totowa, NJ.

154. Zhang Y.; Yang P.; Yao F.; Liu J.; Yu L.; Synthesis and characterization of alkylated caseinate, and its structure-curcumin loading property relationship in water. *Food Chem.* **2018,** *244,* 246-253.

Biographical information

Alena Aleksandrovna Denisenko was born in Langepas, a small town in Siberia, in the former Soviet Union, now referred to as the Russian Federation. In 2010, she graduated from Surgut's Music College as an orchestra performer, ensemble member, violin performance instructor, and concertmaster for the orchestra. After graduating from college, she moved to the United States of America in order to pursue her American dream. Her academic career began in the year 2017 when she graduated with a Bachelor of Arts in Chemistry with a minor in Russian from The University of Texas at Arlington. Thereafter, she completed her education at The University of Texas at Arlington with a Ph.D. in Organic Chemistry under the supervision of Dr. Frank W Foss. Her research focuses on the synthesis and spectroscopic investigations of Ion-Selective Single-Molecule Fluorescent Imaging Molecules and Materials.